Radar Sensing in General Aviation
For Purposes of Detect and Avoid

Maas, J.B.

DOI
10.4233/uuid:b7fae981-33a4-4cdb-993c-4ec06b6534ba

Publication date
2022

Document Version
Final published version

Citation (APA)
Maas, J. B. (2022). *Radar Sensing in General Aviation: For Purposes of Detect and Avoid*. [Dissertation (TU Delft), Delft University of Technology]. https://doi.org/10.4233/uuid:b7fae981-33a4-4cdb-993c-4ec06b6534ba

Radar Sensing in General Aviation

For Purposes of Detect and Avoid

Radar Sensing in General Aviation

For Purposes of Detect and Avoid

Proefschrift

ter verkrijging van de graad van doctor
aan de Technische Universiteit Delft,
op gezag van de Rector Magnificus prof. dr. ir. T.H.J.J. Van der Hagen,
voorzitter van het College voor Promoties,
in het openbaar te verdedigen op donderdag 30 juni 2022 om 15:00 uur.

door

Jerom Bastiaan MAAS

Ingenieur in de Luchtvaart en Ruimtevaart,
Technische Universiteit Delft, Nederland,
geboren te ’s-Hertogenbosch, Nederland

Dit proefschrift is goedgekeurd door de promotor.

Samenstelling promotiecommissie:

Rector Magnificus	voorzitter
Prof. dr. ir. J. M. Hoekstra	Technische Universiteit Delft, *promotor*
Onafhankelijke leden:	
Prof. dr. ir. M. Mulder	Technische Universiteit Delft
Prof. dr. D. Kügler	Deutsches Zentrum für Luft- und Raumfahrt, Duitsland
Prof. dr. D. Delahaye	École Nationale de l'Aviation Civile, Frankrijk
Dr. A. Meta	Metasensing Technologies, Italië
Dr. F. Uysal	TNO Nederland
Prof. dr. D. G. Simons	Technische Universiteit Delft, *reservelid*
Overig lid:	
ir. R. van Gent	Selfly BV

Ir. R. van Gent heeft in belangrijke mate aan de totstandkoming van het proefschrift bijgedragen.

Trefwoorden: Airborne Radar, General Aviation, Detect and Avoid, Surveillance, Conflict Detection

Gedrukt door: Druk. Tan Heck

Omslag: J.B. Maas

ISBN 978-94-6384-342-3

Een elektronische versie van dit proefschrift is beschikbaar op
http://repository.tudelft.nl/.

You get to a certain age
where you prepare yourself for happiness.

Sometimes you never remember
to actually get happy.

John Mayer

Contents

Summary

Safety is crucial in aviation. This includes the category of General Aviation, which consists of flights that are not performed by commercial airliners. Many of these vehicles are small in comparison to the aircraft used for commercial transport, providing seats for two or four persons. Despite their limited size, accidents involving General Aviation aircraft can be costly or even lethal. Therefore, a high priority is placed on the prevention of accidents in General Aviation.

The importance of Situation Awareness

In order to prevent collisions, a pilot needs to have an accurate and complete situation awareness, so that he or she can take appropriate action to avoid hazardous situations. This awareness includes knowledge about the own aircraft, as provided by the flight instruments in the cockpit. Besides this information, the pilot needs to have information about the immediate environment.

This immediate environment can contain many different objects of which the position relative to the aircraft needs to be known. Stationary obstacles such as towers, windmills and other buildings are relevant when flying at low altitudes. Also the curvature and elevation of the landscape are relevant for a pilot flying near the ground, such as when taking off or landing at an airfield. Dynamic obstacles can also pose threats to a pilot. These obstacles can be other aircraft, and birds are also known to cause dangerous situations for aircraft. And the development of unmanned air vehicles also leads to more conflicts between drones and aircraft.

Situation Awareness Limitations in Visual Flights

For flights taking place in Instrument Flight Rules, a situation awareness solution is guaranteed and enforced; all aircraft must be equipped with the correct transponders and aircraft that do not comply are tracked down by military radar. But for flights under Visual Flight Rules, there are no such regulations, for various reasons. In these flights, which make up the majority of General Aviation flights, the pilot relies on eyesight in order to guarantee separation with other aircraft and the ground.

At times, human eyesight is insufficient to guarantee safety. This can be a consequence of a high workload for the pilot, changing weather conditions, the direction of where an object is coming from, and other reasons. This can lead to unsafe situations for the pilot and for others, both in the air and on the ground.

Technical solutions have been developed that can assist the pilot in his or her situation awareness tasks. Unfortunately, these solutions all involve the use of transponders of some kinds, which makes them dependent solutions. These solu-

tions can only provide an indication of safety, but no guarantee, because aircraft without transponders cannot be detected. An independent sensing solution in General Aviation for purposes of detect and avoid can contribute significantly to safety in the air. The aim of the research in this dissertation is to contribute to the actualization of such a solution.

Research Objective

Whilst the field of General Aviation is still in need of this independent sensing solution, such technology is already implemented in the field of automotive road traffic. Modern cars are equipped with microwave sensors that can sense the presence of obstacles such as other cars and pedestrians. The technology can be based on radar or light waves, or even visual input such as cameras. The existence of sense-and-avoid technology for road traffic is an indication that it may be possible in aviation as well.

The research objective of this dissertation is to determine to what extent it is possible to perform microwave sensing for sense and avoid purposes in General Aviation, using state of the art hardware. The focus will be on sensing technology that can be performed on board of a General Aviation aircraft, so it must be mobile and portable. Besides the possibilities of radar sensing, its natural limitations are also of interest to the researchers.

The focus in this dissertation is on radio waves as microwaves, since it is known that they can cover large distances, which is necessary in aviation. In parallel to the research presented in this thesis, a prototype of the sense-and-avoid radar system is being developed, which is used in several chapters for experimental purposes.

Results

The research started off with the development of a microwave radar simulator that can generate radar images as being processed by the prototype. It has been found that good quality fast time simulations of radar reflections are possible. It is found that it is possible to develop radar processing models based on the simulator. This has as an advantage that offline studies can be performed before costly flight tests are required. Difficulties remain in the simulation of unwanted radar reflections such as self-interference, so validation flight studies remain necessary.

It is demonstrated that it is possible to construct the radar as a mobile ground station, similar to a primary radar from Air Traffic Control. The radar can be powered by batteries and is light weight and small enough to be carried in mobile applications. It has been found that this hardware is capable of detecting a small aircraft to up to 3 kilometers distance. A method is presented that can determine the position of the target in three dimensions in real time. Experiments have demonstrated that the method has an accuracy of 2 degrees horizontally and 3 degrees vertically.

Since the radar constructs images with range-Doppler information, it is researched whether targets in the images can be tracked using traditional visual tracking methods. It is found that these methods can be used as a basis since targets appear as moving pixels in the image. A new tracking method has been

developed which is optimized for use in radar images, and it was demonstrated that the proposed method gives better results than traditional methods, for this application.

The radar is tested in flights on board of an aircraft as well. The simulator has indicated that ground reflections will be strongly visible, and this is confirmed by these flight experiments. A method is developed that can use the Doppler information of the radar reflections to determine altitude and velocity information with respect to the landscape. Simulation experiments above different landscapes have demonstrated that the method works best above flat landscapes. This method of radar state estimation is a more direct way of altimetry than using GPS, which is dependent on local calibration by the pilot.

A second flight experiment is performed with the radar aperture aimed towards the side of the aircraft. In this mode of operation, surface elements such as roads and rivers can be recognized in the ground reflections from the radar. It has been proved that these reflections can be compared to a digital map of the local environment, with which the aircraft latitude and longitude coordinates by GPS can be verified, as well as its heading.

An alternative method of radar sensing was developed in this research project as well. This method is using a bistatic radar constellation, in which the primary radar from Air Traffic Control was used as transmitter, and a pilot carried a Software Defined Radio that can be used as the receiver. It was demonstrated that this method of radar sensing is capable of detecting static objects such as towers and buildings in real time. Further research is necessary before dynamic obstacles such as aircraft can be detected.

Conclusion

Overall, it is found that microwave sensing technology can provide a significant benefit in the situation awareness of pilots in General Aviation. The independent nature of radio waves' reflections ensures that these systems can provide reliable results under various circumstances.

On-board radar sensing can be performed in various methods, which can provide different information to a pilot. This information can contain position and distance information to other aircraft, and also the own position of the aircraft with respect to the landscape can be verified in three dimensions.

Before this technology can be implemented in a final product in flight, special attention needs to be paid to the presence of unwanted signals, such as self interference. Image processing techniques that enhance radar reflections and remove the presence of noise can greatly improve the performance of these radar sensing applications.

Samenvatting

Veiligheid is essentieel in de luchtvaart. Dit is ook van toepassing op de categorie 'General Avation', die bestaat uit vluchten die niet door commerciële luchtvaartmaatschappijen worden uitgevoerd. Veel van deze vliegtuigen zijn klein in vergelijking met degene die gebruikt worden voor commerciëel transport, en bieden plaats aan twee of vier personen. Ondanks hun beperkte grootte kunnen ongevallen in General Aviation kostbaar zijn of zelfs dodelijk. Daarom heeft het voorkomen van ongevallen prioriteit binnen General Aviation.

De Noodzaak van Situatiebewustzijn

Teneinde aanvaringen te voorkomen dient een piloot een accuraat en volledig situatiebewustzijn te hebben, zodat hij of zij gepaste actie kan ondernemen om gevaarlijke situaties te voorkomen. Dit bewustzijn omvat kennis over het eigen vliegtuig, zoals in voorzien door vluchtinstrumenten in de cockpit. Behoudens deze kennis dient de piloot ook informatie te hebben over de lokale omstandigheden.

De nabijheid van het vliegtuig kan een verscheidenheid aan objecten bevatten waarvan de positie ten opzichte van het vliegtuig bekend dient te zijn. Stilstaande obstakels, zoals torens, windmolens en flatgebouwen, zijn relevant bij vluchten op lage hoogtes. Ook de kromming en hoogte van het landschap zijn relevant voor een piloot in de buurt van de grond, zoals bij het opstijgen of landen in de nabijheid van een vliegveld. Dynamische obstakels kunnen ook bedreigingen vormen voor een piloot. Deze obstakels kunnen andere vliegtuigen zijn en het is bekend dat ook vogels gevaarlijke situaties kunnen veroorzaken voor vliegtuigen. De ontwikkeling van onbemande vliegtuigen leidt ook tot meer conflicten tussen drones en vliegtuigen.

Grenzen aan Situatiebewustzijn bij Visuele Vluchten

Voor vluchten die plaatsvinden in Instrument Vliegregels wordt een oplossing voor situatiebewustzijn gegarandeerd en afgedwongen; alle vliegtuigen dienen uitgerust te zijn met de correcte transpondertechnologie, en vluchten die niet conformeren aan deze regels worden opgespoord door militaire radar. Maar voor vluchten die onder Visuele Vliegregels plaatsvinden gelden deze regels niet, voor verschillende redenen. In dit soort vluchten, die de meerderheid van General Aviation vormen, vertrouwt de piloot op zijn zicht om separatie met andere vliegtuigen en de grond te garanderen.

Zo nu en dan is zicht niet voldoende om veiligheid te kunnen garanderen. Dit kan een gevolg zijn van hoge werklast voor de piloot, veranderende weersomstandigheden, de richting van waaruit een ander object komt, en andere redenen. Dit

kan leiden tot onveilige situaties voor de piloot en voor anderen, zowel in de lucht als op de grond.

Er zijn technische oplossingen ontwikkeld om piloten te assisteren in hun situatiebewustzijn. Helaas gebruiken deze oplossingen transponders, waar de oplossing afhankelijk van is. Deze oplossingen kunnen slechts een indicatie geven van veiligheid, maar geen garantie, omdat vliegtuigen zonder transponders niet gedetecteerd kunnen worden. Een onafhankelijke oplossing voor de detectie van vliegtuigen in General Aviation kan een significante bijdrage leveren aan vliegveiligheid. Het doel van het onderzoek in dit proefschrift is om een bijdrage te leveren aan de totstandkoming van een dergelijke oplossing.

Onderzoeksdoel

Terwijl de kleine luchtvaart in afwachting is van een dergelijke onafhankelijke detectie oplossing, bestaat zulke technologie al op het terrein van de zelfrijdende auto. Moderne auto's zijn uitgerust met microgolf sensors die de aanwezigheid van obstakels zoals andere auto's en voetgangers kunnen detecteren. De technologie kan gebaseerd zijn op radio- of lichtgolven, of zelfs op visuele signalen zoals van camera's. Het bestaan van detectietechnologie voor wegverkeer is een indicatie dat dit ook mogelijk kan zijn in de luchtvaart.

Het onderzoeksdoel van dit proefschrift is om te bepalen in hoeverre het mogelijk is om microgolftechnologie toe te passen voor doeleinden van detectie en ontwijkmaatregelen in General Aviation, met de nieuwste van de nieuwste technieken. De nadruk zal liggen op detectietechnologie die aan boord van een sportvliegtuig toegepast kan worden, dus deze moet mobiel en draagbaar zijn. Naast de mogelijkheden van radardetectie worden ook de inherente limitaties onderzocht.

Resultaten

Het onderzoek is begonnen met het ontwikkelen van een microgolf radar simulator die radarafbeeldingen van hoge kwaliteit kan genereren zoals ze door een radar prototype worden gevormd. Het is bevonden dat het mogelijk is om dergelijke simulaties in hoog tempo uit te voeren, en dat methodes van signaalverwerking ontwikkeld kunnen worden aan de hand van deze simulator. Dit heeft als voordeel dat computerstudies gedaan kunnen worden voordat kostbare testvluchten noodzakelijk zijn. Moeilijkheden blijven in het simuleren van ongewenste radarreflecties zoals eigeninterferentie, dus vliegexperimenten voor validatie blijven noodzakelijk.

Het is aangetoond dat het mogelijk is om de radar als mobiel grondstation te construeren, vergelijkbaar met een primaire radar van de luchtverkeersleiding. De radar kan op accu's aangedreven worden en is licht en klein genoeg om verplaatst te worden in mobiele toepassingen. Het is bevonden dat deze hardware geschikt is om een klein vliegtuig op een afstand van 3 kilometer te herkennen. Er is een methode gepresenteerd om de positie van het doelwit in drie dimensies vast te stellen tijdens de operatie. Experimenten hebben aangetoond dat deze methode een accuratesse heeft van 2 graden horizontaal en 3 graden verticaal.

Aangezien de radar afbeeldingen genereert met afstands-Doppler informatie,

is het onderzocht of doelwitten in de afbeeldingen gevolgd kunnen worden met traditionele visuele methoden. Het is bevonden dat deze methoden inderdaad als basis gebruikt kunnen worden, omdat doelwitten als bewegende pixels verschijnen in de radar afbeeldingen. Een nieuwe methode is ontwikkeld om doelwitten in radarafbeeldingen te volgen, en het is aangetoond dat de voorgestelde methode betere resultaten oplevert dan traditionele methodes, voor deze toepassing.

De radar is tevens getest in vluchten aan boord van een vliegtuig. De simulator heeft reeds aangekondigd dat reflecties van de grond duidelijk zichtbaar zullen zijn, en dit wordt bevestigd door de testvluchten. Een methode is ontwikkeld die Doppler informatie van de radar kan gebruiken om hoogte- en snelheidsinformatie van het eigen vliegtuig af te leiden, relatief aan het landschap. Simulatie experimenten hebben aangetoond dat de methode het beste werkt boven vlakke landschappen. Deze methode van positiebepaling is een directere manier dan hoogtebepaling met GPS, wat afhankelijk is van lokale kalibratie door de piloot.

Een tweede testvlucht is uitgevoerd, waarin de radaropening zijwaarts gericht is. Met deze modus operandi kunnen oppervlaktelementen zoals wegen en rivieren herkend worden herkend worden in de grondreflecties van de radar. Het is bewezen dat deze reflecties vergeleken kunnen worden met digitale kaarten van de nabije omgeving, waarmee de lengte- en breedtecoordinaten van GPS geverifiëerd kunnen worden, alsook de vliegrichting.

Een alternatieve methode van radardetectie is tevens ontwikkeld in dit onderzoeksproject. Deze methode gebruikt een bistatische radar opstelling, waarin de primaire radar van de luchtverkeersleiding wordt gebruikt als zender en waarin een piloot een Software Defined Radio meeneemt als ontvanger. Het is aangetoond dat deze methode van radardetectie geschikt is om statische obstakels zoals torens en windmolens te kunnen herkennen. Verder onderzoek is nodig voordat dynamische obstakels zoals vliegtuigen herkend kunnen worden.

Conclusie

Globaal gezien is het bevonden dat microgolf detectietechnologie een significant voordeel kan zijn voor het situatiebewustzijn van piloten in General Aviation. De inherente onafhankelijke eigenschappen van de reflecties van radiogolven staan ervoor garant dat dit soort systemen betrouwbare resultaten kunnen bieden onder uiteenlopende omstandigheden.

Radar detectie aan boord van een vliegtuig kan op verschillende manieren worden uitgevoerd, waarmee verschillende informatie voor een piloot kan worden gegenereerd. Deze informatie kan positie- en afstandsinformatie naar andere vliegtuigen bevatten. Tevens kan de eigen positie in verhouding tot het landschap vastgesteld worden in drie dimensies.

Alvorens deze technologie toegepast kan worden in definitieve producten in de luchtvaart, dient er speciale aandacht besteed te worden aan de aanwezigheid van ongewenste signalen, zoals door zelf-interferentie. Afbeeldingsbewerkingstechnieken die gewenste radarreflecties versterken en de aanwezigheid van ruis verminderen kunnen de prestaties van radardetectie toepassingen sterk verbeteren.

Preface

This thesis contains the result of a period of intensive research, which lasted from 2015 until and including 2021. The thesis is written in 2021 and 2022 for the purpose of obtaining the degree of doctor at Delft University of Technology.

The research performed was done in collaboration with the company Selfly BV, located in the Netherlands, which funded the project. A grant from the European Commission was used for this purpose. The company was not involved in the processes of study design, data collection and analysis, decision to publish, or preparation of the manuscript. The research questions answered in the research are formulated to help the development of modern radar sensing equipment for the General Aviation market.

The research in this thesis is about radar sensing for general aviation purposes. The aim is to bring independent sensing technology to the general aviation market. The technology should be portable and affordable and the results must be reliable. This dissertation contains chapters that focus on the detection, localization and tracking of targets from the pilots point of view, as well as on navigation of the aircraft. Two different methods of radar sensing are considered.

I am proud of the results achieved in the past years. When I first arrived at Delft University of Technology in 2008, the motto of the university was 'Challenge the Future'. I think that this thesis is an example of that: empowering new applications through the development of modern technology. I am thankful for everyone who supported this thesis: before, during and after the research.

This dissertation illustrates the possibilities of new technologies that may become available in General Aviation in the future. I hope that you, the reader, find it inspiring and that you enjoy your time reading.

Jerom Bastiaan MAAS
Delft, April 2021

1

Introduction

Safety is crucial in aviation. This is because of the prices of accidents. The expenditures of purchase and repairs of aircraft are often higher than those for other types of vehicles, and physical parameters such as flight speed are large. Consequences of accidents are always costly, and sometimes even lethal. The prevention of accidents in aviation is of high priority.

Instrument and Visual Flight Rules

In order to reduce the risk of accidents, civil aviation authorities have implemented safety margins, measures and procedures. Single points of failure are avoided, and redundant safety features are often implemented. One example of this is the system of airspace classes, that separates different types of aviation from one another by sorting on the type of aircraft and the flight rules used. In general, two sets of air traffic rules are used in aviation: IFR and VFR - abbreviations of Instrument Flight Rules and Visual Flight Rules. These rules are applied in different circumstances.

The most commonly used ruleset is IFR. When flying under IFR, the pilot bases his actions on the readings of the instruments in his flight deck[1]. The pilot follows the instructions given by his flight plan, his instruments and those from Air Traffic Control. These instructions include flight levels and compass headings. The responsibility for collision avoidance (other than those on short term) is carried out by remote operators in Air Traffic Management. This also includes flight planning. All commercial air traffic, both for business and holiday travel, is carried out under IFR.

But IFR is not suitable for all flights. Glider aircraft, for example, often stay inside thermal bubbles where they gain altitude. If multiple aircraft are present, the distance between them can become smaller than the error margins of the surveillance equipment of Air Traffic Control. Also, the radio beacons to empower IFR flight are not present on all airfields, specifically the smaller ones. And many recreational pilots prefer to control their own flights instead of asking permission for their

1

Figure 1.1: Instrument Meteorological Conditions in which eyesight is hindered and VFR cannot be applied safely

manoeuvers, which is necessary in IFR.

The alternative to IFR is VFR, the Visual Flight Rules[2]. As the name implies, these rules are based on the principle of visual confirmation of the world outside of the cockpit window, this compared to the IFR principle of using the cockpit instruments. This can mean that a pilot chooses a flight altitude to be a certain distance below the clouds, and not an altitude as indicated on his altimeter. In VFR, the pilot is responsible for immediate collision avoidance and needs to search the surroundings for possible hazards. In uncontrolled airspace pilots can fly according to their own insight, as long as safety standards are not violated. This gives glider pilots the option to circle in thermal bubbles as long as they are convinced of the safety, and pilots from motorized aircraft have more freedom to fly their own planned flights.

Visual Limitations

Many flights are performed in VFR, especially in the category of General Aviation, but that does not mean that it is perfect. Relying on eyesight instead of instruments removes a dependency on flight instruments, but it introduces a dependency on visual limitations. VFR flights are not allowed when the weather is poor, such as at night and in conditions of fog, an example of poor visual conditions is given in Figure 1.1. Weather predictions are quite accurate, but it is possible that a flight under good visual conditions suddenly takes a turn for the worst when the weather changes abruptly. Also, glare from the sun can hinder a pilot in his visual tasks.

Another limitation can come from the aircraft itself. Since the fuselage of an aircraft is opaque, there is always a region where the pilots cannot look since they cannot see through it. The own wings also obstruct the vision of the pilot, and they can be located at the top and/or bottom of the fuselage. Numerous accidents have happened where aircraft got into contact but could not even see each other coming, since they were flying above one another, unlike the situation in Figure 1.2.

Apart from these limitations, it is possible that a human pilot simply overlooks a hazardous aircraft or other obstacle, even though his eyesight is sufficient ac-

Figure 1.2: Example: An accident happened where a low-wing aircraft landed on top of a high-wing aircraft, because the wings prevented visual separation. Luckily there were no injuries in this case.

cording to the mandatory aeromedical examinations. Studies have demonstrated the difficult nature of identifying moving aircraft over large distances while flying, and these tasks become more difficult in situations of stress or under a high workload, such as in crowded airspaces. Even if a target is identified visually, it can still be difficult to estimate the distance to the aircraft and the corresponding risk level[3, 4].

Summarizing, there are multiple ways in which the limitations of visual hazard detection can lead to unsafe situations in General Aviations. This can mean that an aircraft flies at a location where it is not supposed to be, risking an infringement of airspace and/or a collision with other aircraft or obstacles.

Solutions to visual limitations

As described in the previous paragraphs, VFR flight is still the standard choice for many flights in General Aviation, but visual detection of objects does have its limitations, of which several consequences are named. It is therefore not surprising that many solutions are sought to overcome these limitations, or at least to reduce their risks.

A partial solution can be found in procedures such as standardizing flight routes around the airfield, of which an example can be seen in Figure 1.3. If all aircraft follow a given route set, interaction should be limited to a minimum. Also, rules such as keeping on the right hand side of landmarks such as rivers or railways ensure that oncoming traffic is avoided.

Technical solutions have also been sought. Transponder technology is a good example of a method to assist the pilot in detecting other aircraft in the vicinity. If the technology is present on board of two different aircraft, microwave commu-

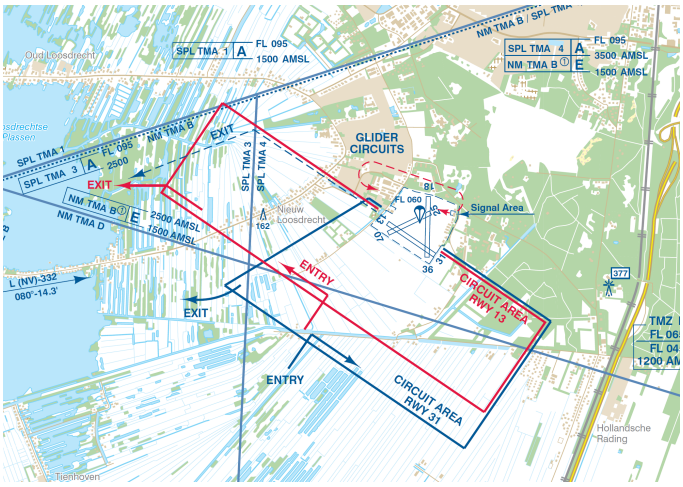

Figure 1.3: An example of VFR flight routes around a runway of an airfield

nication between two transponders can be used to exchange position information. If the devices compute that safety margins between the aircraft are about to be violated, they can provide warnings for the pilot. It is possible to pair this warning with a conflict resolution advice.

Two of these solutions are well-known in aviation: Automatic Dependent Surveillance-Broadcast (ADS-B) and FLARM. ADS-B is developed as technology for Air Traffic Control, and it has aircraft broadcasting their locations over long distances [5]. The technology works well and is mandatory in IFR-graded airspace, but it is also expensive and therefore not widely used in sports aircraft in General Aviation.

The other technology is FLARM [6], which works on a similar principle but has a lower price. This comes with the downside that the range is smaller than for ADS-B, and that accuracy and reliability are reduced. FLARM systems are widely used by glider aircraft because the extra safety is well appreciated when flying in close vicinity in thermal bubbles. But apart from glider aircraft, most General Aviation aircraft are not equipped with the system.

So transponder technology can be helpful to overcome several of the limits of VFR flight, but it is not widely used. This is a problem, since transponder technology only works if both aircraft in a conflict carry the same equipment, such that they can communicate together. Transponder technology can only provide warnings in dangerous situations, but it cannot guarantee safety.

Attempts have been made to reach standardization, but they have not been successful due to the different demands of the diverse aviation market. As long as not all aircraft are equipped with similar transponder technology, there will be a risk of aircraft in the airspace which are undetectable by the transponders, which can lead to dangerous situations.

Microwave Sensing as a Solution

Microwave sensing technology can be another solution to increase situation awareness for a pilot. The oldest microwave sensors have been developed in the 1940's, broadcasting radio waves from a transmitter. These radio waves would reflect on airborne objects, bouncing back to the ground station where they are collected.

Using radar (RAdio Detecting And Ranging) for detection of objects is a well-known technical solution. One of its properties is that it works on all objects because it is independent on the cooperation of the receiver, as opposed to transponder technology. Radar is known to observe aircraft, but also flocks of birds, high buildings and landscapes. Radar technology has been applied for various surveillance purposes [7]:

En Route Radar

En Route Radars are used to observe the higher regions of airspace, in which aircraft fly at cruise altitude. En Route Radars can cover distances up to 240 nautical miles. They consist of a primary radar, which uses reflections of microwave signals to determine a targets location in the horizontal plane. En route radars are coupled with secondary radar systems on top of the primary radar, which determine altitude information (and more) by interrogation with on board transponders.

Airport Surveillance Radar

Airport Surveillance Radar systems are similar in operation to En Route Radars, with the difference that they are designed for closer ranges and lower altitudes: up to 60 nautical miles far and 25000 feet high. Airport Surveillance Radars are deployed in the terminal area around airports.

Precision Approach Radar

A Precision Approach Radar can provide both horizontal and vertical position information of targets independently, so transponder technology on board of the aircraft is not needed. Precision Approach Radars operate up to 20 nautical miles distance, and are used to guide aircraft on their final approach to the runway. An example of a Precision Approach Radar can be seen in Figure 1.4.

Surface Movement Radar

Surface Movement Radar is used to detect objects on the ground of an airfield. These radars have a low maximum range, but high accuracy and update rate. It is used by Air Traffic Controllers in Tower Control to verify their observations of movements on the airport ground.

Special Radar Applications

Radar technology is otherwise applied in aviation for the detection of bad weather in Weather radar. Such a radar can be mounted on board of flying aircraft. Other modern applications also include radars that detect flocks of birds or flying drones.

Figure 1.4: Precision Approach Radar hardware, pictured in 1985

No Mobile Applications

As can be concluded from the above examples, radar sensing technology is widely implemented in aviation. However, the hardware is stationary and ground based for all of the above examples. Radar transmitters typically consist of large pivoting antenna cones, which cannot be fitted on board of any sports aircraft. Also, they tend to use more power than what the on board battery can provide and the price is too steep for personal use. The hardware from Figure 1.4 for example, is unsuitable to take on board of any General Aviation aircraft.

But Figure 1.4 is taken in 1985 and much process has been made in the field of microwave sensing since then. This has partly been empowered by the arrival of self-driving cars, which need proper sensing equipment in order to make balanced decisions. The quality of the hardware has been improved to such a great extent that multiple antennas can be installed on a single vehicle for an acceptable price, and new software methods have been developed such that the results of these antennas can be processed while driving. These systems operate independently; they do not rely on the presence of transponders on board of other cars.

This can be very beneficial in aviation, since the only available conflict detection systems available for VFR pilots are 'dependent' systems, as explained in the previous section. An 'independent' and mobile collision sensing solution for general aviation does not exist. Other applications can also be possible, such as detailed tracking of flights for safety trainings or for diagnostic purposes. It may also be possible to relay information of aircraft without transponders to those that do carry transponder technology on board, or it can empower Beyond Visual Line of Sight operations for unmanned aviation.

However, crucial differences exist between road traffic and aviation: the distances and velocities that occur in flight are much larger than those on the road, and movement in aviation take place in three dimensions as opposed to road traffic which is bound to the ground. This means that radar sensors in aviation must be

able to cover larger areas than those used in road traffic and that other design parameters, such as precision, update rate and antenna aperture, may differ for each application.

So, the applications of radar sensing in General Aviation are promising. The question is which of these applications can be actualized with modern hardware.

This Thesis

In this thesis, I will present the results of extended research to the possibilities of using modern radar technology for Sense and Avoid purposes in General Aviation. The focus will be mainly on applying the technology in flight. Therefore, the focus will be on hardware that is affordable, compact and light-weight, and have a low power consumption. In collaboration with a hardware company, a prototype of an active radar system for General Aviation is being developed. This prototype will be the focus of three chapters in this thesis.

In chapter 2, a simulation model is introduced which is developed for the purpose of this thesis. The model is used to simulate the radar output of the hardware system in flight. This ensures that offline studies to the behavior of the radar results are possible, which saves countless flight tests. This model can also help to explain experimental results and to verify the functions of the hardware.

The prototype is tested in a stationary mode in chapter 3, in which the radar is placed on the ground and aimed to the sky. A test aircraft made a flight within the scope of the radar, and the radar is used to observe the aircraft. Direction of Arrival Estimation techniques are used to determine the location and velocity of the aircraft in three dimensions, and the results are compared to those of a GPS tracker that the test aircraft carried on board. This is used to validate the performance of the radar.

In chapter 4, a method is presented to track radar observations through time. The method is optimized for use in radar images from the prototype, which are different from traditional visual images. The method is tested in radar simulations of a flight with nearby targets, all are based on real flight recordings. The results of the new tracking algorithm are compared to those of traditional tracking methods.

The prototype is tested on board of an aircraft in chapter 5. In this chapter, the focus is not on detecting aircraft while in motion, but to focus on the reflections caused by the landscape. It is expected that these reflections can be used to compute the altitude and velocity of the aircraft with respect to the ground surface. Since traditional altimetry does not measure the altitude with respect to the landscape but with respect to calibrated values, this is potentially a great benefit.

The prototype is also tested on board of an aircraft in chapter 6. Contrary to the situation in chapter 5, the radar is not mounted facing forward, but to the side. It is demonstrated that the radar returns can be mapped onto a flat plane, on which patterns of radar returns become visible which show resemblance to features on the ground. In this chapter, it is researched whether these patterns can be used to verify the location of the aircraft as given by GPS, assuming that a map of the local environment is available.

In chapter 7, an alternative approach is used to construct a bistatic radar setup,

using the primary radar from Air Traffic Control as the transmitter. The main advantage of this is that it is not necessary to transmit our own signal, so the hardware used for this application can have a lower size, power consumption and price. The goal of this chapter is to investigate whether this type of hardware can also yield promising results.

These five chapters come together in chapter 8, in which the main conclusions of this thesis are drawn.

References

[1] F. A. Administration, *Instrument Flying Handbook* (United States Government Printing Office, 2012) p. VOLUME 2.

[2] C. A. S. A. Australia, *Visual Flight Rules Guide* (Australian Government, 2021).

[3] E. Galanter and P. Galanter, *Range estimates of distant visual stimuli,* Perception & Psychophysics **14**, 301 (1973).

[4] J. Morio, T. Lang, and C. Le Tallec, *Estimating separation distance loss probability between aircraft in uncontrolled airspace in simulation,* Safety Science **50**, 995 (2012).

[5] International Civil Aviation Organisation, *ADS-B Implementation and Operations Guidance Document,* (2018).

[6] F. T. GmbH, *PowerFLARM Portable Manual,* (2020).

[7] J. M. Hoekstra and J. Ellerbroek, *AE4321 Air Traffic Management Lectures,* (2022).

2

Modelling an Airborne Detect & Avoid Radar for General Aviation

J Maas, R Van Gent, J Hoekstra

The development of radar technology is an iterative process that requires testing often. Since the application in this dissertation is General Aviation, tests should ideally also take place in an aeronautical environment. But experiments in aviation are costly, both in financial and logistical aspects. Therefore a simulation platform is developed with which the radar output can be simulated.

In this chapter, the simulation platform is introduced and described, and its performance is verified with experimental data. This simulator is used to develop the algorithms presented in chapters 3, 5 and 6.

Part of this chapter is submitted as *Modelling an Airborne Detect & Avoid Radar for General Aviation*, Journal of Aerospace Information Systems, 2021

Nomenclature

A	=	Object Reflectivity
B	=	Bandwidth
c	=	Speed of Light
CPU	=	Central Processing Unit
F_c	=	Carrier Frequency
F_s	=	Sample Frequency
G	=	Antenna Gain
k_r	=	Reflectivity Factor
l	=	Wavelength
L	=	Atmospheric Loss Factor
P_e	=	Emitter Power
P_r	=	Received Power
PRF	=	Pulse Repetition Frequency
R	=	Range
V_R	=	Radial Velocity
λ	=	Wavelength
σ	=	Radar cross section

2.1. Introduction

Having an accurate and reliable awareness of the surroundings is essential for safe flight. Hazards around the aircraft must be detected and evaluated in order to prevent dangerous situations. Pilots flying under Visual Flight Rules (VFR) use eyesight as a primary means of detecting objects, but dangers may be overlooked or not recognized. Transponder based technology such as FLARM or ADS-B can assist a pilot in detecting obstacles, but aircraft remain invisible if they do not carry the proper equipment.

Technological advancements in the field of microwave sensing have brought smaller and lighter sensor hardware to the market [1–3], to the extent that this hardware can be brought on board of an aircraft [4]. A Frequency Modulated Continuous Wave (FMCW) radar can function as a mobile detect and avoid radar, which can identify objects independent of the equipment that they carry. This hardware has the potential to lift safety in General Aviation (GA) to a new level, if it can indeed detect hazards independently in all situations.

A feasibility study is performed in order to investigate the advantages and disadvantages of such a method of detect and avoid in aviation. This study consists of field tests with the prototype radar and simulation experiments are carried out as well [5–7]. In order to properly simulate the operation of the radar, a model of the radar output is developed. This model must accurately represent radar output when used in various simulation setups.

In this chapter we present the FMCW simulation model that is presented for this feasibility study. The code is presented in section 2.2, including best practices discovered in the programming. In section 2.3, the resulting output of the simulator is presented, and this output is compared to that of the actual system in section

2.4. The differences between simulator and actual results are discussed in section 2.5. The conclusions of this work can be found in section 2.6.

2.2. Setup of the Simulation

In this section the construction of the radar simulator is presented. The goal and general structure of the simulator are presented in section 2.2.1, after which the hardware is discussed in section 2.2.2. The modeling of the reflection surfaces is presented in section 2.2.3. The simulation of the radar antennas and the construction of radar images as output are presented in sections 2.2.4 and 2.2.5.

2.2.1. Simulator Goal and Structure

The goal of the simulator is to simulate the operation and output of the microwave system accurately, when the state of the radar platform is given within a known dynamic environment. The time required for a single simulation should be as low as possible.

Since an FMCW radar system is simulated, the Doppler effect will need to be part of the simulation and therefore the velocity of the radar system platform is also required. This means that the inputs of the radar simulator are:

- (static) The specifications of the radar hardware
- (static) The shape of the terrain around the radar platform
- (static) The position and attitude of the radar on the platform (aircraft)
- The position, velocity and attitude of the radar platform
- The position, velocity and reflectivity parameters of nearby objects

With these parameters, the simulator can be used for this aviation purpose as described in section 2.1. However, it is not limited to simulations of flying radar systems. The simulator will be suited for any moving microwave sensing system in an environment with moving reflecting objects, such as sensors on self-driving cars. Of course static situations can also be simulated, but the simulator will then contain unnecessary computations.

The general structure of the radar simulator can be depicted as a flow diagram. This diagram can be seen in Figure 2.1.

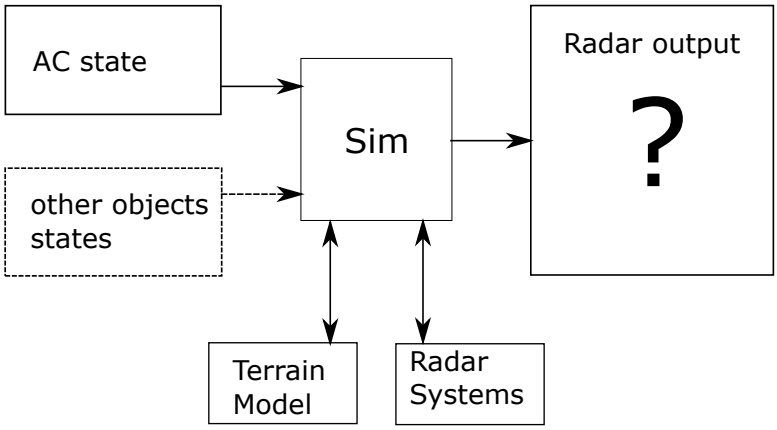

Figure 2.1: General Structure of the Radar Simulator

Using Python, the class to be used as radar simulator is constructed with the following code:

Code 2.1: Main properties of Simulator class

```
import Terrain, Hardware
class Simulator:
 def __init__(self, LatLon):
  # Hardware is an object that contains all the radar
      information
  self.HW = Hardware.Hardware()
  # Use Latitude, Longitude Coordinates to construct a
       model of the local terrain and store it
  self.TerrainModel = Terrain(LatLon)
  ...

 def Sim(self, PlatformState, **kwargs):
  # If other aircraft are included in the simulation,
      they will be named in **kwargs
  ...
  return SimOutput
```

2.2.2. FMCW Hardware

A Frequency Modulated Continuous Wave Radar system broadcasts a continuous signal, of which the frequency varies. The signal can be reflected on a target and returned to the radar system, which also listens to the reflections. When the outgoing and incoming signals are compared to one another, a shift in frequency and a time delay may be observed. A shift in time delay is caused by the travel time from the radar to the target surface and back, which is a measure for the range (R). A shift in frequency is caused by the Doppler effect, when the target velocity has a relative nonzero speed towards the radar. This can be used to compute the

radial velocity (V_R).

As will be discussed in section 2.2.2 below, the antennas used in this system have a wide field of view, in order to cover all three-dimensional directions around the aircraft quickly. This has as a consequence that many reflections will be observed simultaneously. The recorded signal will be a sum of all reflections. If the signal is sampled with a high sampling rate, Fourier analysis differentiates the incoming signals from one another. With two Fourier analyses, the incoming signals can be sorted in R and V_R directions.

Hardware Specifications and Signal Parameters

Sorting the signals in R and V_R directions results in a two-dimensional image of the antenna output, in which the value of each pixel is a complex number - a consequence of the Fourier analysis. In order to compute what the resolution of the image will be, the technical specifications of the radar system are required. In this chapter the specifications are taken of a prototype which is used in section 2.4, they can be found in code 2.2.

The emitted signal is repeated every given time interval, with a frequency of PRF. This parameter is at the basis of the range dimension of the radar image. The theoretical maximum range that the radar can achieve and the range resolution are known scientific equations [8, 9], which can be used directly in the simulator. This is also the case for the maximum absolute Doppler velocity which can be detected [8]. These relations are known as:

$$R_{max} = \frac{c \cdot F_s}{2 \cdot B \cdot PRF} \tag{2.1}$$

$$R_{resolution} = \frac{c}{2 \cdot B} \tag{2.2}$$

$$V_{max} = \frac{PRF \cdot \lambda}{4} \tag{2.3}$$

The number of pixels in V_R direction is determined by the number of samples used in the Fourier analysis. Increasing this number increases the detail of the V_R results, but it comes with the cost of an increase in computation load, and a longer measurement time to collect all the samples for an image, unless the sample rate is increased accordingly.

Similarly, the maximum range can be reduced to speed up computations. With the specifications (found in code 2.2 below), the maximum range would be about $30km$, but the transmitted signal power P_e is not high enough to cover all that distance. Signals received at these distances will be too weak to be visible above the background noise. To minimize the computational load, the maximum range is set to $5km$.

All these parameters are computed in a Hardware object, of which the reference is saved in code 2.1 such that the parameters are accessible during the simulation. The code for this is given in code 2.2 below.

Code 2.2: Computing Hardware Properties

```
import numpy as np
class Hardware:
 c  = 3.e8      #[m/s]Speed of light
 Fc = 9.425e9   #[Hz] Carrier Freq
 l  = c/Fc      #[m]  Wavelength
 Fs = 10.e6     #[Hz] Sampling Freq
 PRF= 4921.     #[Hz] Pulse Rep Freq
 Pe = 40.       #[dBm]Power Emitted
 B  = 10.e6     #[Hz] Bandwidth
 nV = 250       #[-]  Number of Vr pixels
 def __init__ (self):
  # Maximum values
  self.Rmax = self.c * self.Fs / (2 * self.B * self.
      PRF) #[m]
  self.RLim = 5000 #[m] Use this value instead of Rmax
  self.VLim = self.PRF * self.l / 4 #[m/s]
  # Find resolutions
  self.dR   = self.c / (2 * self.B) #[m]
  self.dV   = 2 * self.VLim / self.nV
  # Construct Axes and set value in middle of pixel
  self.Raxis = self.dR/2 + np.arange(0, self.RLim,
      self.dR)
  self.Vaxis = self.dV/2 + np.linspace(-self.VLim,
      self.VLim, num=self.nV, endpoint=False)
  self.nR = self.Raxis.size
```

Antenna Gain Pattern

In order to simulate the radar prototype as accurately as possible, the antenna gain pattern is included in the simulation. The gain pattern is dependent on azimuth and elevation with respect to the antenna normal. Oftentimes measurements of the gain patterns are available from the manufacturer, in this case they are as well. The challenge is that the measured patterns are two one-dimensional sets, and the full antenna pattern is required. These patterns in azimuth and elevation direction are different from one another, and not symmetrical around 0 either, they can be found in figure 2.2.

In order to build a 3D model of the antenna gain pattern, it is chosen to add the losses in azimuth and elevation direction to one another. The resulting three dimensional gain pattern is displayed in Figure 2.2. This method can be compared to taking the L1 norm to the antenna direction. Another option can be to use Pythagoras' theorem to compute the L2 distance, while assuming a point symmetrical gain pattern.

2.2.3. Reflection Surfaces

In order to simulate the performance of the system, the radar power equation, Equation 2.4, must be applied.

$$P_r = \frac{P_e G^2 A \lambda^2 L}{(4\pi)^3 R^4} \tag{2.4}$$

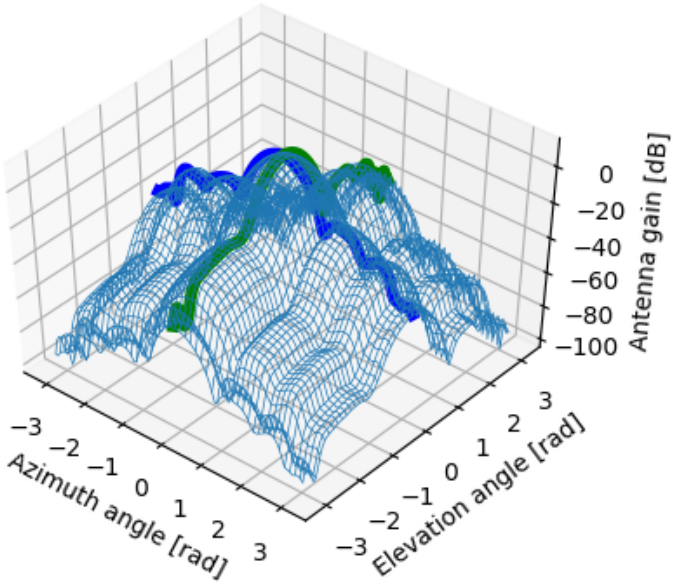

Figure 2.2: Two one-dimensional gain lines and the resulting three dimensional gain model

In Equation 2.4, the received power of the signal P_r is dependent on the emitted power P_e, the antenna gain G, distance R, the wavelength λ and the reflectivity A of the surface. The same antennas are used for transmission of the signal and for the reception, so $G = G_T = G_R$. The symbol L is the loss factor, representing factors such as fluctuation losses and atmospheric losses. These losses are assumed 0 in the simulation, therefore L is 1. The reflectivity is a product of the radar cross section σ and a reflectivity factor k_r, as seen in Equation 2.5:

$$A = \sigma * k_r \tag{2.5}$$

The reflectivity factor is dependent on the incidence angle of the radar signal with respect to the surface plane. Since P_e and λ are properties of the hardware object as seen in code 2.2, the following properties are required from the surfaces:

- Position (relative to radar)
- Velocity (relative to radar)
- Area
- Reflectivity

Objects Surfaces

In this simulator all surface objects are aircraft related. Their flights are noted in latitude and longitude. The first step is to transform their coordinates to a Cartesian system, linearized at the radar location.

The earth is assumed to be flat, which greatly increases simulation speed. The effect of this assumption at maximum range $self.Rlim = 5km$ is approximately $2m$ height, which is small compared to the radar range resolution of $self.dR = 15m$.

After transforming to Cartesian coordinates, computing the relative position and velocity is simply done by subtracting the state vector of the radar system from those of the aircraft. The areas of all aircraft, simulated to be small General Aviation aircraft, is assumed to be $1m^2$, and their reflectivity factor is 1.

Landscape Surfaces

Data from the landscapes is retrieved as elevation files for landscapes (downloaded from http://www.viewfinderpanoramas.org), in which each file consists of $1201 * 1201$ data points over the scope of one degree latitude, longitude. This means that the terrain data is also given in geographic coordinates, and the same transformation to Cartesian coordinates will be performed as with the aircraft location.

The absolute velocity of the landscape is zero in the Earth Fixed Reference Frame. The landscape is assumed to be horizontal, and therefore its area is only dependent on the number of elements and the latitude of the area, as indicated in Code 2.3 below:

Code 2.3: Computing Terrain Area

```
import numpy as np
Re = 6371000 #[m] Earth Radius
...
Elevation = np.load(filename)
# Compute area of 1 degree x 1 degree
TotalArea = (Re*np.pi/180)**2
# Area of each element, more northern parts are
    smaller
Area = TotalArea * np.cos(Latitude) / Elevation.size
```

For the reflectivity, a simple model is assumed: the reflectivity factor of the ground is the cosine of the incidence angle. This means that if the radar is right above the ground, the reflectivity is 1, but if the signal has to travel almost parallel to the ground to reach the surface, the reflectivity is close to zero. For angles in between 0 and $\pi/2$, the shape is a sinusoid.

Surface Code

When the data from the terrain surfaces and object surfaces is combined, the goal is to form the four arrays named at the top of section 2.2.3. Therefore the position and velocity arrays are reshaped to the shape $(n, 3)$, with n the number of surfaces and 3 for three dimensions. Area and reflectivity are one-dimensional arrays with length n. The attitude of the aircraft is used to construct Euler Matrices, with which all positions can be expressed in an aircraft-centered forward facing coordinate system. Since the reflectivity of the surface is dependent on its relative position to the radar system, it can only be computed after this step. The code for this is printed below in Code 2.4.

Code 2.4: Computing Surface Properties

```
import numpy as np
import Dynamics as dyn
import OtherAC
class Simulator:
 def Sim(self, PlatformState, **kwargs):
  # If other aircraft are included, they are in **
      kwargs
  # Unpacking the tuple
  OwnPos, OwnVel, OwnAttitude = PlatformState
  # Get Euler Matrix
  gr2ac = dyn.Euler(OwnAttitude)
  # Get Properties of Ground and Objects
  # 'Dist' and 'Vel' are shape (n,3)
  GrDist, GrVel, GrArea          = self.Terrain.
      Relative(OwnPos, OwnVel)
  AcDist, AcVel, AcArea, AcRefl = OtherAC.Relative(
      OwnPos,OwnVel,**kwargs)
  # Concatenate Surroundings Properties
  cc = np.concatenate
  Dist = cc((GrDist,AcDist), axis=0)
  Vel  = cc((GrVel ,AcVel ), axis=0)
```

```
    Area = cc((GrArea,AcArea), axis=0)
    # Rotate Surroundings to AC reference system
    Dist = dyn.Rotate(Dist,gr2ac)
    Vel  = dyn.Rotate(Vel ,gr2ac)
    # Compute Terrain Reflectivity, only for the Ground
        surfaces
    GrRefl = self.Terrain.Reflection(Dist[:GrDist.size
        ,:])
    Refl = cc((GrRefl,AcRefl), axis=0)
    ...
    return SimOutput
```

2.2.4. Antenna Simulation

When all the important properties of the surfaces around the radar have been determined, it is time to apply the radar equation and to simulate the antenna outcome. But before that, first all the surfaces which are outside of the range of the radar are eliminated from the simulation, as well as the points behind the radar. After the surface list has been reduced, it is time to perform the computations with a higher CPU load, to compute the range, elevation and azimuth of the surfaces. Finally, the Radar Equation (equation 2.4) can be applied to compute the Received Power from each surface. After that, the Doppler velocity of each surface is computed by projecting the Vel vector onto the $Dist$ vector. These steps can be seen in code 2.5:

Code 2.5: Removing Irrelevant Surfaces and computing Received Power

```
import numpy as np
class Simulator:
 def Sim(self, PlatformState, **kwargs):
  ...
  # Define filter criteria
  cr1 = np.sum(Dist**2,axis=0)<self.HW.Raxis[-1]**2
  cr2 = Dist[:,0]>0
  inrange = np.where(cr1 * cr2)
  Dist = Dist[inrange]
  Vel  = Vel[inrange]
  Area = Area[inrange]
  Refl = Refl[inrange]
  # High CPU computations
  Range     =np.sqrt(np.sum(Dist**2,axis=0))
  Elevation =np.arctan2(dist[:,2],dist[:,0])
  Azimuth   =np.arctan2(dist[:,1],dist[:,0])
  # Radar Equation
  Gain =self.HW.AntennaGain(Azimuth,Elevation)
  Power=(10**(Gain/10))**2*10**(self.HW.Pe/10)
  Pr = Power * Refl * Area * self.HW.l**2 / ((4*np.pi)
      **3 * Range**4)
  # Doppler Velocity
  Doppler=np.sum(Dist*Vel,axis=1)/Range
  ...
```

With these steps, the signal strength from each surface is computed. But for a complete simulation, it is important to compute the phase of an incoming signal as well, since the phase of two different signals is important for the summation of the sinusoids: when two signals are in counterphase, they cancel each other. Also, many radar applications consist of multiple receiving antennas in each others vicinity, such that phase differences can be used to determine the direction of an incoming signal [10–12].

To compute the strength and phase of the surface reflections, it is necessary to find the exact distance between the receiving antennas and the reflecting surface. For this purpose, a third dimension is added to the numpy array $Dist$. The dimensions of this array are now $(surface, 3Ddimension, antenna)$, with the shape $(n_1, 3, 1)$. The antenna receiver positions (a property of the Hardware object) will then be an array with shape $(1, 3, n_2)$. If these arrays are subtracted and the Euclidean norm is taken over the second dimension, the result will be an array with distances and the shape is (n_1, n_2).

When the distance to each antenna is found, the modulo of this distance divided by the wavelength will result in a phase which is different for each antenna. This phase is in the range $[0, \pi]$. The code for computing the strength and phase for each antenna is given in code 2.6:

Code 2.6: Computing the phase for each Rx antenna

```
import numpy as np
class Simulator:
 def Sim(self, PlatformState, **kwargs):
  ...
  # Compute the Range from surface to Rx
  DRx = Dist.reshape((-1,3,1)) - self.HW.RxDist
  RangeRx=np.sqrt(np.sum(DRx**2,axis=1)
  # Find Phase
  Phase=np.mod((Range+RangeRx)/self.HW.l,1)*2*np.pi
  ...
```

2.2.5. Radar Image Construction

Now that the strength and phase are known for all reflective surfaces and all antennas, it is time to combine those in an image for the radar output. This will be a three dimensional matrix, with axes 0 and 1 being the $Raxis$ and $Vaxis$ as computed in code 2.2. Axis 2 will be the antenna axis, so in the end there will be an $R \times V_R$ matrix for each antenna.

In order to add the sinusoids to each other, use will be made of Euler's formula, $e^{ix} = \cos x + i \sin x$. In this way, reflections from surfaces can be summed without having to compute all the sine functions, speeding up the simulation. Also, for each surface it must be computed in which pixel of the $R - V_R$ image the reflection will appear.

Code 2.7: Computing the complex value of the Signal

```
import numpy as np
class Simulator:
 def Sim(self, PlatformState, **kwargs):
  ...
  # Complex signal value for each surf+Rx
  Signal = np.exp(1j*Phase) * Pr.reshape(-1,1)
  # Where in the image does the surface belong
  Rindex = np.int(Range/self.HW.dR)
  Vindex = np.int((Doppler-self.HW.VLim)/self.HD.dV)
  # Maybe Vindex is outside of Nyquist range
  Vindex = np.mod(Vindex,self.HW.nR)
  ...
```

At this point, the simulator has three important numpy arrays: the $Signal$ array of shape $(surfaces, antennas)$, and two arrays $Rindex$ and $Vindex$ that indicate where in the final matrix the $Signal$ value should be found. Now it is time to map the surface values to the correct pixels.

There is one challenge to bear in mind: multiple surfaces may end up in the same pixel in the reflection image, since they may represent surfaces at different places but with the same range and Doppler velocity with respect to the radar. So the mapping is not necessary one-to-one, which can cause errors when executing the software.

The fastest solution that was found, was to make use of the $np.unique$ function, which can find all unique values in an array in a computationally efficient way. In this way, all of the unique values can be mapped to the output array at once, and after cleaning up the $Signal$ array, the remaining $np.unique$ values can be added to the array. In this way, it was found that typically about 8 iterations were necessary to process the entire $Signal$ array, making it the fastest solution that was found.

At the last step of the simulation, randomly generated complex noise is added to the output, having an amplitude of $NoisePWR$. The entire process can be seen in code 2.8:

Code 2.8: Constructing the Output matrix

```
import numpy as np
class Simulator:
 def Sim(self, PlatformState, **kwargs):
  ...
  FlatIndex=(Rindex+Dindex*self.HW.nR)
  Output=np.zeros((self.HW.nR*self.HW.nV, self.HW.
      nAntennas),dtype = np.complex)

  while FlatIndex.shape[0]:
   FIUnique, Idxs = np.unique(FlatIndex,return_index=
       True)
   Output[FIUnique,:] = Output[FIUnique,:] + Signal[
       Idxs,:]
   Signal   =np.delete(Signal,Idxs,axis=0)
   FlatIndex=np.delete(FlatIndex,Indices,axis=0)
```

```
    ResShp = (self.HW.nV,self.HW.nR,self.HW.nAntennas)
    SimOutput=Output.reshape(ResShp)
    Noise = NoisePWR*np.exp(1j*np.random.random_sample(
        ResShp)*2*np.pi)
    Simoutput = Simoutput + Noise
    return SimOutput
```


Now the simulator returns a complex output matrix which represents all the observed signals. But the complex values are difficult to visualize in an image. So in order to inspect the signals, an additional operation is required. In code 2.9 this is displayed, and it can be seen that it is possible to display the signal strength of each pixel (in dB) or its phase (in radians).

Code 2.9: Visualizing Simualtion Results

```
import matplotlib.pyplot as plt
import numpy as np
def ShowStrength(SimOutput,Rx):
 # Compute the strength in deciBel
 val = np.abs(SimOutput[:,:,Rx])
 valdB = 10 * np.log10(val)
 Plot(valdB,0,50)

def ShowPhase(SimOutput,Rx1,Rx2):
 # Compute the phase difference between two Rx
 ph = np.angle(SimOutput[:,:,Rx1]) - np.angle(
     SimOutput[:,:,Rx2])
 ph = np.mod(ph, 2*np.pi)
 Plot(ph, 0, 2*np.pi)

def Plot(data,v1,v2):
 # Show the image
 ax = plt.figure()
 limits = [-self.HW.VLim, self.HW.VLim, self.HW.RLim,
     0]
 ax.set_xlim(limits[:2])
 ax.set_ylim(limits[2:])
 ax.imshow(plt.cmap(data),vmin=v1,vmax=v2,extent=
     limits,aspect='auto',origin='upper',interpolation
     ='none')
 plt.show()
```

2.3. Simulator Output

In this section resulting images from the FMCW radar simulator are shown and discussed. By changing input parameters, the output figures change as well. These differences are used to verify the functioning of the software.

The first image shown is the result of simulating the aircraft at 1000 meters height above a flat plane, flying with a velocity of 30 meters per second. Another aircraft is included in the simulation. This aircraft flies heads on to the radar with a velocity of 30 meters per second, equal to the platform velocity. The other aircraft

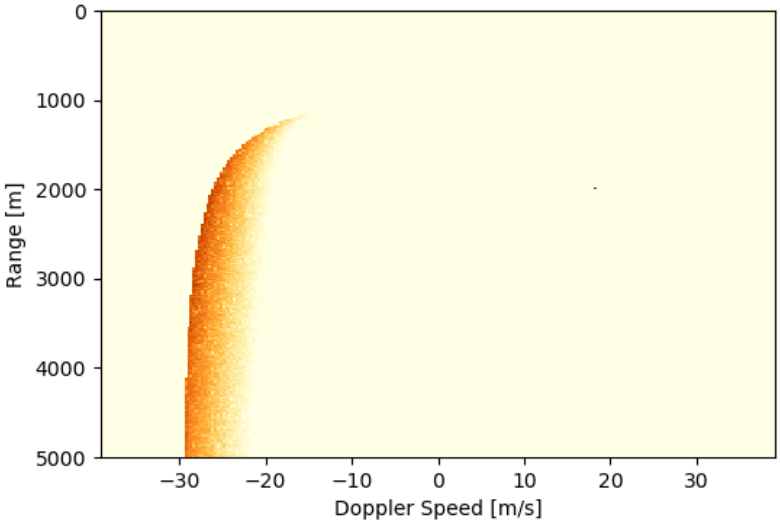

Figure 2.3: Simulator Strength Results at 1000m height and 30m/s velocity, with another aircraft at 2000m distance. The dark regions indicate where a strong signal is received. Apart from the large region, a signal is seen at $R = 2000m$, $V = 20m/s$

is at a distance of 2000 meters, and the simulated radar reflections can be seen in Figure 2.3:

When looking at Figure 2.3, several observations can be made. A coloured shape is drawn on a black background. The bright colours indicate strong radar signals, so this shape must resemble the ground reflections.

The ground reflections appear to have two asymptotes. One asymptote in vertical direction, which seems to be exactly on the line $V_{Doppler} = -30m/s$. This makes sense, since it is not possible to observe velocities of more than the aircraft speed if the rest of the world is stationary. The other asymptote is the horizontal one, with $R = 1000m$. This also makes sense: if the aircraft is 1 kilometer above the ground, reflections from closer than 1000 meters are not expected.

The Doppler values are negative because the simulated antenna is pointed forward. So all ground reflections are moving towards the aircraft, as seen from the perspective of the radar. Since the range is positive, it follows that this Doppler speed is negative.

As seen in Figure 2.3, the extra aircraft is plotted as a bright pixel at 2000m distance, with a radial velocity of about $+20$ meters per second. This is an alias of the true Doppler velocity of -60 meters per second, as will be discussed in the next example.

In the second image, seen in Figure 2.4, the aircraft is set to have a velocity of 60 meters per second. This velocity causes a Doppler frequency shift which is more than the Nyquist frequency (the largest unambiguous Doppler frequency) [13], so

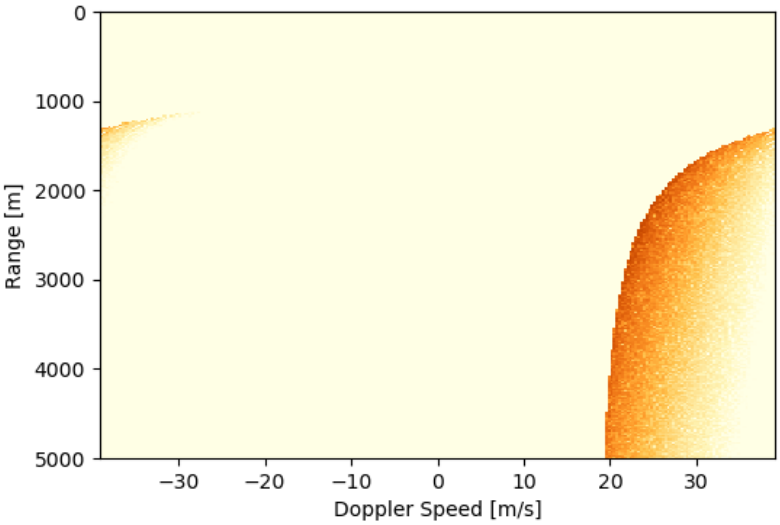

Figure 2.4: Simulator Strength Results at 1000m height and 60m/s velocity. The dark area indicates from where strong signals are received. The area appears to be 'cut in two' on the left and right side of the image.

the signal is undersampled and one of its aliases is observed. This is seen in Figure 2.4, in which the coloured shape is seen on the right hand side of the image.

In fact, the ground reflections are plotted on the right hand side, but this is the alias of the original signal. As can be seen, the horizontal axis ranges from about -40 to +40 meters per second Doppler speed. The values for the ground reflections, which should originally be plotted at -60 meters per second, appear now 20m/s from the right hand side of the image, as if the two edges are connected. The edges do also appear to be connected, because the reflections at +40m/s and -40m/s appear to connect well to each other. This is exactly what is expected to happen when Doppler shifts occur which are greater than the Nyquist frequency. To reduce this effect, it is possible to increase the sampling rate, but this does have computational consequences and may require more expensive hardware.

To measure the speed of the simulator, the radar results of a complete flight were simulated. The flight was previously recorded by a pilot in a flight simulator and consists of 727 samples. The simulation of the radar results that correspond to those 727 aircraft states took 219 seconds, which is equivalent to 3.3 radar simulations per second, performed on a personal computer. The most important contribution to the length of this computation time is the amount of ground data points simulated, which all need to be mapped to the Range-Doppler image.

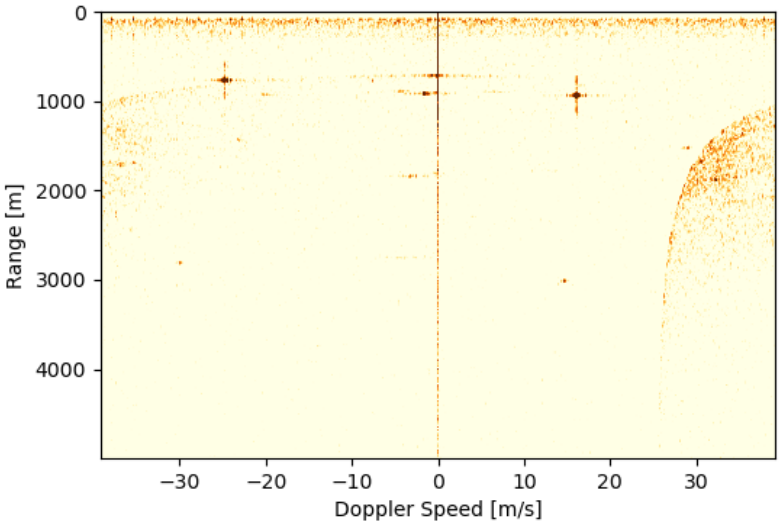

Figure 2.5: Hardware Strength Results at 744m height and 53m/s velocity. It is seen that a similar curved shape is visible as in the simulated results, but there are other signal reflections which were not seen in simulations.

2.4. Comparison to Actual Radar Data

In order to verify that the radar simulator works properly, the simulated results are compared to those of test flights. These flights are performed with a prototype of the radar, of which the specifications are described in section 2.2.2. The flight was performed at the airfield of Deelen in the Netherlands.

The radar was recording during the entire flight, resulting in 22342 measurements. The radar data of the entire flight was processed. The results of measurement number 11171 are shown below. The measurement number was chosen to be in the middle of the flight. At that time, the aircraft was flying with a ground speed of 53 meters per second, and the height was 744 meters. The signal strength results are shown in Figure 2.5.

In Figure 2.5 it can be seen that the strength results measured in a flight resemble those simulated by the software. The shape of the ground reflections is observed by simulations and when hardware tests are performed as well. Also, the ground reflections are plotted on the right hand side of the Figure when the Doppler frequency becomes more then the Nyquist frequency. This was also seen in the simulator.

Some differences are also observed: in the strength plot in Figure 2.5, the shape of the ground reflections is smaller than seen in the simulations. A number of bright spots are observed in the image as well. These spots are present for all 22342 measurements of the flight. Also, signal reflections are observed for all velocities at about a range of 100 meters. The vertical line of zero meters per second does

also have a high signal strength, which was not observed in the simulations. The differences between the simulator results and hardware results are discussed in the next section.

2.5. Discussion

In the previous sections a radar simulator algorithm was presented and the simulator output was compared to recorded data from an actual radar in flight. In this section the differences between the results are discussed.

The first apparent difference from simulated results as seen in Figures 2.3 and 2.4 on the one hand, and Figure 2.5 on the other hand, is the size of the shape of the ground reflections, which is smaller in the real radar results than in the simulations. This means that the received signals are not as strong in reality as in the simulations. This can be caused if the emitted power is not as much as the hardware specifications implied. Another option is the loss factor in Equation 2.4, which was assumed to be 1. Signal losses can be caused by atmospheric parameters. Another option can be that the strategy of combining the azimuth and elevation axis is inaccurate.

Another observation is about the presence of the strong signal spots in Figure 2.5. These spots are known as spurs and can be caused by self-interference of the radar system. This explains why they are present in all measurements in the flight. Spurs are commonly seen in radar applications, and they are very dependent on the exact hardware setup. Therefore they can only be included in the simulation results after their locations have been measured in hardware experiments. The vertical line in the hardware results is also a consequence of self-interference of the radar system.

Despite these differences, it is seen that the radar simulator is generally accurate in simulating surface reflections around the system. This makes the simulator useful for research and development purposes of microwave sensing applications. The differences in simulator output and test results can be explained by hardware inaccuracies and modeling errors. It is expected that after performing a test with the real hardware it is possible to calibrate the simulator. With this step, gain modeling errors can be taken into account and the presence of spurs can be included in the simulation.

2.6. Conclusion

A detect and avoid radar is developed for use in General Aviation. Research is required in order to assess its strengths and weaknesses, such as presented in chapters 3, 5 and 6 of this dissertation. Experiments must be done for the research, but flight tests are costly in both financial and logistical aspects.

Computer tests can provide an affordable alternative to flight tests. Therefore a model is developed with which the output of the radar system can be simulated. The code used for the simulator, written in Python, is provided in this chapter. Its general structure is presented and the different sections are discussed in detail. The simulator can perform several complete cycles per second when ran on a personal

computer, which indicates that it can be used in offline studies for quick development cycles. The simulation output is given as complex numbers of which both the modulus and the argument are considered.

Results of the simulator are compared to those of a flight test of the hardware prototype. It was found that the patterns visible in simulation plots are also seen in real collected radar data. Differences were also observed, like the presence of spurs and background noise. If these are modeled accurately, they can be included in the algorithm. Overall, it can be said that the radar simulator can be used in a microwave sensing project to help with the design and implementation of hardware and software. This simulator has indeed been used in the research for chapters 3, 5 and 6 of this dissertation.

References

[1] R. O. Chavez-Garcia and O. Aycard, *Multiple Sensor Fusion and Classification for Moving Object Detection and Tracking,* IEEE Transactions on Intelligent Transportation Systems **17**, 525 (2015).

[2] Z. Zhang, Z. Tian, B. Zhang, W. Hong, Y. Wu, and L. Li, *Multi-channel SAR covariance matrix estimation based on compressive covariance sensing,* in *2016 4th International Workshop on Compressed Sensing Theory and its Applications to Radar, Sonar and Remote Sensing, CoSeRa 2016*, CoSeRa (2016) pp. 37–41.

[3] F. Biondi, *Super resolution of synthetic aperture radar data by convex optimization,* in *4th International Workshop on Compressed Sensing Theory and its Applications to Radar, Sonar and Remote Sensing*, CoSeRa (2016) pp. 28–32.

[4] C. Naulais, *General Aviation Radar System for Navigation and Attitude Determination*, Ph.D. thesis, Technische Universiteit Delft (2015).

[5] J. Maas, R. V. Gent, and J. M. Hoekstra, *Estimation of Flight State with a Collision Alert Radar,* AIAA Journal of Aerospace Systems , 1 (2021).

[6] J. Maas, R. V. Gent, and J. Hoekstra, *Object Tracking in Images of an Airborne Wide Angle FMCW Radar,* in *ICRAT International Conference for Research in Air Transportation* (2018) p. 8.

[7] J. Maas, V. Stefanovici, R. V. Gent, and J. Hoekstra, *Validation of GPS by Ground Scanning Radar,* in *ICRAT International Conference for Research in Air Transportation* (2020) pp. 1–8.

[8] S. Rao, *Introduction to mmwave Sensing: FMCW Radars,* (2017).

[9] A. Meta, *Signal Processing of FMCW Synthetic Aperture Radar Data* (TU Delft, 2006) p. 133.

[10] A. K. Shaw, *Improved Wideband DOA Estimation Using Modified TOPS (mTOPS) Algorithm,* IEEE Signal Processing Letters **23**, 1697 (2016).

[11] A. Paulraj and T. Kailath, *Direction of arrival estimation by eigenstructure methods with unknown sensor gain and phase,* Acoustics, Speech, and Signal Processing, IEEE International Conference on ICASSP '85. **10**, 640 (1985).

[12] W. Li, J. Lin, W. Wang, Y. Wang, and Z. Chen, *Method of multi-channel calibration for digital array radar,* in *European Radar Conference* (2015) pp. 533–536.

[13] D. Koks, *How to Create and Manipulate Radar Range-Doppler Plots*, Tech. Rep. (Defence Science and Technology Organisation, Edinburgh, 2014).

3

A Portable Primary Radar for General Aviation

J Maas, R Van Gent, J Hoekstra

The simulator from chapter 2 is used to develop fast versions of signal processing algorithms that can be used to display the radar output in real time. Now the radar is tested in a field experiment. During this experiment, the radar is stationary on an airfield, aimed to the sky. A test aircraft passes over the radar setup, and it carries a gps device that logs its position.

In this chapter the signal processing algorithms and the experiment are presented. It is found that the radar is capable of accurately determining the aircraft position in three dimensions up to 3 kilometers distance.

This chapter is based on the publication *A Portable Primary Radar for General Aviation*, PLoS ONE 15(10), 2020

3.1. Introduction

In order to guarantee safe flight, it is essential to be aware of the environment around the aircraft in aviation. Lethal collisions can happen in General Aviation (GA) when pilots flying under Visual Flight Rules (VFR) are confronted with unexpected Instrument Meteorological Conditions (IMC), which limit the vision of a pilot [1, 2]. The detection of hazards around the aircraft may also be hindered by glare from the sun, the position of the own wings, or the size and attitude of the object [3]. On top of that, the development of Unmanned Aerial Systems (UAS) is expected to lead to an increase in traffic in uncontrolled airspace, where conflicts between partakers will occur more and more frequently [4]. Air Traffic Control (ATC) may not be present to guarantee safety, according to the plans for the future development of air traffic management [5, 6]. Therefore, reliable local methods for providing situation awareness are required.

Technical solutions have been sought to improve situation awareness. Devices such as Traffic Collision Avoidance System (TCAS) and Flarm can give pilots proximity warnings and even resolution advisories[7, 8], but the systems can be expensive, specifically for GA. Moreover: these systems are transponder-based and are therefore dependent on the presence of a transponder in the target aircraft. Towers, mountains and aircraft that do not carry the proper hardware are invisible for these systems and a pilot relying on them may perceive a false sense of safety. An independent solution for objects surveillance in an aircraft's vicinity has not yet been found.

A hypothetical ideal solution would be to take a high-tech version of an airport surveillance radar on board of an aircraft. These systems, of which the first were built in the 1950's, can independently detect a multitude of objects around an airport, whether transponder-equipped or not. Tuning of ground radar systems can empower them to observe even birds or rain clouds. With a system like this, the situational awareness of a pilot could be enhanced to a great extent. However, airport surveillance radars are too big and heavy to be carried on board of GA aircraft, and they consume more power than what a typical GA aircraft can provide. Also, the price of such a system is too steep to be considered for a regular GA aircraft owner. Moreover: these radars only provide 2D information about objects; altitude information is usually gathered by the aircraft transponder in Mode C or Mode S, for which a Secondary Surveillance Radar is required. Therefore, airport surveillance radars are unsuitable for taking on board of GA aircraft.

But recent developments in radar hardware have improved the specifications to a point where it is possible to build small low-power radar systems. In the 1970's, marine radars have been introduced that can be taken on board of boats to improve the situational awareness, and in the early 2010's, bird radar systems have been designed and built at airports. The present-day interest in self-driving cars have instigated a renewed focus on radar sensing [9–11]. This applies to hardware manufacturers that aim to improve specifications such as accuracy, weight and power consumption for a better cost, and it applies to scientists that use modern computational power to find new data processing algorithms to improve the results [12]. DIY-radio hardware that can match professional Automatic Dependent

Surveillance Broadcast (ADS-B) receivers can be bought for use at home for less than the price of a computer, and the size of radar antennas is small enough to be fitted behind the front bumper of a self-driving car[9, 11]. It has become possible to design hardware for sense-and-avoid purposes on board of a GA aircraft.

This new hardware also brings new scientific challenges, since aviation is different from road traffic or shipping. A notable difference is the presence of a vertical dimension: while road traffic and shipping take place on the surface of the earth - an approximate two-dimensional plane - aviation is performed in the three-dimensional airspace above it. This means that objects of interest for the pilot can come from many different directions and that for any object, its location must therefore be determined in three dimensions. This task is complicated by the attitude of the aircraft itself, which can vary along three axes as well. Also, the presence of driving lanes cannot be assumed in aviation. This means that simplifications that are useful in head-tail collision prevention for car traffic, will not hold in flight. Further, aviation takes place on a larger scale than road traffic, with larger distances and higher velocities. This will not impact the theoretical limits since better hardware can be bought to overcome larger distances, but advanced software is necessary to improve accuracy in order to keep the hardware affordable for GA aircraft. These examples show that new research is required before sense-and-avoid radar systems can be put into use in aviation.

In this chapter, the results are presented of multiple experiments that work towards the goal of developing a portable radar system for local surveillance. The focus of this chapter is on the detection of objects in the radar output, and on finding their locations in 3D space. In section 3.2, the hardware used in this research is described and the relevant theory is introduced. The algorithm for detecting the object pixels in the radar image is described in section 3.3, and the strategy of three-dimensional localization is described in section 3.4. These two sections are illustrated on the basis of a simple static experiment, but a dynamic experiment is also carried out to assess the performance of the radar. This experiment is described in section 3.5, and its results are presented in section 3.6. A discussion about the results can be found in section 3.7, and conclusions about the experiments are found in section 3.8.

3.2. Hardware

In this section, the hardware used in this research is described, as well as the theoretic principles that form its scientific foundation. Three sub-sections are used for this. The theoretic principles and the resulting radar image are introduced in section 3.2.1. The issue of aliasing is introduced in section 3.2.2. In section 3.2.3, an overview is given for the steps necessary for object detection in GA.

The radar is constructed by the company MetaSensing Radar Solutions in Noordwijk, the Netherlands. Its technical specifications are listed in table 3.1. An image of the hardware used in this research is seen in figure 3.1. The radar and its power supply fit within the trunk of a passenger car, as seen in the image. In this research, the radar was always operated from within the trunk of this car.

Table 3.1: Technical Specifications of the Radar Hardware

Parameter	Symbol	Value
Carrier Frequency	f_c	$9.425\ GHz$
Wavelength	λ	$31.83\ mm$
Sampling Frequency	f_s	$10\ MHz$
Pulse Repetition Frequency	PRF	$4921\ Hz$
Power Emitted	P_e	$40\ dBm$
Bandwidth	B	$10\ MHz$

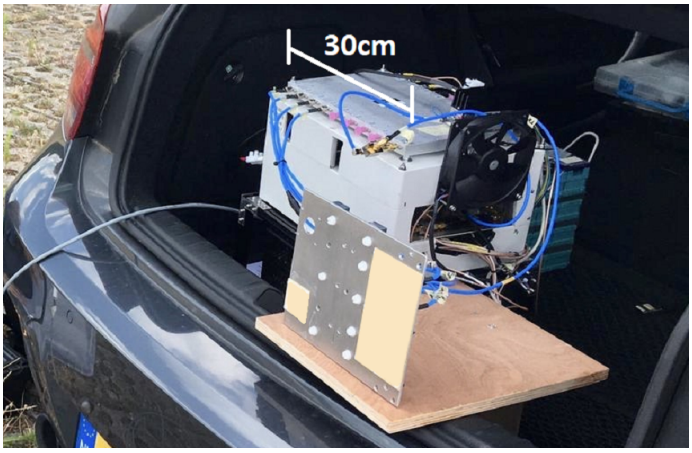

Figure 3.1: The hardware setup used in this research

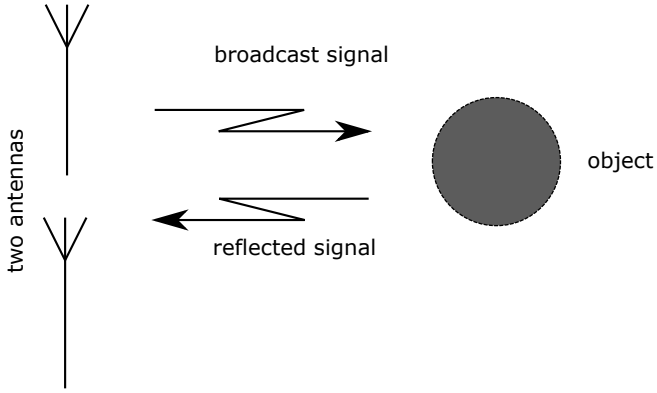

Figure 3.2: Transmission and reflection of a radar signal

3.2.1. Principles of FMCW Radar

A modern Frequency Modulated Continuous Wave (FMCW) radar is used for this research. These radars transmit a non-stop signal, of which the frequency is varied around a central value. The signals are broadcast to the surroundings of the radar, reflect on present surfaces and are received again by the antennas of the system. The received signal is compared to the transmitted one, and the differences can be used to compute the time delay and Doppler shifts of the received signal. From these, the distance to the target and the radial velocity of the target can be found, respectively.[13, 14]. This principle is illustrated in figures 3.2 and 3.3. FMCW radars can be built with inexpensive hardware, since the frequencies which are observed are lower. Because a continuous signal is transmitted, the power consumption of an FMCW radar is lower than that of a pulse radar. These properties make FMCW radar suitable for GA applications.

As can be seen in figure 3.3, the shape of the frequency modulation facilitates a comparison between the broadcast and received signal. The time shift that is found can be used to compute the range to the object. Since the radar signals travel with the speed of light, the range to the object (R) can be found with equation 3.1, in which Δt is the round trip time delay and c the speed of light.

$$R = \frac{c \cdot \Delta t}{2} \tag{3.1}$$

The vertical shift between the original and received signal is a consequence of the Doppler effect. This is caused by the objects moving relative to each other in longitudinal direction. Therefore, if the object is moving towards the radar or away from the radar, this will be visible in the Doppler results. A sideways movement will not result in a Doppler shift. Since the velocity of moving objects is negligible with respect to the radio propagation speed, the radial velocity (V_R) can be found using equation 3.2.

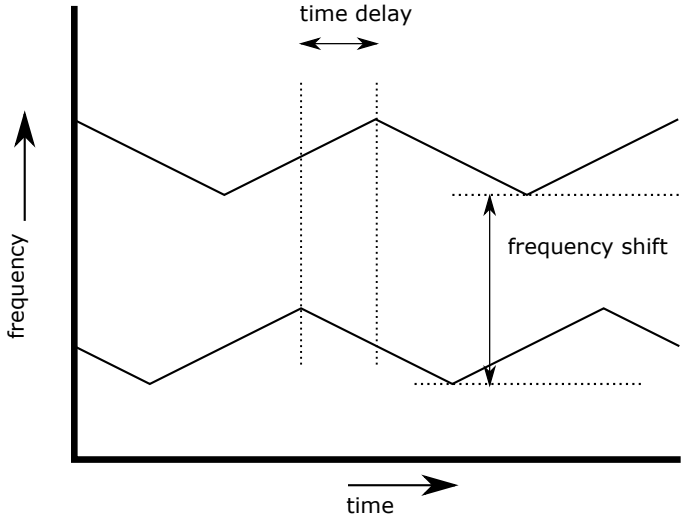

Figure 3.3: Differences between transmitted and received signals

$$V_R = \frac{\Delta f}{f_c} \cdot c \tag{3.2}$$

In equation 3.2, the frequency difference is denoted by Δf and f_c is the transmitted center frequency.

When operating, the radar will receive a multitude of reflections from surfaces in its vicinity. All these reflections are sensed by the same antenna, so the resulting input signal is an addition of all reflections. The input signal is converted from analog to digital and a Fourier analysis is performed to reconstruct the reflections. For each of the components of the Fourier result, the values for R and V_R are found as well as the amplitude of the sinusoid. These three parameters are used to construct a greyscale radar image, in which R and V_R form the pixel coordinates, and the intensity of the signal is used for the pixel intensity. An illustration of a radar image can be found in figure 3.4, in which the axes are illustrated, as well as the way how to find the R and V_R values of a pixel of interest.

3.2.2. Aliasing

When an analog signal is sampled and converted to digital values, it is impossible to determine the exact original frequency. This is because of the phenomenon of aliasing. This means that two sinusoidal signals which differ in frequency with an exact amount, can not be separated from one another. This can be illustrated with an example of a moving disc, as can be seen in figure 3.5. In this example, three discs rotate with different rotational velocities. If a picture is taken of these discs at the right moment, when they performed half a revolution clockwise or counterclockwise, the pictures will be identical, and it is not possible to determine the rotational velocity uniquely. [15]

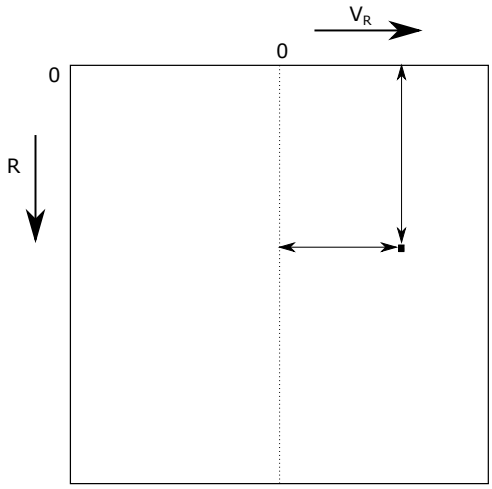

Figure 3.4: The axes of a radar image and how to read pixel coordinates. The range of a pixel is given by the vertical axis, the Doppler velocity is indicated by the horizontal axis.

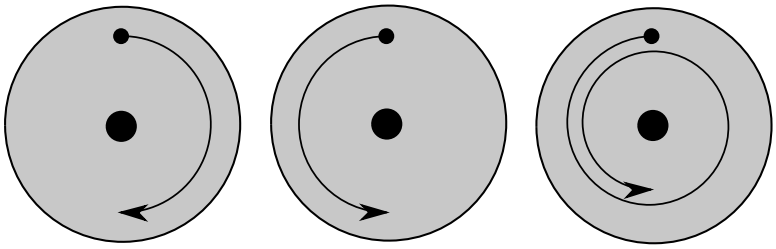

Figure 3.5: Three rotating discs that are observed to be equal when sampled at the correct frequency

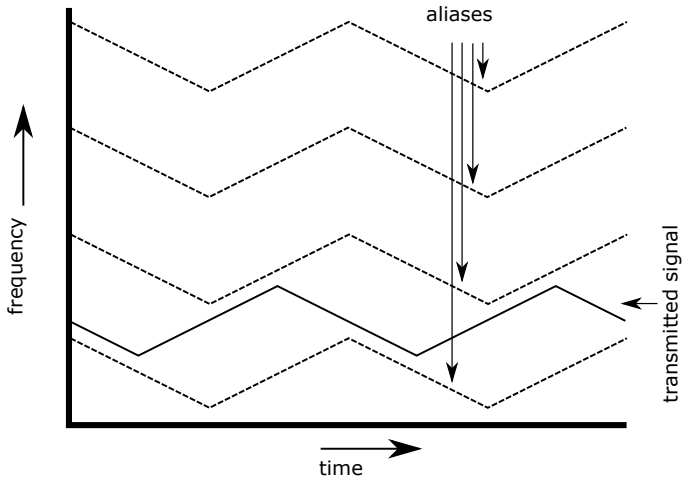

Figure 3.6: Aliases of an observed signal. The four dashed lines are offset by a constant frequency. They are equivalent reflections of the transmitted signal.

In the example of the FMCW radar, it means that the incoming signal can be observed with different frequencies. This means that multiple solutions are found when determining the Doppler shift of the incoming signal, and that the radial velocity of an object does not have a unique solution. In figure 3.6, an observed signal is plotted in a dotted line, next to three of its aliases. As can be seen, it is not possible to determine which is the real signal and which are the aliases.

A solution to aliasing can be to increase the sampling frequency of the system. The difference between two aliases is equal to the sample frequency, so if this frequency is large, there is less possibility of signals being mistaken for one another. Another solution can be to decrease the center frequency of the transmitted signal, denoted as f_0 in equation 3.2. This means that for a given V_R, the shift in frequency is also lower and it is less likely to get confused by aliases. Therefore the bandwidth of one alias is higher, and a higher value of V_R should occur in the test before the bandwidth is surpassed, as discussed in [16].

To completely prevent aliasing from existing, an infinite sampling rate is required. This is not possible, and a finite sampling rate will have to do. The sampling rate is limited by the quality and cost of available hardware, bearing in mind that the system is developed for use in GA and reductions in cost are desirable. Also, the center frequency used by the system is constrained, determined by bandwidth constraints by communication authorities. It is therefore not possible to completely prevent the occurrence of aliases in this hardware.

In the radar image shown in figure 3.4, aliasing will have as a consequence that the horizontal edges of the figure are adjacent to one another. This is illustrated in figure 3.7, where the motion of an object is indicated in the radar image by a series of black dots. If the radial velocity of the object would increase to an amount that it would surpass the maximum limit of the horizontal axis, it would reappear on the

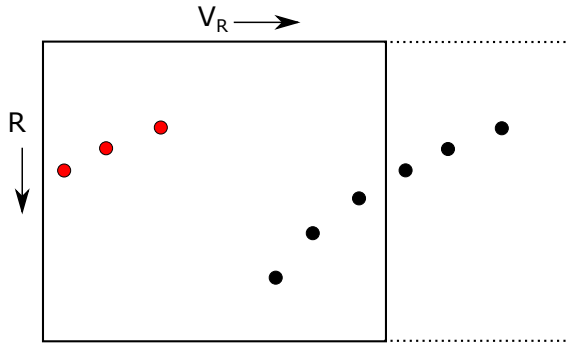

Figure 3.7: Aliases in the radar image

other side of the image, as denoted by the red dots in the figure.

It is possible to solve the issue of aliasing. A solution is to use known information about the objects that are to be observed. It is also possible to use a series of observations in which the object is tracked over multiple time instances. If this is done, the change in range R can be used to validate the value of the radial velocity V_R, as performed in [17].

As discussed above, the real signal and its alias cannot be distinguished from one another by instantaneous observation. Since the focus of this chapter is on the detection of objects, it does not matter whether the original signal or one of its aliases is detected. In this work, aliasing is solved afterwards, by knowledge of the state of the other object, as will be discussed in section 3.5.

3.2.3. Steps required for Sense-and-Avoid

The radar image, as presented in figure 3.4, is two-dimensional - with only one distance dimension. Aviation is three-dimensional, so more information is required to adequately notify the pilot of objects in the vicinity of the aircraft.[1]. It is possible to find more information about the state of any object that appears in the radar image.

Direction of Arrival determination algorithms exist, which can be used to determine the direction of an incoming signal. When this direction is known and the radar image provides the distance information R, the exact location of the other object can be found in three dimensions. Since the radial velocity V_R is measured, this can even give an indication of whether or not the other object is approaching the aircraft or not. To provide optimal information for the pilot, three-dimensional Direction of Arrival estimation is performed.

After the exact locations of objects are determined in one instance, a filter can be applied to remove reflections from the ground, such that only airborne objects and towers remain in the selection. The next step is to track the movement of the objects' locations through time. This can happen either in the radar image, where

[1]Of course, one-dimensional safety measures do exist in aviation, such as vertical separation for air traffic and the TCAS-II [7, 18, 19]

the pixel needs to be tracked [17], or in three dimensional space, in such a way that the locations of the objects should first be determined before they are tracked.

When tracking is done, the next step is to predict the future track of the object. Predictions can be made based solely on the current state of the aircraft, extrapolating the current speed vector. The terrain around the aircraft may also be taken into account in the predictions of the other aircraft, as well as the local VFR flight routes. When predictions are made, conflicts between the own aircraft speed vector and the predicted other tracks can be detected. These conflicts can be presented to the pilot as is, or a conflict resolution advice may be included, assisting the pilot by providing a suggestion for safety.

Together, the aforementioned steps are as follows:

- Data acquisition
- Radar image construction
- Pixel detection (This work, section 3.3)
- Direction of Arrival estimation (This work, section 3.4)
- Ground filtering
- Object tracking
- Conflict detection
- Resolution advice

3.3. Pixel Detection

In this section it is described how the detection of objects of interest is performed in the radar image. In 3.3.1, it is discussed what an object is expected to look like in the radar image. The state of the art of existing object recognition software is discussed in section 3.3.2 and algorithms to perform corner detection are discussed in section 3.3.3. A first field test is performed, which is used to verify the expectations from section 3.3.1. The test is described in section 3.3.4. The presence of spurious signals, and the strategy to cope with them, is discussed in section 3.3.5.

3.3.1. Appearance of Objects

It is important to consider what objects will look like when they appear in the radar image. In this section, the differences between radar images and optical images (pictures) are considered and described in detail.

Different axes for images

Since the radar image has the axes of range and radial velocity, radar images are fundamentally different from visual images that we are accustomed to. The two axes of a picture indicate where the object was relative to the camera when the picture was taken. Objects that are closer appear bigger on the image. In the radar

image, only one of the two axes relates to the position of an object. This is the range axis. This axis is also different from the two axes in pictures, which indicate the position of an object horizontally and vertically relative to the sensor.

The shape of the object will also differ in between the two images. In an optical image, a projection of the three-dimensional object is preserved, but this does not happen in the radar image.

Mapping to the R and V_R axes

When a signal is sampled with a frequency of $10MHz$, the distance that a radar signal travels between two samples is around $30m$. This means that the range resolution of the radar image will be about $15m$ per pixel, taking into account that the signal needs to travel in two directions. This means that for most GA aircraft, all reflective parts of the hull will fall within the same range bin in the image, so the reflection will be displayed as a single pixel in range direction. For larger objects, the reflection may be seen in several range bins.

For the velocity axis, it can be assumed that the entire object has the same velocity vector $\vec{V}$. Therefore the radial component of the velocity vector V_R will be equal for all reflecting surfaces, since the vector $\vec{R}$ is almost the same for the entire object. If the object comes close to the radar, small differences in V_R can be noticed as illustrated in figure 3.8.

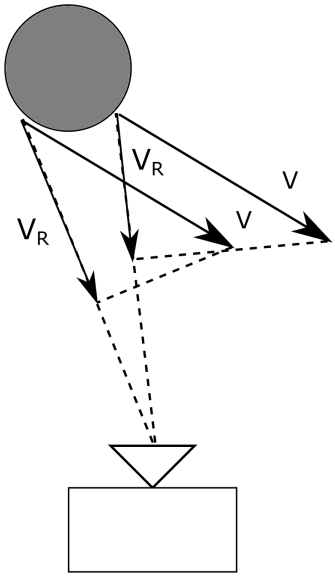

Figure 3.8: Two surfaces of an object close to the radar have a the same velocity $\vec{V}$ but different radial velocity V_R

Fourier analysis on a single signal

Combining the results from the previous two paragraphs, it is expected that an object is displayed in one single pixel in the radar image. It should be noted however,

that the exact range and radial velocity of the object will not be the precise center values of the pixel in the radar image. The consequences of this are illustrated in figure 3.9, where a one-dimensional Fourier analysis is performed on two sinusoids. The components of the two Fourier analyses are all integer frequencies. In subfigure 3.9a, it is seen that the exact frequency of $10\ Hz$, is seen as one single bar, a one-dimensional pixel. However, in subfigure 3.9b the frequency is not exactly the center frequency of a bin. So in this subfigure, the Fourier result is a sum of frequencies that lie around the original sinusoid of $10.1\ Hz$.

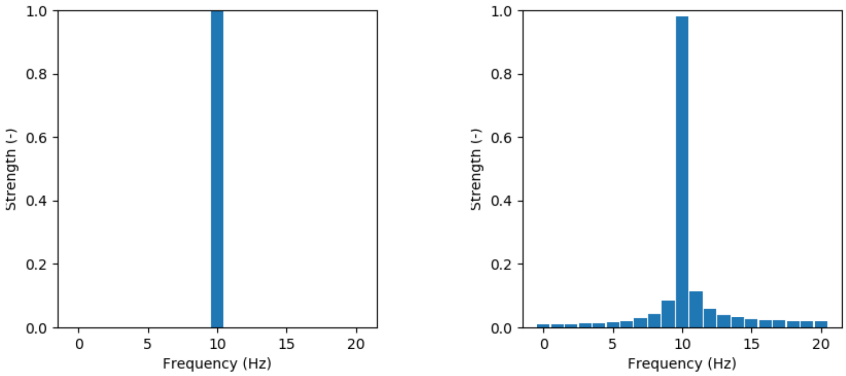

Figure 3.9: Bar graphs of one-dimensional Fourier results of two perfect sinusoids
A - $f = 10\ Hz$ B - $f = 10.1\ Hz$

The effect illustrated in figure 3.9 is representative for the effect in the radar image. Even though all reflective surfaces of an object may fall within the same R,V_R bin, the values will not be exactly the same as the center value of the pixel. Therefore, the Fourier analysis will yield a result where several nearby pixels are also illuminated. The pixel that the object falls in will still have the strongest signal.

The distance of the object will have an effect on two elements of its representation in the image. If the object is closer to the radar system, the distance is smaller and R will be smaller, so the location of the object will be more to the top of the image. Next to that, when an object is closer to the radar, its reflection will be stronger, so the pixels in the image will illuminate brighter.

Resulting appearance in radar image

Combining the considerations in section 3.3.1, it is possible to explain the appearance of objects in the radar image. In figure 3.10, a situation is drawn where an object is being observed by a camera or a radar. In figure 3.11, the resulting images of the camera and radar are drawn. It can be seen that in the optical image, the object is shown to the left, just as the situation in figure 3.10. Also, the object has the same shape as the original. In figure 3.11b, it is seen that the object is not seen as a round shape but as a small flock of illuminated pixels. Since the object is moving towards the sensor in figure 3.10, the flock is located on the left side of the image, where V_R is negative.

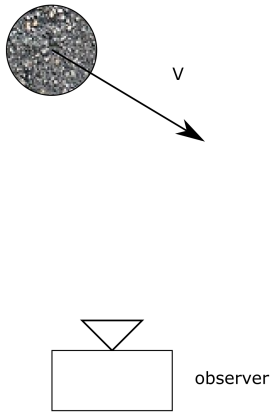

Figure 3.10: Top-down view of an object with speed vector $\vec{V}$ relative to an observer (camera or radar)

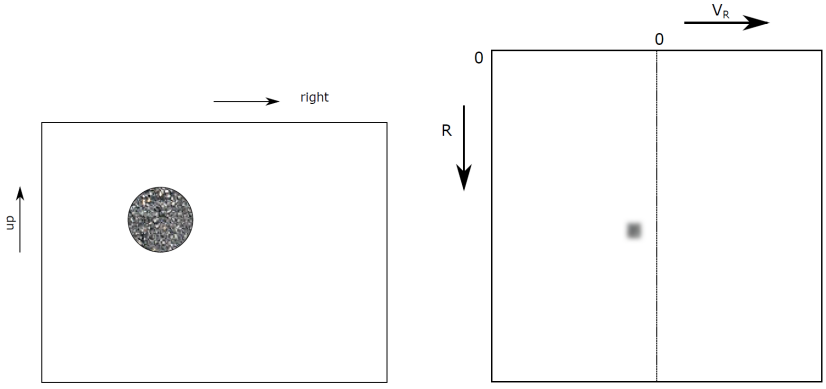

Figure 3.11: The object from figure 3.10 as seen in a visual image and a radar image
A - Camera Image B - Radar Image

3.3.2. Existing Software

Even though the radar image is unlike an optical image, much research that is performed to pictures is also applicable to radar images. The radar image is still a two-dimensional figure, in which objects are to be found which have a higher intensity than the background. This compares to finding the bright spots in a grayscale picture. It is therefore possible to base the detection of objects on existing research on visual images.

Modern visual algorithms are capable of more sophisticated tasks than finding bright spots in a grayscale picture. Recent scientific papers deal with detection of continuously changing shapes in coloured videos [20]. Classification of any objects is also performed, categorizing the objects by the hand of their features. This can include noisy images with low resolutions, or moving cameras [21]. Face recognition is also performed by modern software [22].

This does not mean that finding objects in the radar image is trivial. The most straightforward strategy is to define a threshold above which a detection is concluded. Since objects that are closer reflect stronger than objects far away and objects are visible in several pixels in the radar image, this can have as a consequence that multiple pixels surpass the threshold, and that one object is detected as more than one. This can be solved by only using the highest value of the flock of pixels, but if two objects are quite close to each other in the radar image, they may be perceived as being one object.

3.3.3. Corner Detection Algorithms

The solution to the problem from section 3.3.2 is to use a Corner Detection Algorithm. Corners are defined as locations in the image that have diverging values with respect to their immediate neighbours, in both the horizontal and vertical directions. Various algorithms for corner detection exist. These algorithms vary in accuracy, consistency and speed. A Harris Corner Detection algorithm[23, 24] is well-known and widespread, and multiple researchers have found it to be an excellent algorithm [25, 26]. The Shi-Tomasi algorithm is a variation of the Harris algorithm, which makes the corner detection more suitable for tracking over time [27, 28]. Since the Shi-Tomasi corner detection algorithm can be found in the widespread OpenCV library, it is chosen to use it for this research.

The corner detector is public knowledge and widely available. Nevertheless, the core elements of the algorithm are presented below. The starting point is to compute the auto-correlation of the greyscale image, where the value of each pixel is compared to those in its immediate vicinity, as in equation 3.3.

$$E_{\Delta x,\Delta y} = \sum_{x,y} w_{x,y}\big(I(x+\Delta x, y+\Delta y) - I(x,y)\big)^2 \tag{3.3}$$

In equation 3.3, the function $I(.)$ denotes the intensity of the greyscale image in a specific pixel coordinate. The function $w(.)$ is a windowing function with the output range between 0 and 1. Harris proposed to use a Gaussian smooth circular window, such that the response of the Corner Detection Algorithm would be invariable for rotation of the image.

Using a linear Taylor Series approximation and a linear matrix notation, equation 3.3 is rewritten to contain a matrix M:

$$E_{\Delta x,\Delta y} \approx [\Delta x \ \Delta y] \ \ M \begin{bmatrix} \Delta x \\ \Delta y \end{bmatrix} \tag{3.4}$$

In equation 3.4, M equals:

$$M = \sum_{x,y} w_{x,y} \begin{bmatrix} I_x I_x & I_x I_y \\ I_x I_y & I_y I_y \end{bmatrix} \tag{3.5}$$

In equation 3.5, the symbols I_x and I_y contain the image derivatives in x and y directions. As follows from equations 3.4 and 3.5, the covariance E of a single

pixel is directly dependent on M, which is different for each pixel. M has the advantage that it is not dependent on the values of Δx and Δy, only on the local image derivatives I_x and I_y and the window function w.

The strategy from Shi and Tomasi is to compute the eigenvalues λ_1 and λ_2 of the matrix M for each pixel. If both eigenvalues are higher than a threshold value, the pixel is considered a corner.

3.3.4. First Field Test

In order to prepare the experiments from section 3.5, a small field test is performed in which the radar was tested for the first time. This test takes place with a stationary radar on the ground. The location was in a meadow in Soest, in the Netherlands, with coordinates 52.172 degrees and 5.305 degrees for latitude and longitude. In figure 3.12, the test location is illustrated by a marked map of the location and a picture.

Figure 3.12: The location in Soest for the first field test
A - Local Map with roads, apartment building and the position of the radar indicated B - Picture with apartment building

In Figure 3.12a, the triangle indicates the position and looking direction of the radar, the dark marking on top of the Figure is around a big apartment building that was clearly visible from the test location and the dashed line is a path used by cyclists and walkers. The path and the building are also seen in the picture in 3.12b. This picture was not taken at the exact radar location but 150 meters forward. This was done in order to better show the apartment building, road and landscape in one image.

In Figure 3.13, a snapshot is shown from the field test in Soest. The axes of the image contain R and V_R, as was described in section 3.2.1. In the image, brighter spots indicate strong signals and dark colours indicate that no signals are received with those values. It is seen that a vertical line is present in the image, indicating the line with V_R equal to zero. This is a often-seen consequence of Fourier analyses, where the zero-frequency component is offset with respect to the other frequencies. It can be seen that the strongest reflections are relatively close to $R = 0$. Several bright spots are observed around $R = 950m$ and $R = 1700m$.

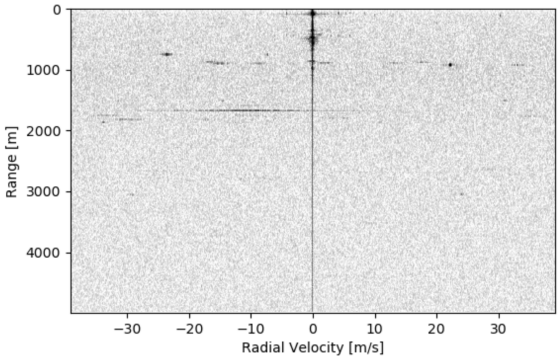

Figure 3.13: A snapshot from the results of the first field test (a darker pixel equals stronger reflection)

3.3.5. Removal of Spurious Signals

As seen in figure 3.13, many illuminating spots can be seen in the radar image. However, this image was taking in stationary position with no moving objects nearby - no walkers or cyclists were present on the road. This raises questions about the reflections that are observed, particularly since they indicate movement with tens of meters per second. Moreover, the apartment building and the trees on the horizon were located around $450m$ from the radar and they blocked all objects behind them from view. The skies were partly overcast by clouds and no aircraft were observed - at least not by the eye. So it is remarkable that bright reflections are seen at $1000m$ and further. The spots do not move, even though the range should change if $V_R \neq 0$, and the spots remain present if the radar is relocated.

These reflections are known as spurious signals, or spurs for short. They are consequences of imperfections in the radar hardware, such as interference between transmitter and receiver antennas[29]. Multiple strategies exist to cope with the existence of spurs, and different radar applications may require different solutions.

Since the radar is being tested in a stationary position in a static environment, it can be concluded that all signals that are being observed now must be spurs. The challenge is to determine the locations of the spurs in the FMCW radar image. In order to do this, a series of frames are taken from the recorded data, and the Shi-Tomasi corner detector (section 3.3.3) is applied to find the locations of the corners. Because the corners tend to wiggle slightly, the corner locations are dilated, such that the adjacent pixels are also counted as spurs. From a series of binary corner images, it is computed how often a pixel is detected as a corner. Pixel counts that surpass a threshold are considered spurs. The results of different thresholds are seen in figure 3.14.

The use of the spurs image is that now the locations of the spurs in the radar output are known. If the Shi-Tomasi corner detection algorithm finds corners that lie within the spurs on the map, these corners are disregarded for further investigation.

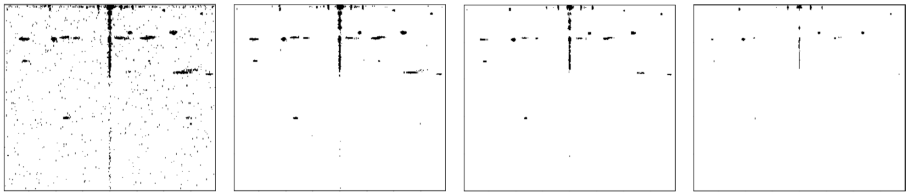

Figure 3.14: Spurs locations for different thresholds of minimum corner presence
A - > 2% B - > 5% C - > 10% D - > 25%

3.4. Direction of Arrival

In section 3.3 it was explained how the radar system can detect objects of interest in the radar image. This strategy can provide a user with Range and Doppler information about airborne objects, but this information is not sufficient to tell the user where a hazard is coming from. Additional steps are therefore required to improve the situation awareness of the radar user. The goal of this is to determine the Direction of Arrival (DoA) of an incoming radar signal. If this is possible, the information can be combined with the Range information to pinpoint the location of the object.

In this section, the technique for DoA estimation is explained. In section 3.4.1 different strategies to perform DoA estimation are introduced, and it is explained which one is chosen in this project. The next section, 3.4.2, contains the algorithm that is used to perform DoA in three dimensions. Calibration of the experimental setup is required in order to achieve accurate results, this is explained in section 3.4.3. The last section, 3.4.4, contains the results of the DoA estimation of the first field test, which was introduced in section 3.3.4.

3.4.1. DoA by Phase Difference

Several different techniques exist for determining location information for radar. Airport Surveillance Radars, used by Air Traffic Control, only provide 2D information. For airports, this is solved by using a Secondary Surveillance Radar [30], which interrogates the transponder on board of the aircraft for altitude information. This solution is not suitable for this GA application, as an SSR is unsuitable for taking on board of an aircraft and not all objects can be expected to be equipped with the proper transponders.

Another solution to determine an object's location is to perform triangulation with multiple sensors that measure distance independently. For this strategy, the distance between the sensors and the accuracy of the range measurements determine the quality of the results. For GA aircraft, multiple sensors could be at most about 10 meters apart from each other, but for the hardware, the range resolution is not expected to become smaller than $5m$, so this would leave a very poor directional estimate.

Directional antennas can also help in localizing an object. The principle of those is that a directional antenna broadcasts a signal in a single direction, so any return

signals that are observed must originate from that direction. Examples of these are the Primary Radar itself, or Height Finding Radars [31] which are directional because a parabolic reflector is built around the antenna. Phased arrays [10, 32] can also be a solution for transmitting a directional signal, by having multiple transmitters next to each other in parallel. The problem with directional antennas is that only one direction can be observed in a single moment. In order to observe the entire space around the aircraft, a scanning pattern is needed, in which the size of the beam, the total coverage and the scanning speed must be balanced to each other.

The chosen solution is to compute the DoA by the hand of the phase difference of multiple adjacent antennas, as illustrated in figure 3.15. This strategy is similar to receiver beam forming, but the direction is computed when the signals are received, and not predetermined when they are transmitted. A disadvantage of this is that each received antenna needs to be recorded separately, instead of a simple addition of all incoming signals as is seen in a phased array. The positive side is that the hardware can receive incoming signals from many directions, and therefore large parts of the close environment can be observed.

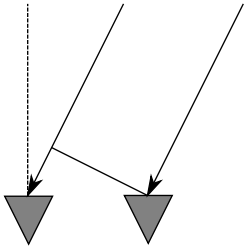

Figure 3.15: Phased array principle: a signal arrives with an angle and is received later by the left antenna

3.4.2. Three-dimensional algorithm

In this section the algorithm is presented to determine an object's location in three dimensions, when the signals are received by multiple receivers R_x. In figure 3.16 the geometry of the situation is illustrated. The location of the point P is denoted as the vector $\vec{P}$, as to avoid confusion with the receivers R_x.

When the distance of $\vec{R_{12}}$ is small with respect to $\vec{P}$, angle α is identical in subfigures 3.16a and 3.16b, so the triangles indicated in these figures must be similar, meaning that the following relation holds:

$$\frac{|\vec{P}'|}{|\vec{P}|} = \frac{d|\vec{P}|}{|\vec{R_{12}}|} \tag{3.6}$$

The phase difference ψ_{12} between the antennas R_1 and R_2 is directly dependent on the distance difference $d|\vec{P}|$ and the wavelength λ of the carrier frequency. Equation 3.6 is rewritten and afterwards rearranged:

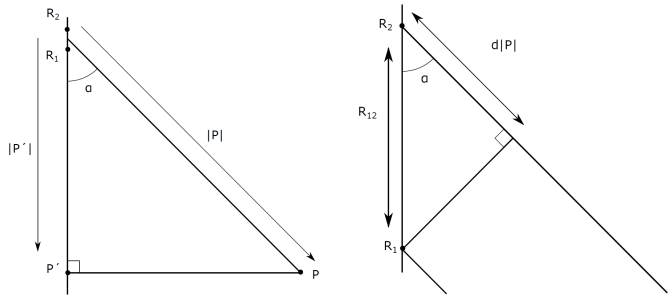

Figure 3.16: Definitions of incoming signals on two antennas R_1 and R_2

$$\frac{|\vec{P}'|}{|\vec{P}|} = \frac{\psi_{12}\lambda}{2\pi} \cdot \frac{1}{|\vec{R_{12}}|} \tag{3.7}$$

This leaves the rather obscure term $|\vec{P}'|$ in the equation: this is the distance to the point P'. That point is found when P is projected on the line $\vec{R_{12}}$. This needs to be removed from the equation, and therefore $|\vec{P}'|$ is written as the product of the vector $\vec{P}$ and the unit vector in the direction from R_1 to R_2.

$$|\vec{P}'| = \frac{\vec{P} \cdot \vec{R}_{12}}{|\vec{R}_{12}|} \tag{3.8}$$

Inserting equation 3.8 in equation 3.7 yields to the relation between the phase difference ψ_{12}, the antenna distance R_{12} and the source position P:

$$\frac{\vec{R}_{12}}{|\vec{R}_{12}|} \cdot \vec{P} = \frac{\psi_{12} \cdot \lambda}{2\pi} \frac{|\vec{P}|}{|\vec{R_{12}}|} \tag{3.9}$$

From this equation, the term $|\vec{R}_{12}|$ falls away on both sides. This equation can be applied to any combination of two receiving antennas, R_x, as long as the phase difference between the two is measured and their positions are known:

$$\begin{aligned} \vec{R_A} \cdot \vec{P} &= \frac{\psi_A \cdot \lambda}{2\pi}|\vec{P}| \\ \vec{R_B} \cdot \vec{P} &= \frac{\psi_B \cdot \lambda}{2\pi}|\vec{P}| \\ \vec{R_C} \cdot \vec{P} &= \frac{\psi_C \cdot \lambda}{2\pi}|\vec{P}| \\ &\dots \end{aligned} \tag{3.10}$$

These equations can be found for all combinations of R_x that receive the signal, and put into matrix form:

$$\frac{2\pi}{\lambda}\begin{bmatrix}\vec{R_A}\\ \vec{R_B}\\ \vec{R_C}\\ \dots\end{bmatrix}\cdot\vec{P} = |\vec{P}|\begin{bmatrix}\psi_A\\ \psi_B\\ \psi_C\\ \dots\end{bmatrix} \tag{3.11}$$

When equation 3.11 is constructed, all known parameters are sorted on the left side, since the carrier frequency λ is constant and the vectors $\vec{R}$ depend on the antenna geometry. On the right hand side, all measured parameters are placed. This includes $|\vec{P}|$, since this is the range to the object, which is measured directly by the FMCW frequency delay (explained in section 3.2). This means that the equation is now written in the form $a \cdot \vec{x} = \vec{y}$, meaning that the equation can now be solved as a linear least squares problem, and $\vec{P}$ can be computed. This is the location of the source P of the reflection of the radar signal.

However, the linear least squares can only give a location $\vec{P}$ that lies in the span of the vector space of R. That means that if the antenna locations are spread in three dimensions, then the location of $\vec{P}$ can also be found in R^3 (assuming that $\vec{P}$ is in view of the antennas). If all antennas are placed in a horizontal line, the location of $\vec{P}$ can only be determined in horizontal direction. And if all antennas are placed in a plane, then only the projection of $\vec{P}$ on that plane can be found.

For the FMCW radar that is used in this research, a constellation of four antennas is used that are located in a plane. This means that an extra step is required to determine an object's location in R^3. Luckily, this is possible. Since the total distance to the object is known and two coordinates span the plane dimensions, the Pythagorean theorem can be used to determine the perpendicular distance. This extra step is illustrated in figure 3.17.

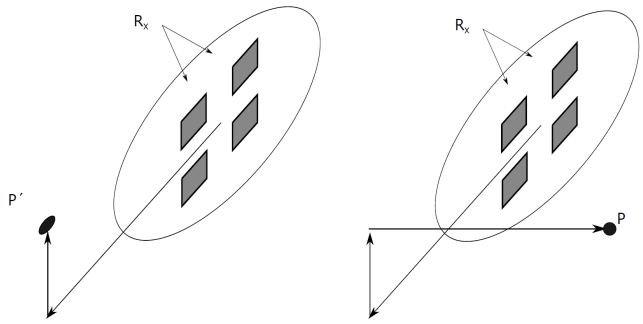

Figure 3.17: Results of 3d DoA with a radar with 4 coplanar receiving antennas

3.4.3. Antenna Calibration For Imperfect Phased Array

The strategy described in section 3.4.2 works very well if the assumptions from figure 3.15 can hold perfectly. However, in reality measurements are often distorted by imperfections in the equipment. This also applies for the radar equipment, which needs to be calibrated before DoA estimation can be performed accurately. The

reason for this can be fabrication differences of sensor hardware or the antennas, or minor differences in the lengths of the antenna cables to the analog-to-digital converter. This means that in practice, noise terms n should be removed from the measured phases ψ_x in equation 3.11:

$$\frac{2\pi}{\lambda}\begin{bmatrix}\vec{R_A}\\ \vec{R_B}\\ \vec{R_C}\\ \dots\end{bmatrix}\cdot\vec{P} = |\vec{P}|\begin{bmatrix}\psi_A - n_A\\ \psi_B - n_B\\ \psi_C - n_C\\ \dots\end{bmatrix} \tag{3.12}$$

Note that in equation 3.12 the terms n may be positive or negative and are unknown by the design. In order to be able to use the equation, the terms n must be found by calibration of the hardware.

Several methods have been developed to find the antenna noise, which not only consists of a phase delay but also of an amplitude error [32–34]. These algorithms perform calibration to a point or object, of which the position is known. For the first field test described in section 3.3.4, this can be done.

3.4.4. Results for First Field Test

In this section, the results of DoA estimation after calibration of the radar are presented. For the first field test from section 3.3.4, A measurement on the satellite map indicated that the distance to the apartment building from figure 3.12b was about 438 meters away from the measurement location. Indeed, a strong reflection was seen by the radar in the Fourier bin $430m - 450m$, with velocity $0m/s$ - as can be seen in figure 3.13. The raw phase of the measured signals is plotted in figure 3.18, where it can be observed that the measured phase is relatively constant over a period of 20 measurements.

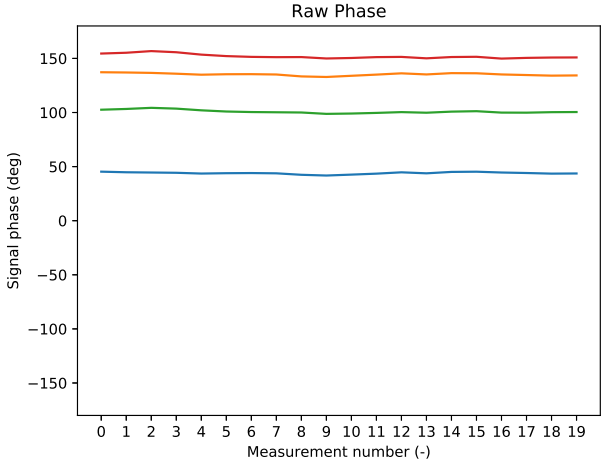

Figure 3.18: Raw signal phase of target reflection

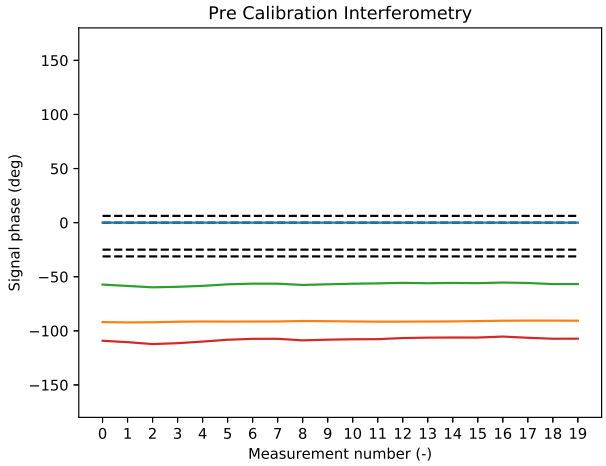

Figure 3.19: Antenna Phase Results of target reflection before calibration

Since the phase of the raw signal is constant, the phase difference between the antennas is also constant, as seen in 3.19. In this figure, the phase difference is shown for Antenna 1, compared to all other antennas. Antenna 1 is the blue line, therefore the blue line is always at 0. The phase difference that is theoretically expected by the measurements is also indicated in the figure: these are the black dashed lines. Since the position of the apartment building at the field test was not directly in front of the radar (but 5 degrees to the right of and 1 degree below the radar central axis), the expected phase differences are not zero. The expected phase difference is computed with the geometry from figure 3.16, since the direction of P is known.

The algorithm from [33] is used to compute the phase difference that is required to align all coloured lines in figure 3.19 with the black dashed lines for the expectations. In other words, the algorithm computes the terms n_x from equation 3.12. When the noise terms n_x are known, they are removed from the raw signals and the image for the phase difference is made again, as found in figure 3.20. In this figure it is seen that the phase differences are now close to the expected black dashed lines. In fact, the average offset of a phase difference and its theoretically expected value is now $0.9degrees$.

Now that the calibration is done, it is possible to determine the location of the apartment building in 3D with the formula from equation 3.12. When taking into account the attitude of the radar setup, the reflection is found to be $372m$ to the north, and $239m$ to the west. Also, the reflection is coming from $16m$ above the measurement station. This can be explained since the apartment building is 7 stories high. When put on the map from image 3.12a, the location of the building is indicated with a dot. The result can be seen in figure 3.21.

The location of the reflection is determined for all time instances in the first field test, and the results are always similar to figure 3.21, with the location of the

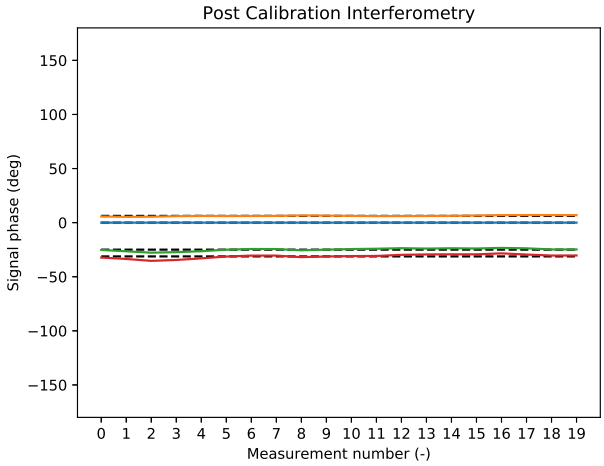

Figure 3.20: Antenna Phase Results of target reflection after calibration

reflection determined on spot of the apartment building. It was already expected that the location of the reflection would be found at the front of the building, since the 3D results were calibrated to the location of the building. It can be concluded that the calibration algorithm works correctly and that the results are consistent.

3.5. Experiment

In this section, the flight experiment is described which is done in order to assess the performance of the radar hardware. The type of the aircraft, flight information and dependent variables are discussed in sections 3.5.1 to 3.5.3.

3.5.1. Aircraft Type

The aircraft used in the flight experiment is of the type Pipistrel Virus 912. These aircraft belong to the category ultralight, with a fuselage that is as small as possible, suitable for only two pilots. An image of the aircraft can be seen in figure 3.22. The aircraft is about $6m$ long with a wingspan of $12m$. Since the aircraft is small, the surface for radar reflections is also small and aircraft of this type are expected to be amongst the most difficult GA aircraft to detect with the radar.

The aircraft is equipped with two external freight boxes that were carried under the wings. These happened to be present for other purposes other than this experiment, but they do have an influence on the test results since they will increase the radar cross-section of the aircraft, causing it to reflect more signals and therefore to be easier to be seen. The effects of the boxes have not been quantified in this study.

The aircraft is also equipped with a GPS tracker. In this way, the position of the aircraft is known at all times, and the results of the DoA estimation can therefore be

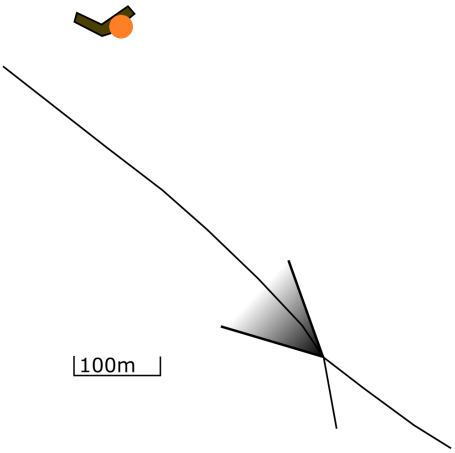

Figure 3.21: Location of the scatter after calibration and DoA estimation, indicated on the map from Soest

compared to the actual location of the aircraft. This is done after the experiment, when the DoA results have been computed.

3.5.2. Flight Information

The experiment is performed at the area of Deelen Air Base in the Netherlands, of which the airspace was closed off for traffic other than the experiment aircraft. Any airborne reflections must have come from the test aircraft or from birds that happened to be in the air. No birds were observed with the eye during the experiment.

The aircraft took off from the runway and flew one complete circuit over the field before finishing the route to go for landing. The radar was located at a small hill -large enough to arise above the tall grass, stationary aimed towards the sky above the runway. During the flight, the aircraft was always between about $500m$ and $3000m$ distance from the radar. The ground track of the flight can be seen in figure 3.23.

3.5.3. Dependent Variables

As dependent variables for the experiment, the differences between the recorded and observed positions of the aircraft are used. First, the range and radial velocity are computed at the hand of the GPS results and compared to the measured values. Secondly, the location of the aircraft is expressed in Cartesian coordinates in the radar centred axis system. The absolute difference of the found and tracked locations is computed. In order to evaluate the performance of the DoA algorithm, the offset will also be expressed in azimuth and elevation as seen from the radar. The last step to be taken is to apply a simple low-pass filter on the Cartesian results, in order to tackle the presence of high-frequency noise of the localization results.

Figure 3.22: The aircraft used for detection, with the cargo boxes under the wings

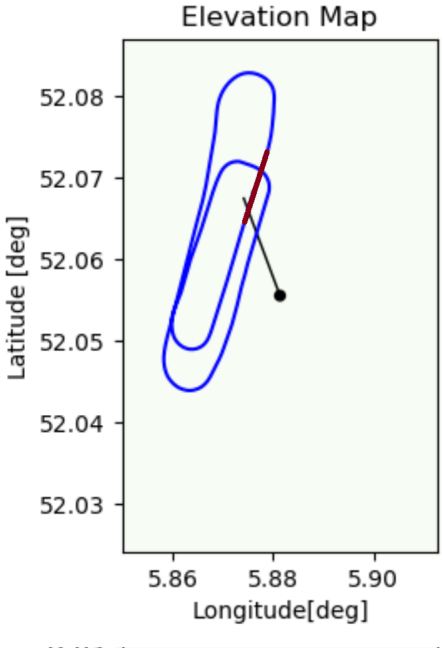

Figure 3.23: Ground track of the flight in Deelen. The radar location and looking direction are indicated in black, the red line shows the location of the runway. The flight was in counterclockwise direction.

3.6. Results

In this section, the results of the experiment are presented and described. The results are discussed briefly in this section; a more elaborate discussion can be found in section 3.7. First of all, the resulting radar output is shown. In figure 3.24, three snapshots are shown of the radar images during the flyover of the aircraft. It can be seen that the images are very similar, but a moving cluster of pixels is observed. This is the reflection of the aircraft, passing over the airfield.

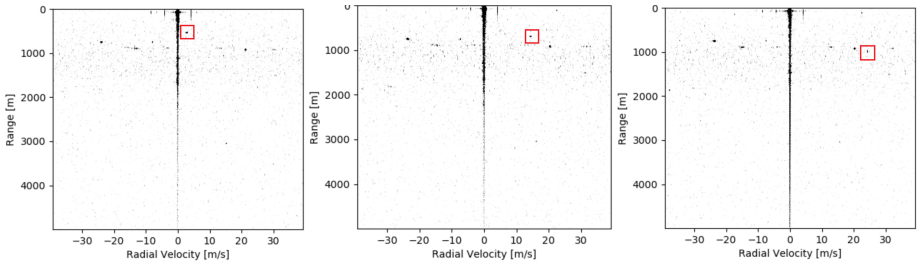

Figure 3.24: Three screenshots of the radar output during the flight over the radar. The aircraft reflection is indicated with a red square.

The pixel detection algorithm (including the spurs filter) is applied to the radar images, and resulting coordinates of the tracked pixel are plotted. Two plots are made, for the Range and Radial Velocity, which contain the measurements from both the radar and the GPS. The GPS does not yield the results for V_R directly, but they can be simply computed since the position of the radar is known, since this means that the distance vector from radar to aircraft is known. The results of these are seen in figure 3.25.

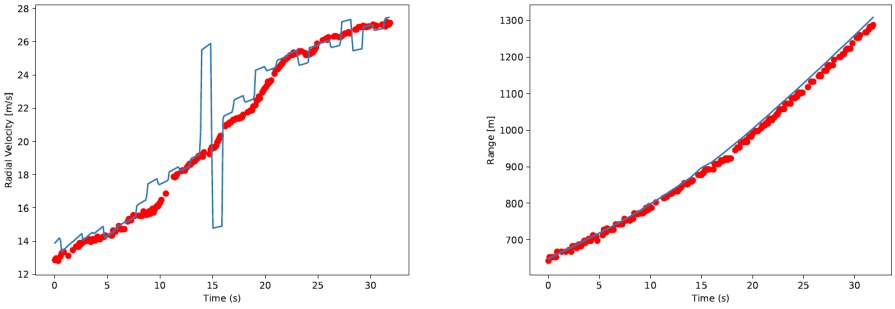

Figure 3.25: Results for V_R and R during the flyover in the experiment for radar (red dots) and GPS (blue line) measurements

In figure 3.25, it is seen that the results for the radar resemble the results from the GPS, where the radial velocity and range start small in the experiment and gradually rise to higher values. The shape of the curve is also similar, but it should be noted that the results of the GPS vary a lot when determining the radial velocity. Also pay attention that not for every measurement a red dot is plotted: sometimes

the pixel detection algorithm found that the radar feedback was not strong enough to pass the detection threshold. In the 300 measurements in 32 seconds during the flyover, an aircraft scatter was detected 202 times.

The DoA algorithm is applied to the detected pixels, and the result of that is plotted in figure 3.26. The orange scatter points are the locations of the 3D detection, and the black line is the track of the aircraft, as logged by the GPS. The green dot is the location of the radar, which is plotted on the point $(0, 0, 0)$. The x-axis points horizontally in the looking direction of the radar. Both subfigures in figure 3.26 contain the same data, only plotted from a different angle.

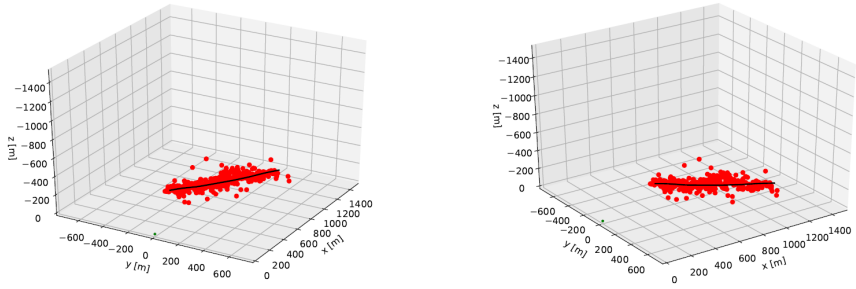

Figure 3.26: 3D results for radar DoA estimation and GPS track, as seen from two different angles

As can be seen in figure 3.26, the results for the DoA form a cloud along the GPS track of the aircraft. The scatters appear to be accurate in following the aircraft, but this needs to be quantified. Therefore the distance from the DoA estimates to the aircraft position is plotted as well, of which the results are seen in figure 3.27.

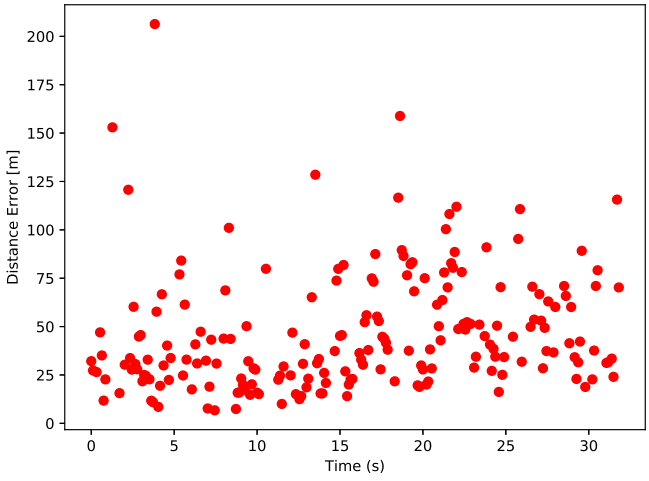

Figure 3.27: Distance from radar scatters to GPS position

Table 3.2: Mean (μ) and Standard Deviation (σ) of difference between Radar and GPS results

	Raw		Hanning	
	μ	σ	μ	σ
distance $[m]$	46.2	30.3	30.7	16.1
azimuth $[deg]$	-0.4	1.8	-0.37	0.8
elevation $[deg]$	-0.5	2.7	-0.43	1.6

From the data in figure 3.26 it is seen that the points are above and below the actual aircraft tracks. Figure 3.27 however, does not provide an indication about the direction of the distance to aircraft position, only the absolute value. In order to indicate the value of this, the distance between the scatter and GPS locations are also expressed in azimuth and elevation errors, as seen from the radar point of view. The results are given in figure 3.28.

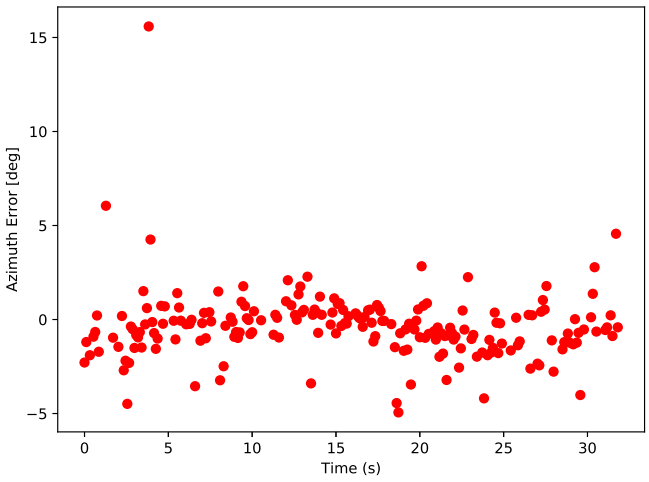

Figure 3.28: Azimuth and elevation differences between radar and GPS results

As seen from figures in 3.28, high-frequency phase noise appears to cause errors on the measurements. This means that a low-pass filter can be used to remove these outliers from the results. A simple Hanning filter [35] is therefore applied on the 3D DoA results in figure 3.26, and the results of this are given in figure 3.29.

In order to quantify the accuracy of the 3D algorithm, the mean and standard deviation are computed for the distance, azimuth and elevation errors, both for the raw data and the hamming filtered results. These values can be found in table 3.2.

3.7. Discussion

In section 3.3.1, the appearance of objects in a radar image was discussed. It was found that objects are expected to take shape as blurred pixels in the radar image.

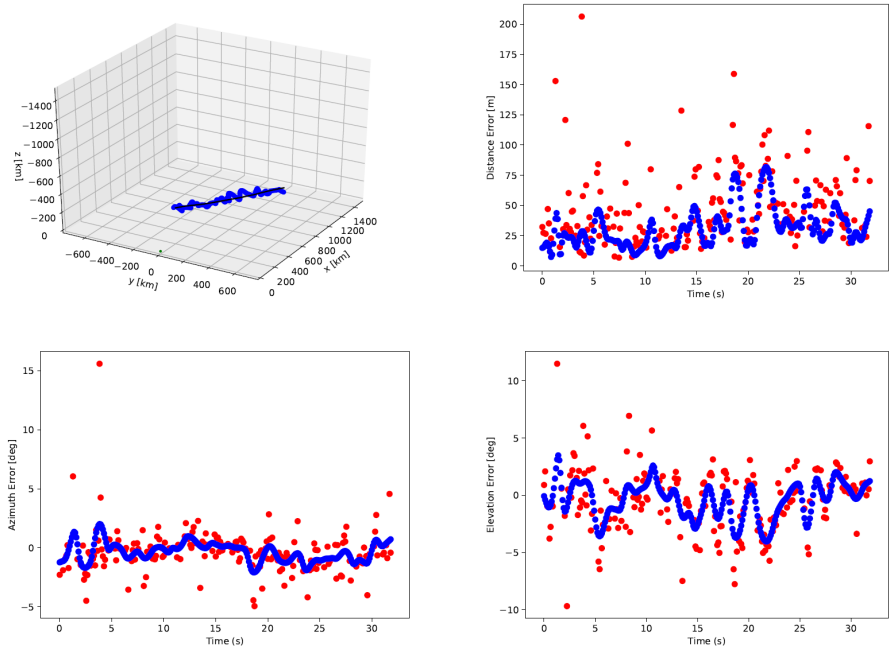

Figure 3.29: 3D results before (red) and after (blue) application of Hanning window function

When the first field test was performed, it was found that this indeed was the case, as was seen in figure 3.24. It was confirmed that the radar was possible to track the reflection of the aircraft, after spurious signals were removed from the image.

3.7.1. Radial Velocity Results

When the tracked values for the range and radial velocity are compared to those of the GPS measurements, it is seen that the trends in both figures are similar (figure3.25). However, it is seen immediately that the blue line in the radial velocity plot is varying around the red pixels. Since the variations are so abrupt (the big spike is a difference of $10m/s$ in one second: a sudden deceleration of 1g), it is reasonable to assume that the red scatter points describe the radial velocity more accurately.

For the blue line, the GPS radial velocity, it should be stated that this velocity can only be computed indirectly: GPS can pinpoint the location of an object and its velocity can be computed by subtracting consecutive measurements. For the radar, the radial velocity is computed directly, by taking the Doppler shift. The difference in V_R accuracy can also be explained because the location measurement from the GPS typically is accurate within several meters, but one pixel in the radar image is $0.075m/s$ wide. It can therefore be said that the accuracy of the radar V_R measurements is excellent with respect to that of GPS.

3.7.2. Range Results

For the range measurements, which are also presented in figure 3.25, it is also seen that the radar yields results similar to GPS. The typical position errors of several meters of GPS have little effect on the results, since the scale of the range measurements is of hundreds of meters. Also the pixel size in the radar image (one pixel is $15m$ long) is of little influence. It is seen that the radar results follow the GPS line closely, but that later in the experiment the differences between radar and GPS become larger.

Several explanations can exist for this. It is possible that the radar has an offset, that the results are biased at larger distances. It is also possible that the timing between the GPS and radar clocks was off by about one second; if the blue line would move to the right with respect of the red line the differences would also become smaller. This would have an effect predominantly in the later part where the line gradients are higher.

A third option is that the position of the ground station was measured inaccurately (by GPS) and was off by a few meters. Any location that is closer to the end of the flyover but at the same distance from the start of the experiment would yield better results to the red line.

From this experiment, it cannot yet be concluded which of these explanations causes the differences in range measurements.

3.7.3. 3D Positioning

After the first field test, if was concluded that it is possible to calibrate the radar system and to perform 3D Direction of Arrival Estimation, with which the location of an object in 3 dimensions can be determined. Now that the calibration and DoA estimation are applied to the flyover, it is found that indeed the 3D radar scatters follow the flight path of the aircraft over the test location.

3.7.4. Accuracy

It is computed that the 3D scatter points are on average $46.2m$ removed from the true GPS location, with a standard deviation of $30.3m$. The GPS results may have been a few meters off, as discussed in the section above. This would affect the μ of $46.2m$, but would have a minor effect on the standard deviation.

The average distance between GPS and radar results is an absolute distance and can therefore never become negative. More information about the accuracy of the DoA algorithms can be found when the results are expressed in azimuth and elevation angles. It is found that the standard deviations for azimuth and elevation errors are 1.8 and 2.7 degrees, respectively. The Hanning filter reduced those values to 0.8 and 1.6 degrees. This can be sufficient to provide a mobile ground station with an image of objects in the sky above. The mean errors have values of 0.4 and 0.5 degrees, which can be caused by small misalignments of the radar: the equipment to measure the radar attitude was accurate to a single degree, so smaller errors such as these can be fixed with accurate calibration of the radar platform.

The angular accuracy of the DoA algorithm can be improved by raising the number of receiving antennas. In this experiment, only 4 receiving antennas were used,

but it is possible to increase that number if a better accuracy is required. The number of equations for the linear least squares problem in section 3.4.2 increases if more antennas are added to the setup. Having more antennas can also decrease the effect when a single antenna measurement is disturbed. It is remarkable that the DoA algorithm yields more accurate results in azimuth direction than in elevation direction. The antennas formed a square 2x2 pattern, which is symmetrical in horizontal and vertical direction. The only difference can be the polarization direction of the radar signals. It is unclear whether the difference in azimuth and elevation accuracy originates from the radar system, or from the test environment.

3.7.5. Range Limit

The range limit of the radar system is unknown, since it is not tested explicitly. The largest distance that the aircraft had to the ground station was just over $3km$, at which the radar reflection was visible in the radar images, but only when they are viewed in a sequence - the signal was too weak to be differentiated from background noise when just a single image was observed. Novel visual tracking algorithms are able to detect such reflections when the data is treated as a streamed video, so it can be possible to detect even these reflections. A larger number of antennas in the configuration can also help to increase the sensitivity, and increase range for the radar. The maximum attainable range is furthermore dependent on the radar cross-section of the object. Larger aircraft will be visible from larger distances.

3.7.6. Comparison to other products

It is important to compare the performance of the FMCW radar to that of Flarm devices and airport surveillance radars. The FMCW radar is portable and can be powered by a small battery, and can therefore be deployed at any location. The radar has a field of view of 80 degrees, in vertical and horizontal directions. In order to cover the entire sky, a constellation of multiple systems is required. An alternative is to have the radar pivot around an axis, similar to a primary radar. When objects are observed around the aircraft, the radar can pinpoint the direction of the signal source within a few degrees accuracy. This is significantly better than e.g. Flarm, which can localize an object in 12 segments of 30 degrees in horizontal direction, and 5 vertical layers relative to the device. Multiple consecutive measurements can further improve the accuracy, as the high-frequency phase noise can be countered with a low-pass filter. The radar system can detect various objects, independent on whether they carry the proper equipment. The radar results are dependent on the radar cross-section of the objects. A Pipistrel Virus 912 aircraft was visible up to $3km$ distance.

The experiment confirms that the radar can be used to detect aircraft within the vicinity of the radar. Future research is needed to test whether the radar can be used while moving in the air. It is also required to test the radar in rotating mode, in order to observe the complete environment. Additional techniques to filter reflections based on their elevation can help to separate aircraft from ground reflections.

3.8. Conclusion

In this chapter research was presented towards the possibility of building a portable primary radar for General Aviation, of which the goal is to bring it on board of an aircraft for purposes of 'detect and avoid'. The system has to be affordable, small and it has to consume little power. The hardware tested in this chapter matches those requirements.

A test was performed with an aircraft flying over the radar, which could be observed in the radar image for a range up to $3km$. The aircraft was tracked with an on-board GPS for a flyover at closer distance and the radar was able to detect the aircraft autonomously and to determine its location with an accuracy of on average $46m$. The direction of the incoming signals can be determined within 2 degrees horizontally, and 3 degrees vertically. If the aircraft is tracked, low-pass filters can be applied to filter out the high-frequency phase noise and increase the accuracy of the three dimensional position estimates. Expanding the number of antennas beyond the 4 used in this research can also improve the radar results further.

It has been demonstrated that the detection of other aircraft is possible by this radar system, which will increase the situation awareness of the pilot and help prevent hazardous situations. In chapters 5 and 6 of this dissertation, the radar will be used on board of an aircraft for purposes of determining the flight state and position of the own aircraft.

References

[1] D. Wilson and T. Sloan, *VFR Flight Into IMC: Reducing the Hazard,* Journal of Aviation/Aerospace Education & Research **13**, 29 (2003).

[2] D. A. Wiegmann, J. Goh, and D. O'Hare, *The role of situation assessment and flight experience in pilots' decisions to continue visual flight rules flight into adverse weather.* Human Factors **44**, 189 (2002).

[3] P. Pegin and E. Sitnichuk, *The Effect of Sun Glare: Concept, Characteristics, Classification,* in *Organization and Traffic Safety Management in large cities*, Vol. 20 (Elsevier B.V., 2016) pp. 474–479.

[4] J. M. Hoekstra, R. N. H. W. V. Gent, and R. C. J. Ruigrok, *Designing for safety : the 'free flight' air traffic management concept,* Elsevier Reliability Engineering & System Safety **75**, 215 (2002).

[5] SESAR Joint Undertaking, *U-space blueprint*, Tech. Rep. (SESAR Joint Undertaking, Luxembourg, 2017).

[6] F. A. A. Organisation, *Unmanned Aircraft System Traffic Management*, Tech. Rep. (Federal Aviation Administration, 2020).

[7] C. Munoz, A. Narkawicz, and J. Chamberlain, *A TCAS-II Resolution Advisory Detection Algorithm,* in *AIAA Guidance, Navigation and Control Conference* (2013) pp. –.

[8] F. Technology, *System Design and Compatibility*, Tech. Rep. 1 (FLARM technology GmbH, 2015).

[9] F. Folster, H. Rohling, and U. Lubbert, *An automotive radar network based on 77 GHz FMCW sensors,* IEEE National Radar Conference - Proceedings **2005-Janua**, 871 (2005).

[10] M. S. Lee and Y. H. Kim, *Design and performance of a 24-GHz switch-antenna array FMCW radar system for automotive applications,* IEEE Transactions on Vehicular Technology **59**, 2290 (2010).

[11] R. O. Chavez-Garcia and O. Aycard, *Multiple Sensor Fusion and Classification for Moving Object Detection and Tracking,* IEEE Transactions on Intelligent Transportation Systems **17**, 525 (2015).

[12] B. Fürsich, R. Bamler, S. Augustin, H.-w. Hübers, and X. X. Zhu, *Towards single-pixel FMCW radar reconstruction,* in *4th International Workshop on Compressed Sensing on Radar, Sonar and Remote Sensing* (2016) pp. 96–100.

[13] A. G. Stove, *Linear FMCW radar techniques,* in *IEE Proceedings F Radar and Signal Processing*, Vol. 139-5 (1992) pp. 343–350.

[14] A. Meta, *Signal Processing of FMCW Synthetic Aperture Radar Data* (TU Delft, 2006) p. 133.

[15] S. J. Orfanidis, *IEEE Transactions on Communications*, Vol. 20-5 (Pearson Education Inc, 2004) pp. 1046–1047.

[16] P. Stoica and R. Moses, *SPECTRAL ANALYSIS OF SIGNALS* (Prentice Hall, Upper Saddle River, 2004).

[17] J. Maas, R. V. Gent, and J. Hoekstra, *Object Tracking in Images of an Airborne Wide Angle FMCW Radar,* in *ICRAT International Conference for Research in Air Transportation* (2018) p. 8.

[18] R. L. Ford, *On the Use of Height Rules in Off-Route Airspace,* Journal of Navigation **36**, 269 (1982).

[19] J. M. Hoekstra, J. Maas, M. Tra, and S. E., *How Do Layered Airspace Design Parameters Affect Airspace Capacity and Safety ?* in *7th International Conference on Research in Air Transportation* (2016) p. 8.

[20] Z. Liu, L. Wang, G. Hua, Q. Zhang, Z. Niu, Y. Wu, and N. Zheng, *Joint Video Object Discovery and Segmentation by Coupled Dynamic Markov Networks,* IEEE Transactions on Image Processing **27**, 5840 (2018).

[21] M. Narayana, A. Hanson, and E. Learned-Miller, *Coherent motion segmentation in moving camera videos using optical flow orientations,* in *IEEE International Conference on Computer Vision* (2013) pp. 1577–1584.

[22] M. Haghighat and M. Abdel-Mottaleb, *Lower Resolution Face Recognition in Surveillance Systems Using Discriminant Correlation Analysis,* in *12th IEEE International Conference on Automatic Face and Gesture Recognition* (2017) pp. 912–917.

[23] C. Harris and M. Stephens, *A Combined Corner and Edge Detector,* in *Proceedings of the Alvey Vision Conference* (1988) pp. 147–152.

[24] K. G. Derpanis, *The Harris Corner Detector,* York University **-**, 2 (2004).

[25] M. Trajković and M. Hedley, *Fast corner detection,* Image and Vision Computing **16**, 75 (1998).

[26] J. Chen, L. hui Zou, J. Zhang, and L. hua Dou, *The comparison and application of corner detection algorithms,* Journal of Multimedia **4**, 435 (2009).

[27] J. Shi and C. Tomasi, *Good Features to Track,* in *IEEE Conference on Computer Vision and Pattern Recognition* (1994) pp. 593–600.

[28] C. S. Kenney, M. Zuliani, and B. S. Manjunath, *An axiomatic approach to corner detection,* in *IEEE Computer Society Conference on Computer Vision and Pattern Recognition*, Vol. I (2005) pp. 191–197.

[29] A. W. Doerry and D. L. Bickel, *Apodization of Spurs in Radar Receivers Using Multi-Channel Processing*, Tech. Rep. (Sandia National Laboratories, Albuquerque, 2014).

[30] R. M. Trim, *Mode S : an introduction and overview,* Electronics & Communication Engineering **2**, 53 (1990).

[31] P. Barton, *Height Finding Radar,* (1979).

[32] S. Hu, G. Hong, and W. Jian, *Antenna calibration and digital beam forming technique of the digital array radar,* in *IEEE International Conference on Signal Processing, Communications and Computing* (2013) pp. –.

[33] W. Li, J. Lin, W. Wang, Y. Wang, and Z. Chen, *Method of multi-channel calibration for digital array radar,* in *European Radar Conference* (2015) pp. 533–536.

[34] A. J. Weiss and B. Friedlander, *Eigenstructure methods for direction finding with sensor gain and phase uncertainties,* Circuits, Systems, and Signal Processing **9**, 271 (1990).

[35] P. Podder, Z. T. Khan, M. H. Khan, and M. M. Rahman, *Comparative Performance Analysis of Hamming , Hanning and Blackman Window,* International Journal of Computer Applications **96**, 1 (2014).

4

Object Tracking in Images of an Airborne Radar

J Maas, R Van Gent, J Hoekstra

In chapter 3 it is demonstrated that the radar prototype can detect targets in its vicinity, which can be used to alert a pilot of hazards. The tracking of targets connects different observations through time. This information can be used in order to filter out high-frequency noise with which the accuracy of position estimates can be improved (as recommended in chapter 3). Secondly, tracking of objects makes extraction of lateral velocity information possible: Doppler information can only be used to determine radial velocity information. This information is necessary to assess the risk that a target poses, such that optimal advice can be given to a pilot.

In this chapter a tracking method is proposed, which is optimized for use on targets in FMCW radar images. The method is suitable for use in flight, and it is evaluated using simulated radar responses of real performed flights. It is found that the proposed tracking method performed better than the traditional method for the application of having a flying FMCW radar with a wide aperture.

This chapter is published as *Object Tracking in Images of an Airborne Wide Angle FMCW Radar*, ICRAT International Conference for Research in Air Transportation, 2018

4.1. Introduction

Object tracking is an important step in any surveillance application [1]. In diverse fields, from weather stations to traffic cameras, linking different observations to one another through time is a crucial step in order to study and predict the medium term behaviour of observations. Improved methods of tracking can increase the quality of the observations over time, and will improve the situation awareness of the observer with respect to the surroundings.

Much work has been done in the field of visual object tracking. Numerous studies have been performed that found high quality algorithms for handling temporary occlusions, singularities and even faulty observations [2–4]. Many of these studies are applied on visual systems such as webcams, helicopter imagery or handycams. Tracking algorithms which are tailor made for airborne FMCW applications, however, are scarce.

In this chapter, an algorithm is presented which can bridge the gap between the field of visual tracking algorithms and the Frequency Modulated Continuous Wave (FMCW) radar in this thesis. In section 4.2, the application of the FMCW radar is explained, after which the theory of the algorithm improvements is explained in section 4.3. The parameters that are used to assess the quality of the algorithms are discussed in section 4.4, after which the experiment is described in section 4.5. The results are presented in section 4.6, followed by discussion (4.7) and conclusions (4.8).

4.2. Application

In General Aviation (GA), many flights are performed under Visual Flight Rules (VFR), in which pilots rely on their own eyes to perform navigation and surveillance. Since a pilot's field of view is finite, possible threats may be overlooked, causing hazardous situations.

Technical applications that assist the pilot in his/her VFR tasks exist. An example of this is FLARM technology [5], in which aircraft broadcast their positions to each other using transponders. These kinds of systems are a form of dependent surveillance, and they can only work if both aircraft are equipped with the right technology. Therefore, such an application can never guarantee that no dangers are present.

A different, novel approach is to have a radar system on board, which can broadcast its own signal and use it to actively and independently scan its environment. This signal is reflected back on objects and can be observed by the system [6]. Similar to the way in which bats sense their environment, such a system empowers independent surveillance with which non-cooperative objects such as birds, towers and mountains can be observed [7].

Developments in radar technology have improved the availability, weight and pricing of FMCW radar systems, to an extent that they can be considered feasible for these tasks. If such systems are to be implemented for improving situation awareness, robust and accurate algorithms are required to perform tracking of observations, which is what this chapter is about.

4.3. Algorithm

In this section, a new object tracking algorithm is proposed. It starts with a section on conventional object tracking, after which the FMCW radar principles are introduced. The majority of this section is found in the last part, in which the differences between visual and radar images are discussed and in which the tailor-made tracking algorithm is presented.

4.3.1. Visual Object Tracking

As discussed in section 4.1, many publications exist in which visual tracking algorithms are discussed [2]. These are used in all kinds of applications, ranging from mobile phones to satellites. Since radar images are constructed as two dimensional monochrome arrays, visual tracking methods may be suitable for this application as well, so they are used as a starting point in this study.

The challenge of object tracking is to link observations to each other, which are supposedly done in (short) succession to each other. A model of the object properties is used to quantify expectations about the behaviour, that are used to perform accurate assignment between observations and models [1]. The common elements of object tracking are illustrated by the image in figure 4.1.

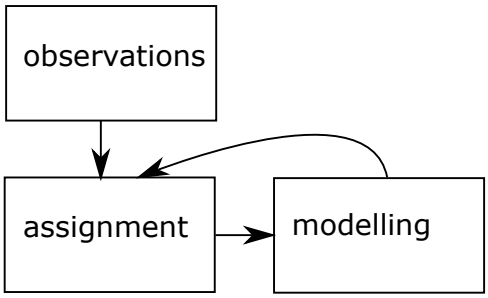

Figure 4.1: Generic elements of tracking software

Elements of Tracking

The three elements of figure 4.1 form a tracking system together. Firstly, the objects that should be tracked must be observed by a sensor. Generally, this is a camera system but in this project, the sensor is an FMCW radar.

The second block is the assignment of observations to the internal models of the objects, usually named 'tracks'. Assignment theory is a research field on its own, but one of the most frequently used algorithms is the Hungarian Algorithm, a well-known optimization algorithm that can solve assignment problems [8]. This algorithm will also be used in this study. Many object tracking research focuses on this aspect of object tracking [3, 4, 9–11].

The third block, the modelling of the tracks, is the focus of this chapter. An observation is usually described as a state vector, containing all important information. Amongst the information is, at least, the location of the observation in the

image. The colour of the object, its shape and its structure can be possible extra information in the state.

Object Modelling

The progression of the state parameters of an inertial object can be computed by using a Kalman Filter [2, 6, 9, 10, 12, 13]. Kalman Filters are common in aviation, and it can be expected that they are useful in this tracking application as well. An internal linear model of the object parameters is used to predict the next expected state vector of the track. An internal model, frequently denoted F, is usually simply defined in the following way:

$$\vec{s}_{t+1} = F \cdot \vec{s}_t = \begin{bmatrix} 1 & & dt & \\ & 1 & & dt \\ & & 1 & \\ & & & 1 \end{bmatrix} \cdot \begin{bmatrix} x \\ y \\ v_x \\ v_y \end{bmatrix} \tag{4.1}$$

In equation 4.1, the parameters x and y in state vector $\vec{s}$ are used to describe the position of the observation in the frame, and v is used for the time derivative of the position, in both directions. The time of the measurement is called t, and the time since the previous measurement is called dt. It can be seen that even though v_x and v_y may not be directly observed, they can indeed be part of the internal Kalman model.

Standard visual algorithm

Combining all the descriptions based on the literature in section 4.3.1, it is possible to describe a 'standard approach' for object tracking in visual systems. Such an algorithm typically looks like the following:

1. Load observations
2. For all existing tracks: prediction current state
3. Evaluate all combinations of observation + track
4. Assign the best matches of observations to the tracks
5. Update internal models of assignments
6. Initialize new tracks of unassigned observations
7. Close tracks without observations
8. Start again at 1.

4.3.2. FMCW Radar Imaging

A Frequency Modulated Continuous Wave (FMCW) radar system operates by broadcasting a radio wave using a transmitting antenna. The signal is reflected on the environment, and observed by a receiving antenna. The basic signal, the 'carrier wave' can be modulated by another frequency, which can be varied over time [14, 15].

Comparing the observed frequencies with the broadcast ones, information about the environment can be deduced. Phase and frequency shifts between the signals are caused by the travel times of the radio waves and by the Doppler effect. Fourier transforms can be used to infer those properties from the incoming signals, once they are converted to a digital signal.

The result of this is that the axes system of an FMCW radar image are different than those of traditional visual imagery, as indicated in figure 4.2 [16]. Where the traditional axes of a visual image contain information about the location of an object, or its elevation and azimuth with respect to the camera, this information is absent in this type of radar images.

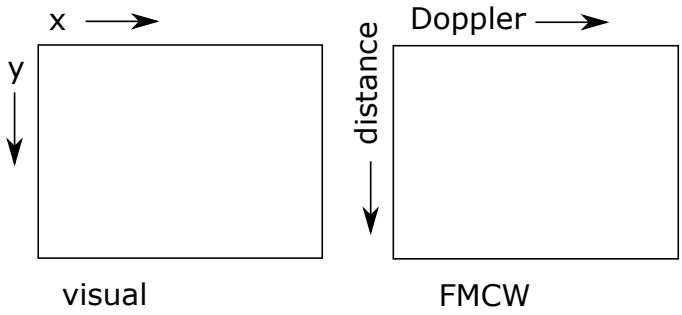

Figure 4.2: Differences in image axes

Algorithms for Direction of Arrival (DoA) estimation of incoming radar signals may be applied to such an FMCW radar system, in order to increase the knowledge about the observed objects [6, 15]. They are dependent on the quality and number of receiving antennas on the aircraft, and the stiffness of the wing[1] and presence of background noise [17]. These factors influence the performance in determining the DoA. It is therefore beneficial to be able to perform tracking directly in the radar image, so as not to be dependent on the quality of DoA estimation.

4.3.3. Algorithm Improvements

Working in the radar image frame, important differences exist that distinguish this project from a standard camera application. Three changes in standard visual tracking models are made in order to accommodate those differences. They are discussed in the paragraphs below.

[1] The distance away from the aircraft makes the wingtips a very suitable place to mount a radar system, but this has consequences for the observation quality

Aliasing

When inferring a frequency from a Fourier transform of sampled data, the maximum observable frequency, called the Nyquist frequency, is dependent on the sampling rate of the data. Frequencies that lie outside the range will be observed as their aliases: frequencies with a difference of $n \cdot f_N$ (an integer times the Nyquist frequency) [14, 18].

This is illustrated in figure 4.3, where three rotating discs are depicted, with different rotational velocities. If the sampling frequency is such that each disc rotates half a circle between each sample, the discs will be observed the same, and an observer cannot distinguish which one has which rotational velocity.

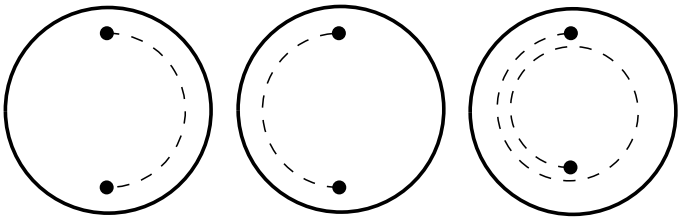

Figure 4.3: With the right sampling rate, these three discs with different rotational frequencies will be observed identically

For this project, this is applicable for the Fourier shift in Doppler direction. This means that it is impossible to estimate the Doppler frequency exactly, since a signal with a Doppler frequency outside of the observable spectrum will be seen as its alias.

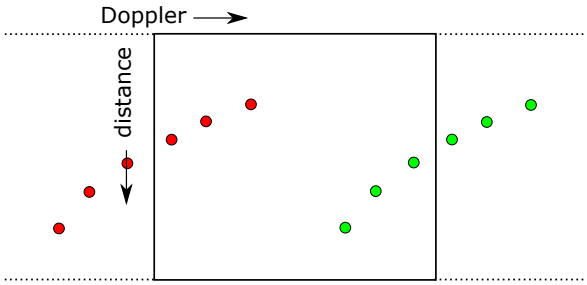

Figure 4.4: Observations of an object in the range-Doppler image over time, with aliases indicated in red

When tracking of an object is performed over multiple time instances, it is possible that the Doppler shift of the object changes such that the object moves out of the image frame, and that an alias becomes visible. This is indicated in figure 4.4, where an example track under influence of aliasing is shown.

The problem of the aliasing can be solved using a simple but precise alteration in the algorithm, to change the definition of **innovation** in Doppler direction. Innovation is a term used in signal processing, which describes the difference between the predicted state of the observation and the observed one [1, 12, 13]. Traditionally,

innovation ($\vec{y}$) is computed in the following way, using the notation $:=$ to indicate a computational assignment:

$$\vec{y} := \vec{o} - \vec{p} \tag{4.2}$$

Innovation is used in the Kalman filter, to update the track model, and in the assignment algorithm, as mentioned in section 4.3.1: the Hungarian Algorithm is fed with the l^2 norms of the innovation vectors.

Realising that aliasing may make an object appear at the other side of the image, the component of the innovation in Doppler direction is computed in the following way:

$$y_D := mod\left(\left(o_D - p_D + \frac{D_{width}}{2}\right), D_{width}\right) - \frac{D_{width}}{2} \tag{4.3}$$

In equation 4.3, $mod(a,b)$ indicates the modulo of a divided by b and D_{width} is the size of the image in Doppler direction. This definition ensures that the innovation is computed either with the direct distance, or with the distance around the outside of the image, whichever is shorter.

Relation between image axes

When looking at the standard x, y linear model shown in equation 4.1, it can be observed that x and y are independent of each other - a common element of visual systems, in which the different axes of the generated images are uncoupled. Some research includes perspectivity in the model [19], but in general, movements in x and y direction are independent.

This is not the case for an FMCW radar system. One of the two parameters measured, the Doppler shift, is caused by relative movements of the object with respect to the observer. The Doppler shift is a direct measure for the radial velocity of the object, its speed in the direction along the distance vector. This means that there is a relation between the distance R and the Doppler speed V_R:

$$V_R = \frac{dR}{dt} \tag{4.4}$$

The relation between R and V_R from equation 4.4 means that the internal linear model must be adapted, as seen in equation 4.5:

$$\begin{bmatrix} 1 & & dt & \\ & 1 & & dt \\ & & 1 & \\ & & & 1 \end{bmatrix} \begin{bmatrix} x \\ y \\ v_x \\ v_y \end{bmatrix} \rightarrow \begin{bmatrix} 1 & dt & & \\ & 1 & & dt \\ & & 1 & \\ & & & 1 \end{bmatrix} \begin{bmatrix} R \\ V_R \\ dR/dt \\ dV_R/dt \end{bmatrix} \tag{4.5}$$

Aliasing and Axes Relations Combined

When the two improvements from the previous sections are implemented, a new problem rises. If the relationship between R and V_R is used, but due to aliasing V_R can have multiple values, how to predict R?

When an observation is assigned to an existing track, the values of R between the current and most recent observations can be compared. The change in R per time unit, $\Delta R/\Delta t$ can be used to find the proper value of V_R. This means that an extra step should be taken after the assignments are computed by the Hungarian Algorithm, just before observations are appended to the internal models:

$$V_R := V_R + round\left(\frac{\Delta R/\Delta t - V_R}{D_{width}}\right) * D_{width} \tag{4.6}$$

In equation 4.6, $round()$ indicates rounding off to the nearest integer. This computation step ensures that all tracks that consists of two or more observations have found the right value of V_R to use in their internal model. When a track still consists of only one observation (it was just formed in the previous step), it is not possible yet to have an accurate estimate of V_R.

This means that this should be incorporated by the tracking algorithm. When computing the innovation, as the difference vector between expected and observed states, one extra step should be added that is only executed if the track only consists of one observation yet. In this step, the innovation component in Range direction should be recomputed:

$$y_R := mod\left(\left(y_R + \frac{D_{width}}{2}dt\right), D_{width} \cdot dt\right) - \frac{D_{width}}{2}dt \tag{4.7}$$

4.4. Quality Assesment

To assess the performance of visual tracking algorithms, two different dependent variables are used. They are discussed in the paragraphs below. Next to these parameters, it is beneficial to plot the course of the tracks in the radar image frame. This will provide an insight in the tracking results, and it allows for human verification of the achieved tracks.

4.4.1. Innovation

Innovation, as described in section 4.3.3, is the variable which describes the vector difference between the predicted and observed state vectors. The l^2-norm of the innovation describes the pixel distance between the states in the radar image, and it describes how accurate the internal linear model is: lower innovation is better. Therefore, the average value of the innovation will be used as a quality parameter in this research.

Next to that, the distribution of the innovation is also relevant. If the innovation is consistently low, this means that the gate size of the tracking algorithm can be reduced: the border distance at which an observation and a track may still be linked. A low gate size means that new tracks can be initiated when new observations occur close to existing tracks. In other words: a low gate size means that the algorithms can follow more tracks at the same time. In order to monitor this, the 95% border of the innovation distribution will be used as a quality parameter.

4.4.2. Number of Tracks

Nothing says more 'Tracking Failure' than losing track of an object. Therefore, it is important to monitor the number of lost tracks in an experiment. Any time an existing track is ended too soon, the remaining observations will form a new track together. The number of observed tracks can therefore be used to describe the amount of lost tracks, of which fewer is better.

4.5. Experiment

An experiment is conducted to assess the performance of the proposed tracking algorithm. In order to test only the 'modelling' element from figure 4.1, 'assignment' will be done by the standard practice of the Hungarian Algorithm and in order to guarantee proper 'observations', a computer will be used to simulate the radar response in different flight conditions.

The radar simulator is a high-precision wave generator, in which all important factors are incorporated: the positions and angular rates of the aircraft, terrain structure and hardware properties: from the specific antenna configuration to wave-length and position on the aircraft frame. The simulator is able to compute the effects of millimetre-scale design and compute the Doppler and range properties of all objects in the vicinity of the aircraft, with a maximum range defined at 5km, and generated radar images with a resolution of 250x250 pixels.

The difficulty here is to develop a testing environment which is both challenging and realistic. It is important to test the performance of the tracking algorithm under difficult circumstances, where many aircraft are in each others vicinity. Many simultaneous observations may lead to mixing of tracks, which should be prevented.

On the other hand: the testing environment should be realistic and not appear set up, so as not to raise questions about the independence of the test.

A solution was found to meet both criteria simultaneously. Using flightradar24.com, a website that displays live aircraft locations, a Cirrus SR22T aircraft was found which performs mostly local VFR flights. A picture of such an aircraft model is seen in figure 4.5.

Figure 4.5: Image of a Cirrus SR22T Aircraft

The flight history of this aircraft can be downloaded, and 10 flights were selected that have been performed under VFR around the same airport, Warsaw-Babice Airport in Poland (ICAO code EPBC). These flights form the basis for the experiment. Therefore, the experiment is conducted with aircraft that are accelerating, making turns, changing altitude and performing other manoeuvres which were not discussed in the model in section 4.3.3. The routes are displayed in figure 4.6.

Next to those flights, three flights have been simulated using the off-the-self computer simulator Xplane, a high-fidelity flight simulator, in the same airspace. In the radar simulations, the radar system will be simulated to be on board of these aircraft, since the simulated data has a higher quality than the ADS-B data. These three flights will form three distinct test scenarios, in which all Cirrus flights are implemented. The simulated flights are also indicated in figure 4.6.

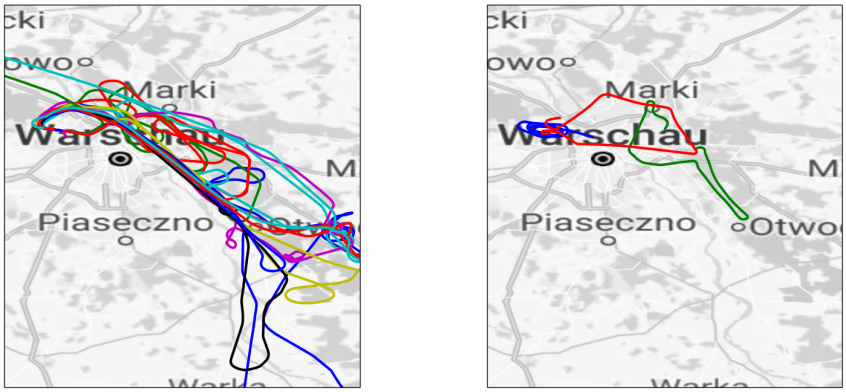

(a) Cirrus Flights (b) Simulated Observer Flights

Figure 4.6: Flights around Warsaw-Babice plotted on a map from Google, the first letter 'a' in Warschau is on the location of the airfield

The first simulated flight is called the Circuit flight, as it performs a simple circuit above the airfield (without landing). All Cirrus flights are simulated to be at the end of their route and nearing the airfield again, and they will land with intervals of only 60 seconds. This simulates a busy situation near an airfield.

The second flight (the red line in figure 4.6) revolves around point Zulu, the entrance/exit point of the airfield, located just after crossing the river Wisla. The flights will be simulated to depart one minute after each other, and they will all fly towards point Zulu. This simulation creates a dense airspace.

The last simulated flight (the green line in figure 4.6), is performed in the free airspace north-west of the river Wisla. The flight is still in alongside direction of the river, as the majority of the Cirrus traffic flies in that direction. Flying at more diverse altitudes and with the possibility of sudden turns, this is the approximation of a crowded Free airspace.

4.6. Results

The resulting tracks in the $R - V_R$ frame of the flights are seen in figures 4.7, 4.8 and 4.9, with the results of the traditional and proposed tracking algorithms. In these figures, each track is randomly assigned a colour. This means that all line segments with the same colour belong to the same track.

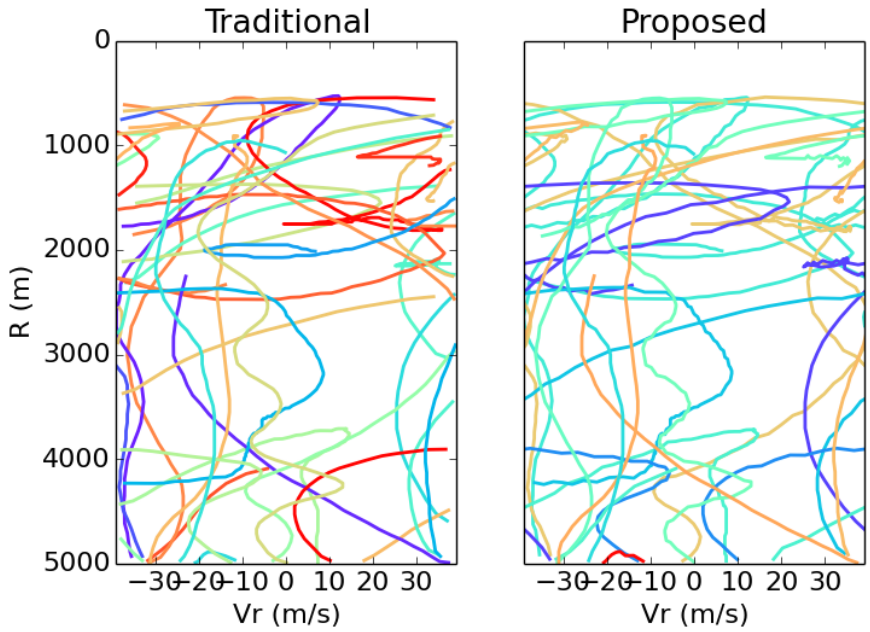

Figure 4.7: FMCW Radar image tracks of the Circuit flight

From figures 4.7, 4.8 and 4.9, two direct observations are made: the first is that the proposed algorithm connects track data together which may be seen as separate tracks by the traditional algorithm (an example of this are the tracks which are closer than 2000m in figure 4.9). The second observation can be done when looking at the side edges of the figures, at $V_R = +-40m/s$. Here it can be seen that many of the tracks end when observed with the traditional algorithm, but with the improvements they are connected to their aliases on the other side of the image.

In figures 4.10, 4.11 and 4.12, the same tracks from figures 4.7, 4.8 and 4.9 are plotted, but now in the horizontal aircraft body fixed frame of reference. These tracks are plotted assuming that perfect Direction of Arrival estimation is performed. In other aspects they are identical to the tracks in the previous figures; only the axes are changed. These images are made because they are slightly easier to interpret than the $R - V_R$ plots. In the images, the X-axis points in the direction of the nose and the Y-axis points towards the right wing tip of the aircraft.

In figure 4.13, a histogram is given of the distribution of the definitive innovations used by all tracks' Kalman filters. It can be seen that the majority of all

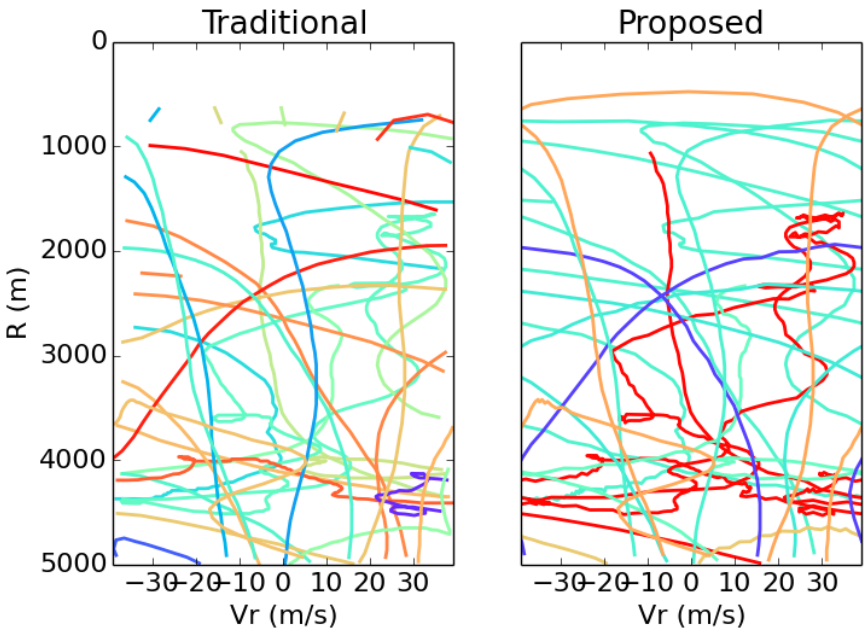

Figure 4.8: FMCW Radar image tracks of the Zulu flight

		Circuit	Zulu	Free
Average (pix)	Traditional	2.1	2.7	4.3
	Proposed	2.0	2.5	3.6
95% percentile (pix)	Traditional	7.1	10.5	14.4
	Proposed	4.9	7.1	10.7

Table 4.1: Results of the l^2 norm of the innovation in the experiments

innovations, both in the traditional and proposed algorithms, are less than 5 pixels. The histograms of the other two flights look very similar to the one in figure 4.13, and are therefore omitted. The exact data on the average innovation and 95% percentile innovation are given in table 4.1.

In table 4.2 the total number of observed tracks for the traditional and proposed tracking algorithms are shown. Next to that, a manual tracking count is also performed. This is done by simulating the radar output step by step for the complete flight, and counting the number of tracks within the looking distance. Although 10 flights were simulated, the number may be lower because some aircraft happen to never come close enough, or the number of tracks may be higher because aircraft enter the observable area multiple times.

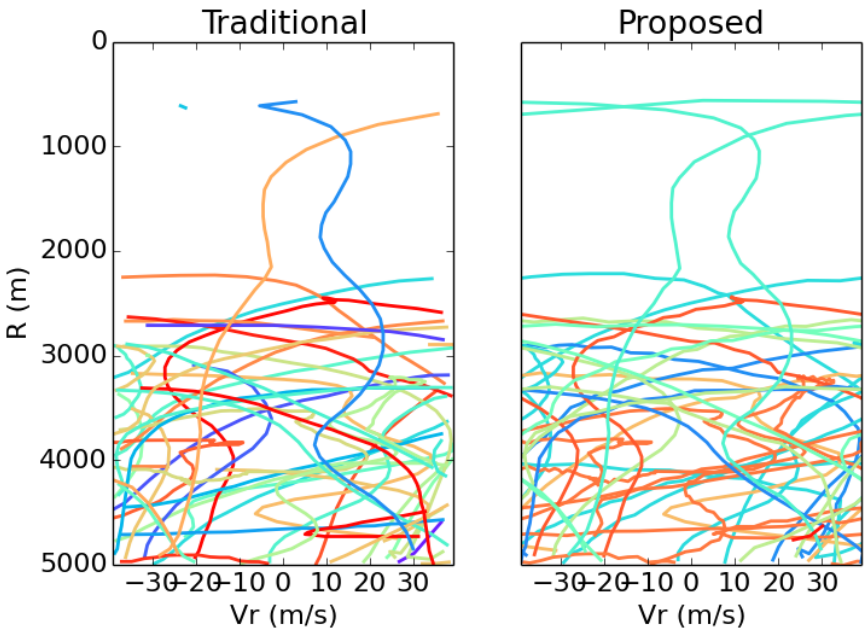

Figure 4.9: FMCW Radar image tracks of the Free airspace flight

	Circuit	Zulu	Free
Traditional	42	42	54
Proposed	14	9	13
Manual	14	9	12

Table 4.2: Number of observed Tracks

4.7. Discussion

The track counts from table 4.2 are very clear. With the proposed tracking algorithm, the number of observed tracks is reduced. Since the experiment was set up in such a way that the observations are identical for both algorithms, this means that the proposed algorithm is better at linking observations together to form a consistent track.

This is also reflected in the figures 4.9, 4.10, 4.11 and 4.12, where the observed tracks are plotted in the radar image and aircraft body frame. It is seen that often observations that form distinct tracks in the traditional algorithms are seen as one single track by the proposed algorithm.

The images in figure 4.10 need further elucidation: in these plots many concentric circle segments are observed. Contrary to what may be intuitive, this is a correct display of the observations. In the circuit flight, around 50% of the time the aircraft is making turns. In these manoeuvres, the range to other aircraft is

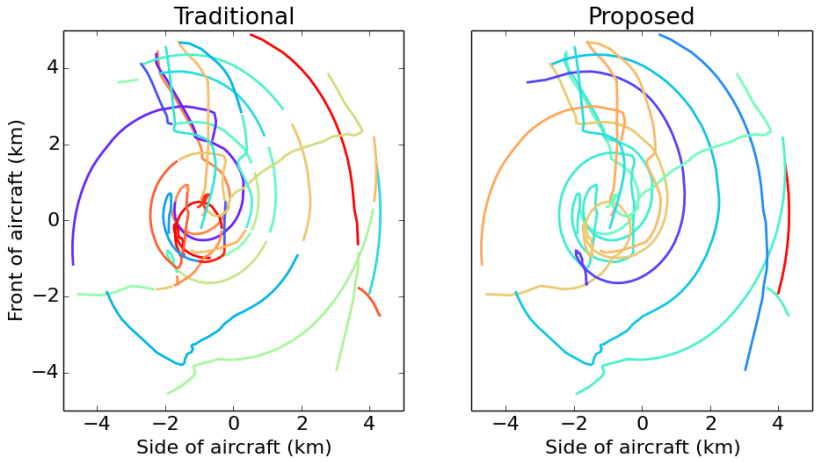

Figure 4.10: Tracks in horizontal aircraft frame of Circuit flights

not significantly affected but the relative direction of the aircraft is. And since the plots are made in an aircraft body fixed frame of reference, this results in concentric tracks.

In figure 4.11, another phenomenon can be observed: two simultaneous tracks of which the observations are mixed up. This can be seen in the top-left corner of the image, and in the centre, where a link is drawn between two distinct tracks. These tracks are easily distinguishable in the aircraft body frame, but in the $R - V_R$ image this distinction cannot be made and they are interchanged by the traditional algorithm. The proposed tracking algorithm improves on this and prevents mixing of tracks.

The tracks from figure 4.12 are also suited for further discussion. It can be seen that in the flight in the free airspace, one other aircraft happened to come very close to the radar-equipped one. But exactly at the closest point, when awareness of the position of the other aircraft is most critical, the track was lost. This does not happen with the improved algorithm. The reason for this is the link between R and V_R, as described in paragraph 4.3.3. When an aircraft is close, the change in Doppler can be very quick, because the time between a (near) heads-on situation and flying away from each other can be only a few seconds. The improved model is capable of computing that change during the flight, and is therefore capable of tracking the other aircraft.

Lastly, the changes in innovation need to be discussed, which were found in table 4.1. It is seen that the l^2 norm of the innovation is reduced by the proposed algorithm for all experiments. This is an indication that the system is better at predicting the short-term object behaviour, and therefore it can more accurately couple observations to tracks. This may help in order to prevent switching of tracks such as seen in figure 4.11.

Additionally, it can be seen that the 95% percentile innovation is lower than in

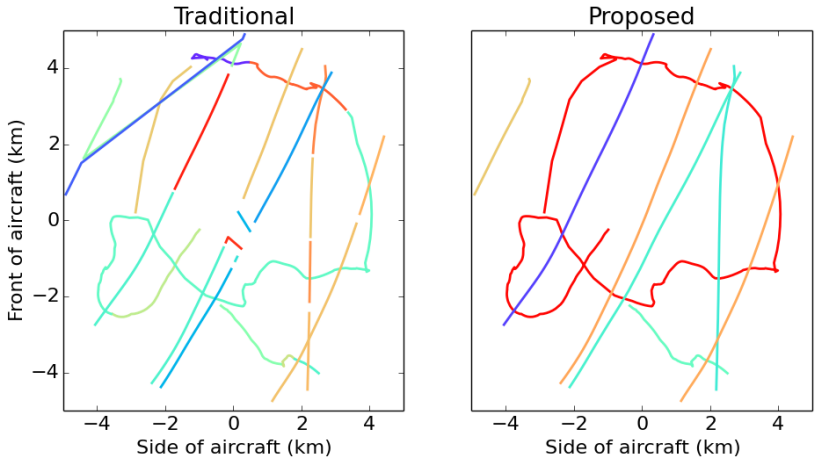

Figure 4.11: Tracks in horizontal aircraft frame of Zulu flights

the traditional algorithm. As discussed in section 4.4.1, a consistently low innovation means that the gate size of the tracking algorithm can be reduced, enabling a higher capacity in terms of number of simultaneous tracks in the simulation. It is seen that the proposed algorithm improves on this aspect, so this is beneficial for application in dense airspaces.

As discussed in section 4.3.1, it is found that the problem of object tracking usually consists of three elements in collaboration: observations, assignment and modelling (as illustrated in figure 4.1). In this chapter, the focus was on the modelling aspect of object tracking. The quality of observations was assumed to be perfect, generated by a high-detail radar simulator. More research to the real generation of FMCW radar data, including the development of proper signal filters, should be performed.

As for the 'assignment' element: so far the Hungarian Algorithm was used in the research, which demonstrated to provide results of good quality. Many research has been performed in the field of visual tracking assignment, and this knowledge may be used in the assignment algorithms, independent from the algorithm developed in this chapter. Therefore, different types of research may supplement and amplify each other.

4.8. Conclusion

In this chapter, an object tracking algorithm is proposed which is suitable for tracking objects in a radar image, such as it can be generated by an FMCW (Frequency Modulated Continuous Wave) radar. The algorithm makes use of specific radar properties such as the Doppler effect, which are taken into account in the predictions of the tracks.

A novel application for this is to use a wide-angle on-board FMCW radar in

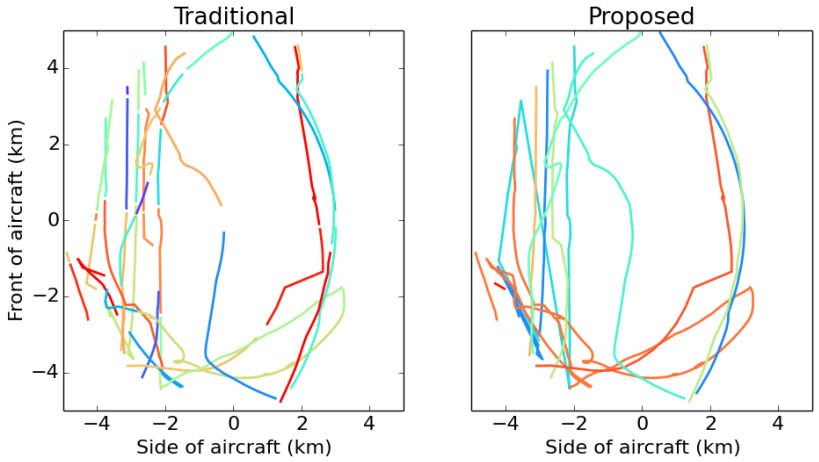

Figure 4.12: Tracks in horizontal aircraft frame of Free flights

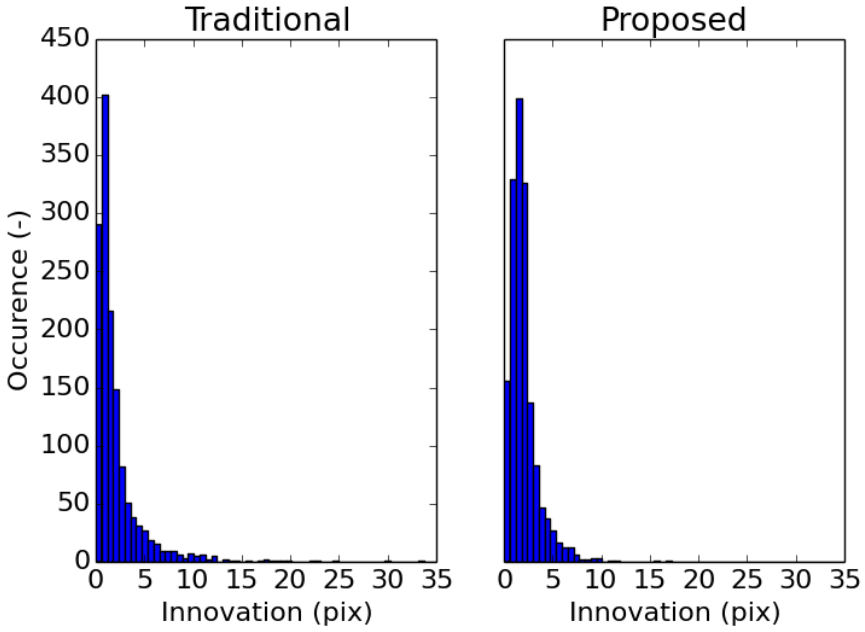

Figure 4.13: Histogram of innovation of the Circuit flight

General Aviation, in order to track the positions of other aircraft in the vicinity of the observer, even if those aircraft are not equipped with any special equipment. This empowers the possibility of independent surveillance, with which objects such as birds, towers and windmills can also be observed. A simulation experiment

is set up to assess the performance of the algorithm in dense General Aviation circumstances, and the results are investigated.

It is found that the proposed algorithm outperforms a traditional object tracking algorithm. Often, a traditional algorithm is not able to connect segments of observations to each other when the observations are aliased to the other side of the radar image or at close distance. The new algorithm is almost always able to make these connections, but one case was found where the new algorithm misconcluded that a series of observations consisted of two tracks instead of one.

Additionally, the accuracy of the proposed algorithm was tested. It was found that the new algorithm is better in predicting the progression of a track than standard optical imagery, and that systems using the new algorithm may have a higher tracking capacity than traditional algorithms applied to FMCW radar images.

In conclusion, the proposed tracking algorithm improved the internal Kalman model of the observed tracks to include aliasing and the relation between distance and radial velocity. It is found that this is an important improvement for the object tracking in FMCW radar images. This new model may be combined with existing and upcoming research on the quality and the assignment of observations.

References

[1] A. Yilmaz, O. Javed, and M. Shah, *Object tracking: A Survey,* ACM Computing Surveys **38**, 13 (2006).

[2] E. Trucco and K. Plakas, *Video tracking: A concise survey,* IEEE Journal of Oceanic Engineering **31**, 520 (2006).

[3] Y. Cai, N. de Freitas, and J. Little, *Robust Visual Tracking for Multiple Targets,* Computer Vision – ECCV 2006 , 107 (2006).

[4] C. J. Veenman, M. J. T. Reinders, and E. Backer, *Resolving motion correspondence for densely moving points,* IEEE Transactions on Pattern Analysis and Machine Intelligence **23**, 54 (2001).

[5] F. Technology, *System Design and Compatibility*, Tech. Rep. 1 (FLARM technology GmbH, 2015).

[6] F. Folster, H. Rohling, and U. Lubbert, *An automotive radar network based on 77 GHz FMCW sensors,* IEEE National Radar Conference - Proceedings **2005-Janua**, 871 (2005).

[7] C. Naulais, *General Aviation Radar System for Navigation and Attitude Determination*, Ph.D. thesis, Delft University of Technology (2015).

[8] H. W. Kuhn, *The Hungarian Method for the Assignment Problem,* Journal of Naval Research Logistics **2**, 83 (1955).

[9] A. G. Amitha Perera, C. Srinivas, A. Hoogs, G. Brooksby, and W. Hu, *Multi-object tracking through simultaneous long occlusions and split-merge conditions,* in *Proceedings of the IEEE Computer Society Conference on Computer Vision and Pattern Recognition*, Vol. 1 (2006) pp. 666–673.

[10] P. Konstantinova, A. Udvarev, and T. Semerdjiev, *A study of a target tracking algorithm using global nearest neighbor approach,* in *Proceedings of the 4th International Conference on Computer Systems and Technologies E-Learning - CompSysTech '03* (2003) pp. 290–295.

[11] A. B. Poore and S. Gadaleta, *Some assignment problems arising from multiple target tracking,* Mathematical and Computer Modelling **43**, 1074 (2006).

[12] G. Welch and G. Bishop, *An Introduction to the Kalman Filter,* in *An Introduction to the Kalman Filter*, Vol. 8 (Chapel Hill, 2001) pp. 1–81, arXiv:arXiv:1011.1669v3 .

[13] A. F. Genovese, *The Interacting Multiple Model Algorithm for Accurate State Estimation of Maneuvering Targets,* John Hopkins Apl Technical Digest **22**, 614 (2001).

[14] S. J. Orfanidis, *IEEE Transactions on Communications*, Vol. 20-5 (Pearson Education Inc, 2004) pp. 1046–1047.

[15] M. S. Lee and Y. H. Kim, *Design and performance of a 24-GHz switch-antenna array FMCW radar system for automotive applications,* IEEE Transactions on Vehicular Technology **59**, 2290 (2010).

[16] A. G. Stove, *Linear FMCW radar techniques,* in *IEE Proceedings F Radar and Signal Processing*, Vol. 139-5 (1992) pp. 343–350.

[17] N. Wilkins, A. K. Shaw, and M. Shaik, *True time delay beamspace wideband source localization,* ICASSP, IEEE International Conference on Acoustics, Speech and Signal Processing - Proceedings **2016-May**, 3161 (2016).

[18] J. Zhang and S. Wang, *An automated 2D multipass Doppler radar velocity dealiasing scheme,* Journal of Atmospheric and Oceanic Technology **23**, 1239 (2006).

[19] R. Okada, Y. Shirai, and J. Miura, *Object tracking based on optical flow and depth,* in *IEEE/SICE/RSJ International Conference on Multisensor Fusion and Integration for Intelligent Systems* (1996) pp. 565–571.

5

Estimation of Flight State with a Collision Alert Radar

J Maas, R Van Gent, J Hoekstra

The radar prototype was tested in stationary mode in chapter 3, and dynamic simulations have been performed in chapter 4. But dynamic tests are also required, since the radar is designed to be taken on board of an aircraft for mobile hazard detection. The movement of the aircraft is expected to have a strong effect on the radar output, since the radar makes use of the Doppler effect to generate its output.

In this chapter, the radar is taken on board of a small aircraft that performs a test flight near a small airfield. It is found that the reflections of the ground are clearly visible in the radar output. Using algorithms that were developed in the radar simulator of chapter 2, it is found that it is possible to determine the ground speed, climb rate and height of the aircraft with respect to the terrain surface.

This chapter is based on the publication *Estimation of Flight State with a Collision Alert Radar*, Journal of Aerospace Information Systems: Vol. 18, No 6, Pg. 347-354, 2021

5.1. Introduction

An airborne Collision Alert Radar is being developed for use in General Aviation (GA) [1–3]. Although its primary goal is not to detect the ground, reflections from the surface are observed in the radar output. These reflections can contain useful information for a GA pilot, since it is crucial to know the aircraft state with respect to the landscape.

The traditional flight instruments of an aircraft provide the pilot with the state information by interpreting the air data. A barometric altimeter can compute the distance above the runway. If the altimeter is set correctly, the altitude is 0 when the aircraft lands on the runway. This way of setting the altimeter will be used in the rest of this chapter, but it does not provide information about the landscape around the airfield [4].

Inertial Navigation Systems (INS) track the aircraft position by Dead Reckoning from take-off, and satellite based navigation (GPS) is used in commercially available navigation apps [5–7]. These systems determine the sensor position with respect to the start of the flight (INS), or with respect to an elliptical approximation of the earth mean sea level (GPS). None of these instruments measure the surface, but the position of the ground is stored in an internal model of the elevation. But this map may be outdated or lack detail, and tree tops increase the terrain height that a pilot wants to avoid, which may not be included in the database. Such faults can lead to unsafe situations.

In order not to rely on an elevation map, it is possible to perform direct measurements on the surface. This can be done with a radar or lidar (Light Detection And Ranging) altimeter [8, 9]. These systems measure the distance to the ground directly below the aircraft. This provides information from a single point and not about the entire landscape. For collision warnings about the landscape in front of the aircraft, the pilot is still dependent on an internal elevation model. The limited functionality of lidar altimetry, combined with a steep price, is the reason that lidar altimeters are not often used in GA.

Progress in the field of microwave sensing has empowered the development of new portable radar hardware for direct measurements [10]. Such a new system can be used in GA, as a Collision Alert Radar. Example functionalities are to detect wind turbines and to track aircraft in 3D. The equipment will cost less than a complete ADS-B/CDTI[1] combination and all 'sense and avoid' functions can be performed simultaneously by a single machine. The application of portable radar in GA looks promising, and the processing methods for it are being developed [3].

In this chapter, the development and testing of a new method are presented. This method will use reflections of the Collision Alert Radar to determine the state of the aircraft: its height and velocity with respect to the landscape. The method makes use of the wide aperture of the radar, as well as the signal filtering properties. It combines several surface reflections in front of the aircraft into one final aircraft state, and it can therefore provide ground collision warnings based on the landscape in front of the aircraft. This is not possible with existing equipment. This system

[1] Automatic Dependent Surveillance Broadcast/Cockpit Display of Traffic Information

Table 5.1: Technical Specifications of the Radar Hardware

Parameter	Value
Carrier Frequency	9.425 GHz
Wavelength	31.83 mm
Sampling Frequency	10 MHz
Pulse Repetition Frequency	4921 Hz
Power Emitted	40 dBm
Bandwidth	10 MHz

has the potential to act as a terrain collision warning system for the pilot.

The underlying hardware and software principles of the state determination method are presented in section 5.2. This method is first tested in simulation experiments described in section 5.3. The radar and the algorithm are subjected to a flight test, which is presented in section 5.4. The results of the flight are presented in section 5.5, and a discussion on these is found in section 5.6. Conclusions on the algorithms are given in section 5.7.

5.2. State Determination Method

Modern microwave sensing hardware and software has improved greatly in the past years, partly empowered by the arrival of self-driving cars [11–13]. Because of this, new systems can be developed which complement the shortcomings of current flight instruments [3]. In this section, the theoretical method for detecting the state is introduced. The hardware and software for this are described in two parts.

5.2.1. Hardware

Frequency modulated continuous-wave (FMCW) radar systems measure range and Doppler velocity (noted as r and V_r) of objects within sensor range [14]. The weight, cost, and power consumption are low enough that they can be taken on board of a small aircraft. If this is done, they can be used to sense the aircraft surroundings [15, 16].

A Collision Alert Radar system is developed for use in GA. This system is expected to increase situation awareness of GA pilots. The system is developed to have a wide aperture, up to 60 degrees horizontally and vertically. Other aircraft can be seen with these radars and ground reflections are observed as well. Technical specifications of the hardware used can be found in table 5.1.

An FMCW radar system can measure both the distance to and the Doppler velocity of an object [11, 14], after antialiasing is performed [17, 18]. The Doppler velocity is the component of the relative velocity in the direction of the object. Direction of Arrival Estimation can help localize a source of reflection in three dimensions [19, 20].

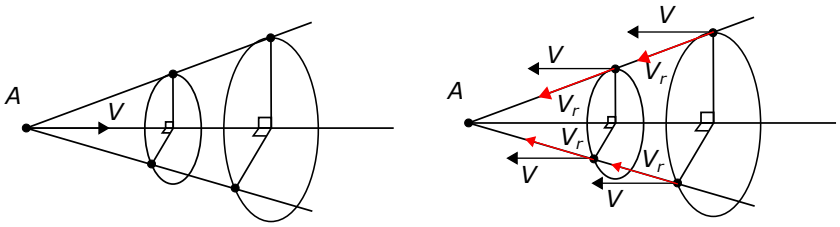

(a) The absolute velocity vector V of A

(b) The relative velocity vectors of the points and their Doppler velocities V_r

Figure 5.1: Aircraft A and four points with the same angle between distance and velocity vector V forming a cone

5.2.2. Software

When the radar system is moving over a landscape, the surface can be represented by a collection of objects with different distances and relative radial velocities. The measured signals can be used to determine the instantaneous state of the system.

The landscape is modelled as an inertial flat plane which reflects emitted radar signals back to the system. The effect of this assumption will be investigated in Section 5.3. Since the surface is not moving, the relative velocity vector is equal at all locations on the surface.

Radial velocity is defined as the component of the relative velocity vector in the direction of the object [18]. Since the relative velocity is the same everywhere, this is only dependent on the angle between the distance and velocity vectors of a point.

This means that two points will have an equal radial velocity only if the angles between the line from the aircraft to the point and the aircraft velocity vector are equal to each other. As illustrated in Figure 5.1, this means that all points with the same radial velocity must lie on a three-dimensional cone around the system velocity vector.

A contour plot on the surface is created, connecting the points on the surface with equal radial velocity. Since all such points must lay on the three-dimensional cone and on the surface plane, the resulting curves are hyperbolas, parabolas and ellipses. The transverse axes of the hyperbolas are the projection of the axis of the cones, i.e. the aircraft velocity vector. A second contour plot is added to the figure, connecting surface elements with the same distance to the system. The result is seen in Figure 5.2.

From Figure 5.2 it is observed that for a given distance to the system, multiple radial velocities exist. For this given distance, the maximal and minimal radial velocities can be found where the hyperbolas are tangent to the circle. Since the center of this circle lies on the transverse axes of the hyperbolas, the two types of contour plots must be tangent at the vertices of the hyperbolas, which is indicated as the dotted line in the figure.

This means that for a given distance to the system, the maximal and minimal radial velocities can be found at the transverse axis of the hyperbolas. This axis is the projection of the system velocity vector on the plane, which will be called the

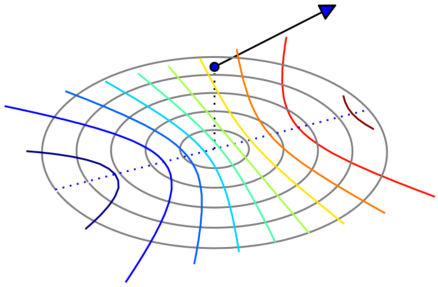

Figure 5.2: 3D view of a system with a velocity above a flat surface, with contour plots of equal distance (grey) and radial velocity (colours)

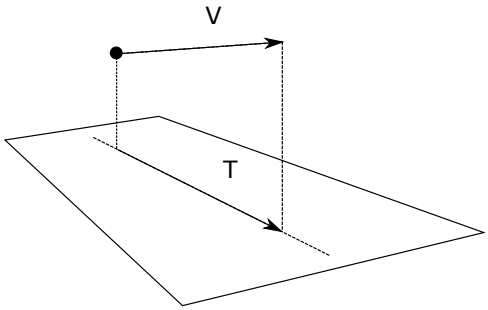

Figure 5.3: 3D view of the track vector T as the projection of the velocity vector V on the ground

track vector. The track vector is illustrated in Figure 5.3.

The FMCW radar can measure the distance and radial velocity of all points that form the surface. It is now found that:

For a given distance, the surface points with the maximal and minimal radial velocities must lay on the track vector of the radar system. These points are significant, because they can be used to derive the aircraft state, as will be discussed in Section 5.2.2 below.

This is also given in mathematical notation. Say S is the collection of points p on the surface, and V is the velocity vector of the aircraft. Note $V_r(p)$ and $r(p)$ as the Doppler velocity and the range of p. Then it follows:

$$S = \{p : p \text{ on surface}\} \tag{5.1}$$

$$S_x = \{p : p \in S, r(p) = x\} \tag{5.2}$$

$$T = \{p : p \in S, p \text{ below } V\} \tag{5.3}$$

$$p \in T \Leftrightarrow V_r(p) = \max\{V_r(s) : s \in S_{r(p)}\} \tag{5.4}$$

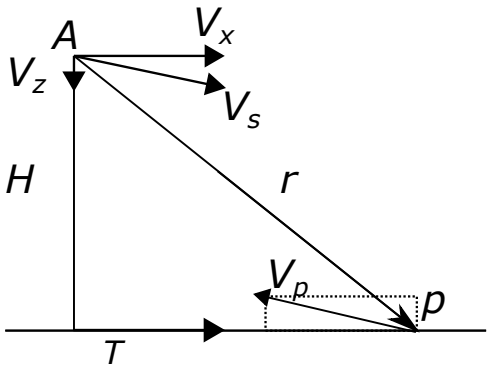

Figure 5.4: Side view of the geometry between a moving aircraft A and a point p on the track vector T

State Finding Theory

In Figure 5.4 a side view is given of a radar system above a surface. According to the theorem in the previous section, let point p be the point with the highest radial velocity V_R of all measurements with distance r. Therefore, point p must lay on the track vector of the radar system.

The radar system moves with a velocity of V_S. This means that the relative velocity vector of p is given as:

$$\vec{V_p} = -\vec{V_S} = \begin{bmatrix} -V_X \\ -V_Z \end{bmatrix} \tag{5.5}$$

The radial velocity (which is measured), is a component of this relative velocity vector:

$$V_r = \frac{\vec{V_p} \cdot \vec{r}}{r} = \begin{bmatrix} -V_X \\ -V_Z \end{bmatrix} \cdot \begin{bmatrix} \sqrt{r^2 - H^2} \\ H \end{bmatrix} \frac{1}{r} \tag{5.6}$$

To get rid of the vector notation in equation 5.6, it is written out completely. Then calculus is applied to sort out the terms in groups of radar parameters r and V_r (which are measured) and system parameters V_X, V_Z and H (which are unknown). These steps are shown below:

$$V_r \cdot r + V_Z \cdot h = -V_X\sqrt{r^2 - H^2} \tag{5.7}$$

$$(V_r \cdot r)^2 + 2V_r r V_Z H + (V_Z \cdot H)^2 = V_X^2(r^2 - H^2) \tag{5.8}$$

$$(V_r \cdot r)^2 + 2V_r r V_Z H + H^2(V_X^2 + V_Z^2) = r^2 V_X^2 \tag{5.9}$$

$$\frac{1}{V_X^2}(V_r \cdot r)^2 + \frac{2V_Z H}{V_X^2} V_r r + \frac{H^2}{V_X^2}(V_X^2 + V_Z^2) = r^2 \tag{5.10}$$

With multiple measurements of Vr and r, a set of equations can be constructed:

$$\begin{bmatrix} (V_{r_0} r_0)^2 & V_{r_0} r_0 & 1 \\ (V_{r_1} r_1)^2 & V_{r_1} r_1 & 1 \\ \vdots & \vdots & \vdots \\ (V_{r_n} r_n)^2 & V_{r_n} r_n & 1 \end{bmatrix} \begin{bmatrix} a \\ b \\ c \end{bmatrix} = \begin{bmatrix} r_0^2 \\ r_1^2 \\ \vdots \\ r_n^2 \end{bmatrix} \tag{5.11}$$

With the parameters:

$$\begin{aligned} a &= \frac{1}{V_X^2} \\ b &= \frac{2 V_Z H}{V_X^2} \\ c &= \frac{H^2}{V_X^2}(V_X^2 + V_Z^2) \end{aligned} \tag{5.12}$$

The equation is now in the form $AX = B$, with matrices A and B only containing measured data: V_r and r. The other three terms, a, b and c, consist of combinations of V_X, V_Z and H. These are unknown parameters, and they describe the state of the radar system: the velocities tangential and perpendicular to the landscape, and the height above it. If at least three surface points are observed, a least squares solution to the equation can be found and parameters a, b and c are known. Observing more points p increases the accuracy of the a, b and c estimates. The aircraft state can then be computed by inversing the relations from equation 5.12:

$$V_X = \sqrt{\frac{1}{a}} \tag{5.13}$$

$$V_Z = \frac{b}{\sqrt{4a^2 c - a b^2}} \tag{5.14}$$

$$H = \sqrt{c - \frac{b^2}{4a}} \tag{5.15}$$

The challenge is to observe multiple suited surface points with values of V_r and r. The reflections that lay on the track vector must therefore be distinguished from the rest. This can be done in several ways, for example with by estimating the Direction of Arrival of the incoming signal [19]. In this chapter Equation 5.4 is used, as introduced previously.

Using this theorem means that if all observed reflections are sorted in range bins [21], the track vector can be found by selecting the observation with the highest value for V_r. This will provide a set of data points with different values of r and V_r, with which it is possible to compute the aircraft state.

It should be noted that equation 5.4 is based on the assumption that the landscape is a flat plane, which is not the case in reality. The measurements that are taken by the radar will be distorted with respect to those of a flat plane. The effect

is that for a given value of r, there will be a difference in the actual and expected location of the signal reflection. This will be observed in a slightly different direction, which influences the value of V_r. Also, some parts of the landscape may be obstructed by terrain, which will remove expected reflections from the radar results. A solution to cope with this can be to implement a three dimensional Direction of Arrival Estimation method. With this, the assumption from equation 5.4 is unnecessary and Figure 5.4 and equation 5.5 can be set up in three dimensions. With this, the state of the aircraft can be computed accurately over three dimensional terrain.

5.3. Verification by Simulation

A simulation experiment is performed to verify the performance of the state determination algorithm. This section is divided in two subsections, which discuss the setup of the experiment and the simulated results.

5.3.1. Simulation Experiment Setup

As an experiment, a virtual flight is performed in the X-plane flight simulator. The flight was recorded and the radar terrain reflections are simulated once per second. The chosen location is important, since the algorithm makes use of radar reflections of the local landscape. Therefore multiple flight locations are used for this experiment.

Since Equation 5.4 is based on the assumption of a flat landscape, the locations are selected to violate this assumption in increasing order. Digital Elevation Maps (DEM) of Europe[2] are used to quantify the local variance in terrain height. The DEM is divided in pieces of about 1km $\times$ 0.6km and of each segment the Standard Deviation (SD) of the landscape height is taken. In Figure 5.5 the result is displayed as a heatmap, where brighter regions have a more local variance in terrain height.

Five locations are selected for simulation testing. The first is the airfield of Deelen in the Netherlands, since this is the location where a flight test experiment is possible (as described in chapter 5.4). The other locations are coordinates in regions around Europe, which vary from hilly to mountainous. These locations are in the west of England (near Worcester), the Eifel area, the Jura and the Pyrenees. The coordinates are indicated on the map in Figure 5.5. Also, a sixth simulation experiment is performed above a flat plane.

The same simulated flight is used for all experiments. The flight track is plotted over the Elevation Maps, as can be seen in Figure 5.6. As can be seen, some flight locations are higher above mean sea level than others. The altitude of each flight is adjusted, in order to make sure that the average height above the landscape is the same for all simulations.

In order to check how the chosen test locations are related to the rest of the continent, a histogram is made in which the standard deviation of the local terrain elevation is counted for all DEMs available. This histogram (plotted on a logarithmic scale) is seen in Figure 5.7. The values of the locations chosen are indicated in the

[2]The DEMs are retrieved from http://www.viewfinderpanoramas.org/

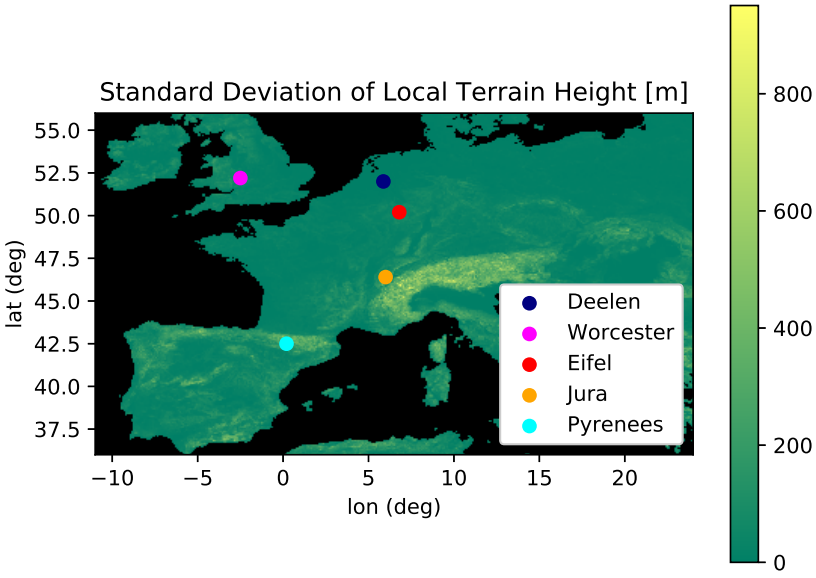

Figure 5.5: Locations of the Five Simulation Experiments within Europe

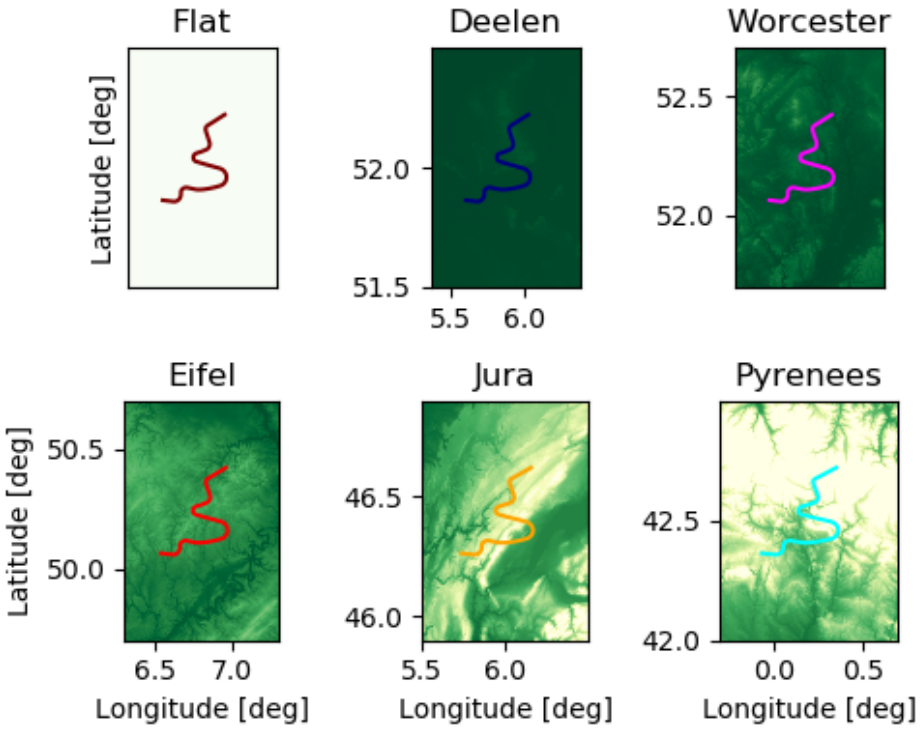

Figure 5.6: Local DEMs at the simulation experiments' locations. Lighter colors indicate higher terrain. The flight tracks are drawn with colored lines.

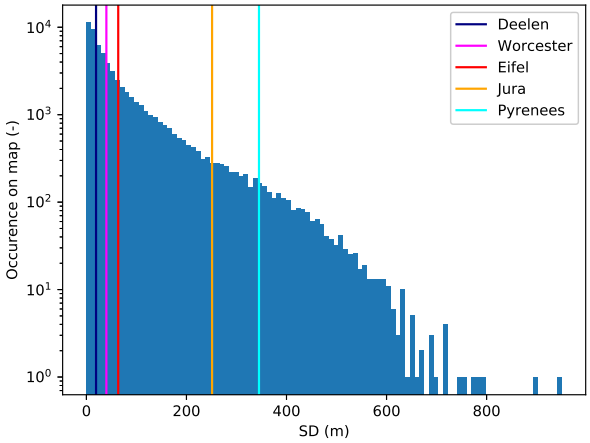

Figure 5.7: Histogram of occurrences of local terrain SDs in the DEMs of Europe

figure as well. The values of Figure 5.7 are also displayed in Table 5.2. The standard deviation of the local terrain elevation is given, as well as the percentage of the map in Figure 5.5 which has a lower local SD than the location.

Table 5.2: Values of local terrain height SD and how this compares to the rest of Europe

Location	**SD of local height [m]**	**part of Europe flatter**
Flat Terrain	0	0%
Deelen	19.2	33.4%
Worcester	39.9	52.68%
Eifel	63.6	65.32%
Jura	251.2	93.72%
Pyrenees	345.0	97.24%

5.3.2. Simulation Experiment Results

The results for the simulation estimates are seen in Figures 5.8, 5.9 and 5.10. At first glance it is seen that the algorithm can approximate the simulated values for some of the simulations. For other flights, the results differ from the simulated truth.

As expected, the results deteriorate when the landscape has more height differences. The flat terrain simulations yield results which are very close to the simulated truth. Simulations above the Deelen area also provide consistent results, and this area was found to be more hilly than 33.4% of Europe. For test areas such as the Jura and the Pyrenees the results are unreliable. These test locations represent about the most mountainous landscapes of Europe.

Numerical values of the height estimate differences can be seen in Table 5.3.

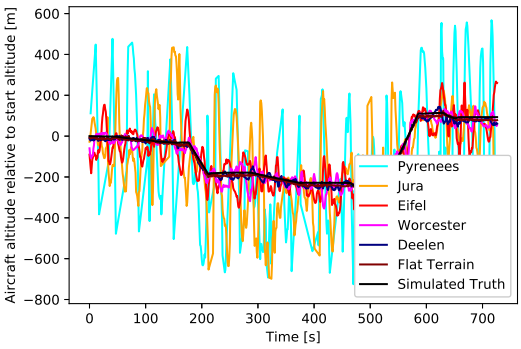

Figure 5.8: Height results of the state algorithm for simulated radar data, and the true values

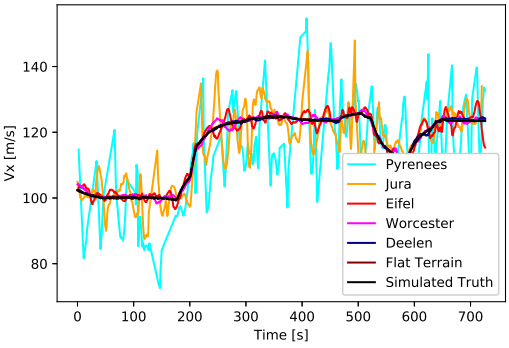

Figure 5.9: Horizontal velocity results of the state algorithm for simulated radar data, and the true values

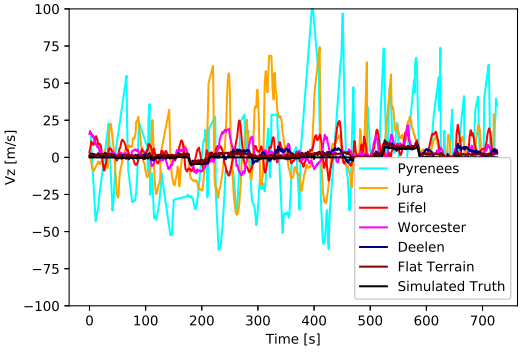

Figure 5.10: Vertical velocity results of the state algorithm for simulated radar data, and the true values

The algorithm seems unsuitable for flight over mountainous regions, but it appears that the algorithm can provide accurate results when used above regions with low local height SD. Is it also observed that a low-pass filter may help remove high-frequency noise from the results.

Table 5.3: Mean and Standard Deviation of height estimate errors of simulated flights at different locations

Location	Mean error [m]	SD of the error [m]
Flat Terrain	8.5	6.5
Deelen	10.3	13.1
Worcester	11.3	35.8
Eifel	20.4	70.5
Jura	130.0	451.1
Pyrenees	381.7	821.6

5.4. Flight Experiment

In section 5.2, the state finding method has been developed. Preliminary results from a simulation experiment indicate that the method can yield desired results. After this, the algorithms were used in a flight test in the Netherlands. This experiment is described in this section.

The aircraft used is a Pipistrel Virus, and two freight containers are attached to the wings. In the front of one of the containers is the radar hardware. The radar antennas have a range of 3 km and they are aimed to the front and downwards, such that they can always receive reflections from the track vector. The radar measurements are able to determine the range to a reflection accurate within 20 m, and the radial velocity is accurate to 0.3m/s. An image of the aircraft can be seen in Figure 5.11, and the aperture and aim of the antenna are illustrated in Figure 5.12.

The flight was performed on the 23rd of October 2019, under Visual Meteorological Conditions. The location was the military airfield of Deelen, in the Netherlands, and the airspace was closed for other traffic. The pilot flew circuits around the airfield with increasing altitudes. The aircraft's true location and velocity were measured using an on-board GPS device and they are plotted in Figure 5.13. The FMCW radar was operational during the entire flight, including taxiing, similar to the GPS. The radar state results are compared to those of the GPS.

5.5. Results

The results of the experiment can be seen in Figures 5.14 and 5.15. These Figures both contain two Subfigures. In Figure 5.14 the velocity results are given in horizontal and vertical direction. In Subfigure 5.15a the GPS results are seen unmodified. In Subfigure 5.15b the GPS results have been calibrated such that the height above the published airfield altitude is given.

The light green line in the background is the raw radar data, and it can be seen

Figure 5.11: The test aircraft, with the radar in the port freight container

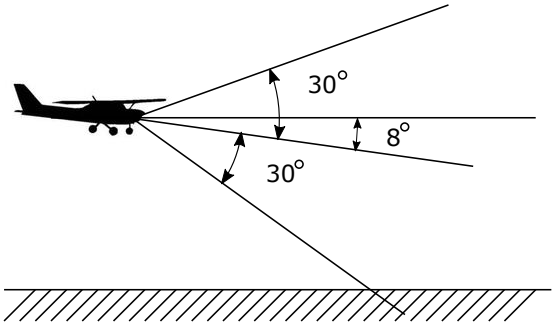

Figure 5.12: The aperture and direction of the radar, as mounted on the aircraft

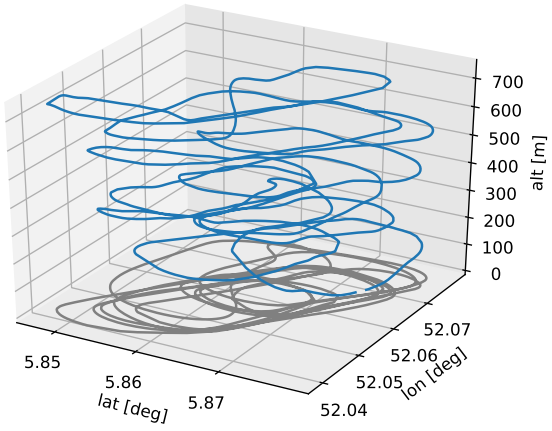

Figure 5.13: The three-dimensional flight path is indicated with the blue line in the figure. The grey line is the projection of the flight path on the horizontal plane. It can be seen that the flight path contains circuits of increasing altitude.

that high frequency variations are present. The first step in the computations is to apply outlier filtering and to discard data points of which the height differs by more than 150m from the GPS data. 15% of the data was removed in this manner.

The other data results are fed to a simple Kalman filter to remove the variations of the signal [22]. Since the height and vertical speed are related to each other, the linear model for the filter used is:

$$x := F \cdot x = \begin{bmatrix} 1 & 0 & 0 \\ 0 & 1 & 0 \\ 0 & -dt & 1 \end{bmatrix} \begin{bmatrix} V_X \\ V_Z \\ h \end{bmatrix} \tag{5.16}$$

The negative sign in the equation is a consequence of V_Z being defined positive downward, which is the opposite direction of H, as was seen in Figure 5.3.

Similarly, it should be noted that the values for V_Z in the Figure 5.14b are also positive downwards. Kalman filtering does improve the accuracy of the results, as expected. Numerical values of the results are displayed in Table 5.4.

From Table 5.4 it is seen that the estimates of the velocity have a small offset of several centimeters per second. The standard deviation is larger, in the order of several meters per second.

It is also seen that the height measurements are on average 36m off, and that their standard deviation is of equal size. This will be discussed in more detail in Chapter 5.6.

The Kalman Filter removes high-frequency noise from the measurements and

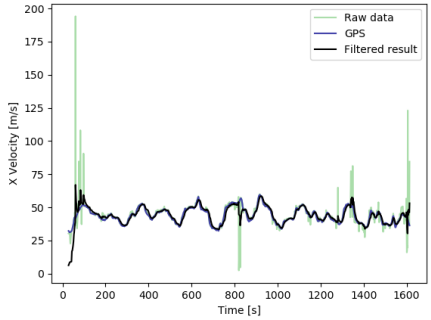

(a) Horizontal velocity results by GPS, radar and filter

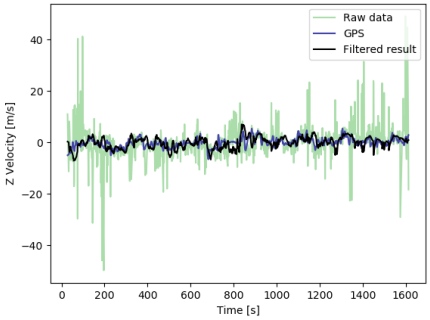

(b) Vertical velocity results by GPS, radar and filter

Figure 5.14: Velocity results by GPS, radar and filter

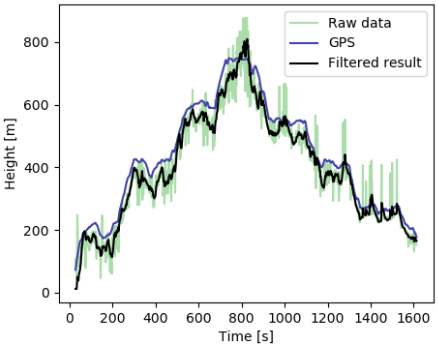

(a) No calibration performed

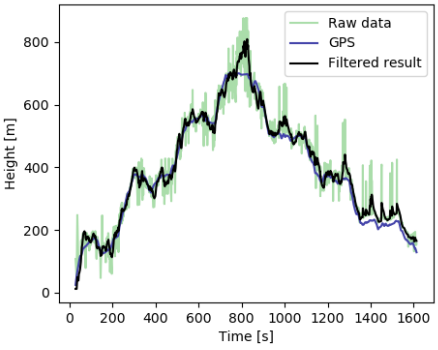

(b) Calibrated with airfield altitude

Figure 5.15: Height results by GPS, radar and filter

Table 5.4: Results of the State Determination algorithm compared to a GPS recorder

	Raw Data		Filtered Results	
	Mean Difference	**SD**	**Mean Difference**	**SD**
V_X	-0.42m/s	6.36m/s	-0.19m/s	2.99m/s
V_Z	0.21m/s	5.76m/s	-0.13m/s	1.98m/s
H	36.27m	36.83m	36.57m	23.82m

improves the results. The mean error of the velocity measurements becomes smaller and the standard deviation is reduced for all measurements. Only the average difference in the altitude measurements does not improve when a Kalman filter is applied, but it is still around 36m. This will be discussed further in the next section.

5.6. Discussion

As noted in the previous chapter, the height difference between GPS and radar is on average 36m off. The origin of this is the difference in GPS altitude and terrain elevation. Whereas GPS computes the altitude above the earth model, the radar uses the reflections of the actual terrain. At the start of the flight, before take-off, the GPS indicated an altitude of 35.97m. This explains why the radar has a mean difference of about 36m, or about 120ft.

A solution to this GPS error can be to calibrate the height at the start of the flight, which will yield results similar to those in Figure 5.15b. However, this solution only guarantees a local fix, and it also does not prevent other faults in the landscape model, including the height of trees. If relying only on GPS during a flight, a risk of terrain collisions is still present.

The height estimates are dependent on the position of the radar reflections. If trees are present, the radar signals will not reach the ground but reflect back on the leaves of the trees. A canopy of trees acts as a radar reflecting plane, parallel to the ground. This means that trees and other foliage increase surface height, and therefore decrease the radar height further. This is useful for the pilot, who wants to avoid flying into the canopy.

In Figure 5.14a it is seen that the V_X measurements are often very close to the actual speed, but that they are several times distorted by a few outliers which have not been removed by the first filter. These outliers affect the mean error and standard deviation, and their influence is reduced effectively by a high frequency noise filter. In this study a Kalman filter was used.

Apart from the height difference, it is observed that the algorithm accuracy is similar to the performance of the hardware, of which the range accuracy is within 20m and the radial velocity accuracy is 0.3m/s.

The vertical speed has more accurate results than the horizontal speed, which is surprising since the radar was pointed to the front of the aircraft. This meant that most of the reflections observed will lay in front of the aircraft, and therefore have a high horizontal radial velocity. It was therefore expected that the algorithm would

be able to tell the horizontal velocity more accurately than the vertical velocity. The Kalman filter uses the relation between vertical speed and height, so extra information is available for a good estimate for both parameters. This can be a reason why the vertical velocity is more accurate.

Considering the uncertainties of the systems, it is found that the radar is less accurate than the GPS, but it is not dependent on a database to find the clearance to the ground. GPS determines the position relative to the earth ellipsoid approximation with a horizontal accuracy of $4m$ and a vertical accuracy of $8m$. For GPS altimetry, the uncertainty can be expressed as $8m + ground\ database\ uncertainty + unknown\ height\ of\ trees$. For the radar system, the standard deviation is $24m$.

Relating back to the theoretical model and the simulation experiment in section 5.3, it is found that the state finding method is more accurate over flatter landscapes. As found from the Digital Elevation Maps, about 33.4% of the European land is flatter than the landscape around Deelen, which is the test area. This implies that state estimation is possible with this system above at least one third of European land. For mountainous areas however, it is unlikely that the method from this chapter alone is sufficient. Future research may indicate in more detail at what locations this system can provide reliable results.

It should be noted that much space for improvement exists in the radar system. Better outlier filtering can have a significant impact on the V_X estimates, as well as the height tracking. Increasing the measurement rate can be of great influence on the Kalman Filter results as well. This experiment was performed with one observation per second, but sampling rates of 10, 20 or 100 measurements per second are possible with modern day radar systems.

As mentioned in the Introduction, the availability and performance of modern microwave sensors and processors have increased significantly over the past years. In the last five years, the price of the equipment used in this experiment has decreased by a factor of 40, and the gain of available antennas has increased by over 10dB. It is possible that the accuracy of the raw results of the radar system will surpass that of the GPS system in the next decade, for a similar price. A pilot will then be able to use a radar system to provide ground collision warnings.

5.7. Conclusion

A sense-and-avoid radar system is being developed for hazard detection for General Aviation pilots. A prototype of this radar system was tested on board of an aircraft. It was predicted that radar reflections from the ground would be clearly visible in the radar output, by the simulator developed in chapter 2.

In this chapter it was investigated whether these ground reflections could be used to determine the altitude and velocity of the aircraft, using a new algorithm that was presented in this chapter. The system was first developed in the simulator, where experiments indicated that it is indeed possible to estimate these parameters with the radar.

The method was developed with the assumption of a flat earth. A sensitivity analysis was performed in the simulator with which it was assessed whether the method could operate above non flat terrain. It was found that the best results were

obtained above simulated flat landscapes, and the presence of hills and mountains reduced the performance.

The method was also tested with the radar in a local flight, and the results in velocity and altitude estimation were compared to those of a GPS tracker.

It is concluded that the quality of the velocity estimates of the radar approaches the quality of GPS navigation. Accurate filtering techniques are required in the processing of radar data.

It was found that the radar could provide altitude information without the need for calibration, but the GPS needed to be calibrated to the runway height. Also, the radar measured the height above the terrain, including tree heights and landscape shapes. This information may be absent or unreliable in a database that is used for GPS navigation. However, the GPS height results are still more accurate than those of the radar. This difference will be reduced by the application of better filtering techniques and more accurate hardware.

The flight test results demonstrated that state determination by a radar system will be a better option than by GPS, if the user wants to measure his position relative to the surface of the landscape.

The simulation tests indicated that the algorithm performs the best above flat terrain. The landscape data of the flight test location are compared to the data of the entire European landscape, and it can be expected that the flight test results will improve if the experiment was performed at another location anywhere in 33.4% of Europe. For the other 66.6% of the landscape, it is unknown where the state estimation method can work and where it will malfunction. Further flight tests above varying landscapes can help indicate the performance envelope of the method.

If the radar sensor is developed further, and the quality of hardware and software is improved with respect to the prototype, this strategy to find flight state information can become a solution for independent state determination with respect to the local environment around the aircraft.

References

[1] J. Maas, R. V. Gent, and J. M. Hoekstra, *Estimation of Flight State with a Collision Alert Radar,* AIAA Journal of Aerospace Systems , 1 (2021).

[2] J. Maas, R. V. Gent, and J. Hoekstra, *A portable primary radar for general aviation,* PLoS ONE **15**, 1 (2020).

[3] J. Maas, R. V. Gent, and J. Hoekstra, *Object Tracking in Images of an Airborne Wide Angle FMCW Radar,* in *ICRAT International Conference for Research in Air Transportation* (2018) p. 8.

[4] US Department of Transportation, *Problems in Worldwide Standardization of the Units of Height Measurement*, Tech. Rep. (Federal Aviation Administration, 1978).

[5] W. Y. Ochieng, K. Sauer, D. Walsh, G. Brodin, S. Griffin, and M. Denney, *GPS integrity and potential impact on aviation safety,* Journal of Navigation **56**, 51 (2003).

[6] W.-W. Kao, *Integration of GPS and dead-reckoning navigation systems,* in *Vehicle Navigation and Information Systems Conference*, Vol. 2 (1991) pp. 635–643.

[7] L. Zhao, W. Y. Ochieng, M. a. Quddus, and R. B. Noland, *An Extended Kalman Filter Algorithm for Integrating GPS and Low Cost Dead Reckoning System Data for Vehicle Performance and Emissions Monitoring,* Journal of Navigation **56**, 257 (2003).

[8] D. Nitti, F. Bovenga, M. Chiaradia, M. Greco, and G. Pinelli, *Feasibility of Using Synthetic Aperture Radar to Aid UAV Navigation,* Sensors **15**, 18334 (2015).

[9] J. Maas, V. Stefanovici, R. V. Gent, and J. Hoekstra, *Validation of GPS by Ground Scanning Radar,* in *ICRAT International Conference for Research in Air Transportation* (2020) pp. 1–8.

[10] E. Nyfors, *Industrial Microwave Sensors—A Review,* Subsurface Sensing Technologies and Applications **1**, 23 (2000).

[11] M. S. Lee and Y. H. Kim, *Design and performance of a 24-GHz switch-antenna array FMCW radar system for automotive applications,* IEEE Transactions on Vehicular Technology **59**, 2290 (2010).

[12] F. Folster, H. Rohling, and U. Lubbert, *An automotive radar network based on 77 GHz FMCW sensors,* IEEE National Radar Conference - Proceedings **2005-Janua**, 871 (2005).

[13] R. O. Chavez-Garcia and O. Aycard, *Multiple Sensor Fusion and Classification for Moving Object Detection and Tracking,* IEEE Transactions on Intelligent Transportation Systems **17**, 525 (2015).

[14] A. G. Stove, *Linear FMCW radar techniques,* in *IEE Proceedings F Radar and Signal Processing*, Vol. 139-5 (1992) pp. 343–350.

[15] C. Naulais, *General Aviation Radar System for Navigation and Attitude Determination*, Ph.D. thesis, Technische Universiteit Delft (2015).

[16] A. Meta, *Signal Processing of FMCW Synthetic Aperture Radar Data* (TU Delft, 2006) p. 133.

[17] J. Zhang and S. Wang, *An automated 2D multipass Doppler radar velocity dealiasing scheme,* Journal of Atmospheric and Oceanic Technology **23**, 1239 (2006).

[18] S. J. Orfanidis, *IEEE Transactions on Communications*, Vol. 20-5 (Pearson Education Inc, 2004) pp. 1046–1047.

[19] A. J. Weiss and B. Friedlander, *Eigenstructure methods for direction finding with sensor gain and phase uncertainties,* Circuits, Systems, and Signal Processing **9**, 271 (1990).

[20] A. K. Shaw, *Improved Wideband DOA Estimation Using Modified TOPS (mTOPS) Algorithm,* IEEE Signal Processing Letters **23**, 1697 (2016).

[21] D. Koks, *How to Create and Manipulate Radar Range-Doppler Plots*, Tech. Rep. (Defence Science and Technology Organisation, Edinburgh, 2014).

[22] G. Welch and G. Bishop, *An Introduction to the Kalman Filter,* in *An Introduction to the Kalman Filter*, Vol. 8 (Chapel Hill, 2001) pp. 1–81, arXiv:arXiv:1011.1669v3 .

6

Validation of GPS by Ground Scanning Radar

J Maas, V Stefanovici, R Van Gent, J Hoekstra

In chapters 3 and 5, the collision alert radar has been used in stationary mode to detect the presence of other aircraft and in flight in order to determine its own flight state, expressed as velocity and altitude. A second flight test is performed with the radar, in which the radar was not oriented towards the flight direction but to the side of the aircraft. The radar observed many different reflections of the ground, and these were mapped onto a flat plane where they showed clear resemblance to the physical landscape below the aircraft. It was investigated whether the resemblance between the radar reflections and satellite images of the landscape can be used to verify the navigation information from GPS.

Fifteen different methods for processing the images were investigated, and two methods have been found effective in extracting similar features in Google and radar images. These algorithms were always successful in picking the single correct GPS coordinate out of a pool of 300 false ones within 150m of the correct answer, except when the aircraft was making a turn and the radar was pointed to the sky.

It is concluded that a ground-scanning radar on board can be used to validate the results of a GPS, provided that the radar can observe recognizable features that can be compared to a digital map. The type of image processing used to extract the data is crucial for the application.

Part of this chapter is published in *Validation of GPS by Ground Scanning Radar*, ICRAT International Conference for Research in Air Transportation, 2020

Figure 6.1: The test aircraft with the radar in the wingtip

6.1. Introduction

Eyesight is crucial for pilots flying under Visual Flight Rules (VFR). Nevertheless, many different kinds of aides are used in flight. Example functions of these add-ons are collision warnings, navigation assistance and weather forecasts.

Many of these add-ons rely on satellite navigation, such as GPS. But this is often used as a single point of failure, and faults in navigation data can mislead a pilot to taking wrong decisions. This can cause unsafe situations, such as airspace infringements.

In recent years, the availability and quality of microwave sensors and modern sensing techniques have improved significantly. This is partially caused by the demand for self-driving cars and the situation awareness that they need to have. Newly developed microwave sensing hardware can be brought on board of an aircraft, where it may empower new applications for aviation.

A test flight with such hardware was performed (seen in figure 6.1), and it was found that structures on the ground were recognizable in the radar output, by the naked eye. This raises the question: is it possible to double-check the GPS results with the data from the ground?

In this chapter, the possibilities of this manner of navigation are explored. The hardware use in the experiment is described in section 6.2, where it is explained how ground images are created. The test flight performed for the experiment is introduced in section 6.3. Different image processing algorithms for improving the raw results are presented in section 6.4, and the method for assessing the performance of these algorithms is presented in section 6.5. The results are presented in section 6.6, after which a discussion and conclusion follow in sections 6.7 and 6.8.

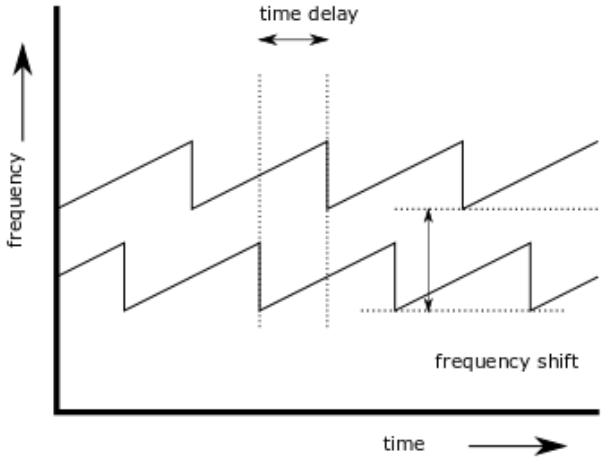

Figure 6.2: FMCW radar principle to find range (time delay) and Doppler (frequency shift) information by comparing an outgoing and incoming signal

6.2. Ground Scanning Hardware

Frequency-Modulated Continuous Wave (FMCW) Radar systems emit microwave signals and receive the reflections of those signals on the surroundings. A comparison of the outgoing and incoming signals yields information about range (R) and Doppler velocity (V_R) of the reflecting surface [1], as is pictured in figure 6.2.

FMCW radars have the properties to be lightweight, cheap and have a low power consumption. This makes them suitable for mobile applications, such as using them on small aircraft. A side-looking radar was mounted on the wingtip of a Socata TB-10, as illustrated in figures 6.1 and 6.3. A radar such as this prototype can weigh 10kgs, be under € 5000 and use 50W power.

When an antenna with a wide aperture is used, multiple reflections are recorded simultaneously, and summed together in one returning signal. Fourier analysis helps differentiate different reflections from one another, provided that the reflection sources have unique values for R and V_R.

Direction Of arrival (DoA) estimation is possible for returned radio signals, when they are recorded by multiple adjacent antennas [2]. The phase difference between the incoming signals can be used to extract the incidence angles of the reflections. Together with the range information of a signal, this yields the position of a reflection in three dimensions.

In this test, a radar system was used with a range of maximum 5000m, and a Nyquist velocity of about 80m/s. For this application, the Nyquist velocity can be considered the maximum possible velocity.

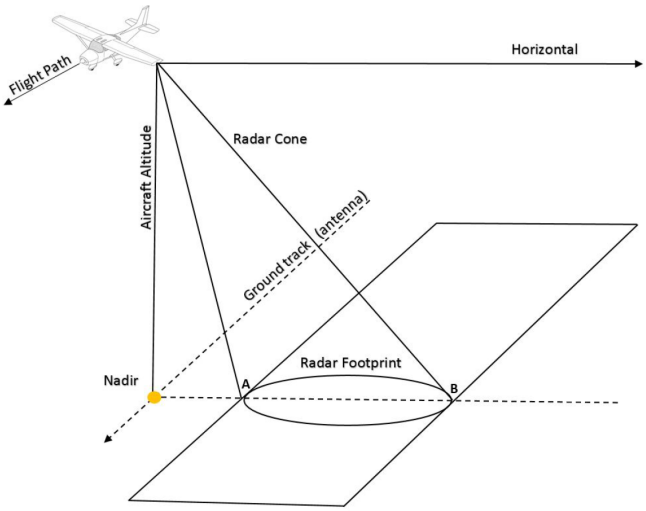

Figure 6.3: Side looking FMCW concept

6.2.1. Differences with SAR

Although the images in figure 6.1 and figure 6.3 may imply that the hardware in this research is an off-the-shelf Synthetic Aperture Radar (SAR) [3], it should be noted that this is not the case.

The radar in this experiment has a wide aperture, being able to observe a large area instantaneously. A SAR has a very narrow aperture, and the width of an image is synthetically created by the movement of the aircraft. A SAR combines many consecutive measurements into one image, which may be disturbed by attitude changes of the platform. Generating a SAR image takes time, but a FMCW image can be generated instantaneously. SAR images are usually generated by post-processing the data, whereas the results of the FMCW radar can be generated live. These differences are illustrated in figure 6.4.

6.3. Test Flight

A local flight with the ground scanning radar on board of the aircraft from figure 6.1 was performed. The flight took place at Teuge airport (EHTE) in the Netherlands, and consisted of two circuits with a touch-and-go in the middle. The aircraft from 6.1 was used as the platform. The flight was logged with GPS, and the track is plotted in figure 6.5.

During this flight, the radar was continuously broadcasting and receiving radio signals. When the returns were filtered, they were processed and their locations were projected onto a flat surface. An example screenshot from the flight is shown in figure 6.6.

In figure 6.6, a greyscale image of the local ground surface beneath the aircraft can be found. The aircraft was located at the center of the semicircle in the image.

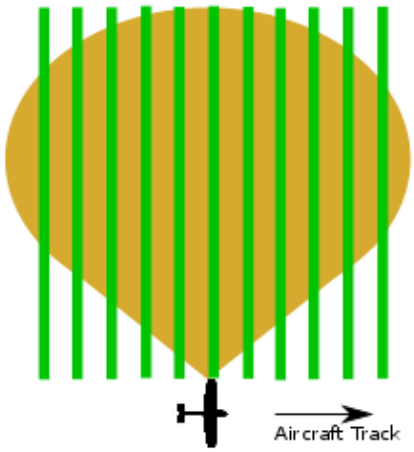

Figure 6.4: Differences in imagery for a SAR (green) and side looking FMCW radar (orange)

Figure 6.5: Test Flight Track, with the runway and taxiways on the north side

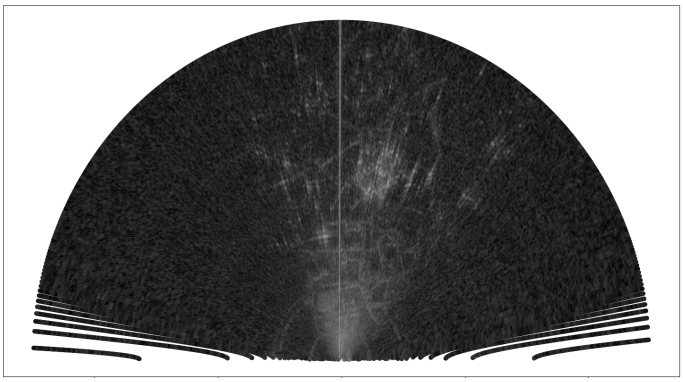

Figure 6.6: Semicircular scatter map around the aircraft with max range 5km

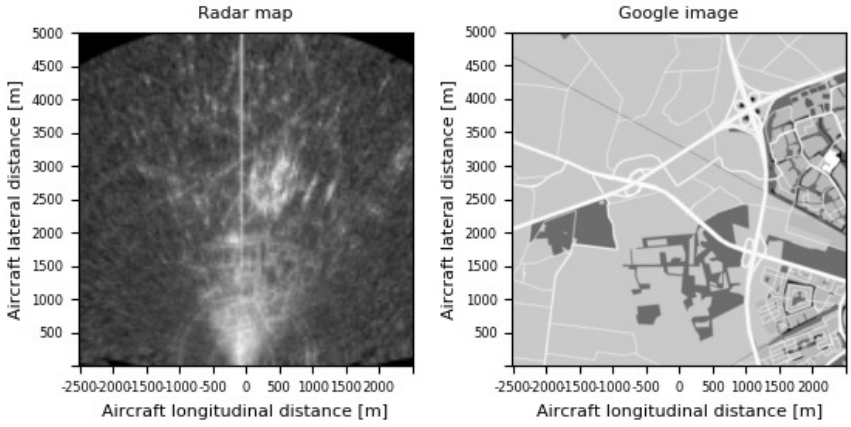

Figure 6.7: Radar map results compared to Google map

The radar was mounted in the left wing, therefore in this image the aircraft was flying to the right.

The brightness in the greyscale image is dependent on the strength of the received signal. It can be observed that many well-reflecting sources are within sight of the radar equipment. The radar, with an aperture of about 60 degrees in horizontal and vertical direction, does not receive signals from everywhere: the sides of the semicircle are dark since no signal is perceived from that direction.

It was noted that the reflections from figure 6.6 appear to form shapes and structures on the ground. These shapes may correspond to buildings, roads, rivers or trees on the ground. To evaluate this statement, the GPS track was used to compare the radar map with a Google map of the same place, same attitude. The result of this is seen in figure 6.7.

In 6.7 a comparison is made between the radar map and the Google map. It is seen that the map from Google contains detailed information on roads locations

and tree areas, but some of this information also appears to be present in the radar map. The location of the big highway appears to be visible as well in the radar map.

Even though it is difficult for a human to compare the radar and Google maps to one another, it does seem that this is within the capabilities of modern image recognition algorithms. If the right strategy for pre-processing is found, an experiment can be performed to evaluate the comparison algorithm. In section 6.4, 15 different image processing algorithms are introduced, which will be subjected to the experiment presented in section 6.5.

6.4. Image Processing Algorithms

In this section, different algorithms are presented that should make comparisons between radar maps and maps from Google as effective as possible. The selection of algorithms is based on a literature study, as well as simple testing in code. The presence of noise and the quality of the radar images excludes the possibility of using point detection algorithms. As such, image transformation algorithms that are robust to noise are desired.

As seen in figure 6.6, a bright area near the center of the semicircle occurs, where the reflections of the radar are stronger than far away. This is a consequence of the shorter range to the aircraft and a higher reflection coefficient, as the ground is more perpendicular to the signal. It was tried to compensate this in an analytic way, but a homogeneous image was never achieved. This means that the solution in recognizing the structures lies in local intensity changes, instead of global variables.

Many of the final algorithms consist of two steps. The first step is a way to map the results of the greyscale to a domain $0 \leq x \leq 1$, and the second step is the way of locally finding the regions of interest. The steps are listed below.

6.4.1. Scaling Steps

- **Gamma Correction** - Also known as Power Law Transform. This function transforms the input image pixel-wise as a power of a chosen value gamma, after scaling each pixel to the domain [4].
- **Thresholding** - The creation of a new binary containing the pixel positions of all intensities that are above a certain threshold.
- **Local Histogram Equalization** - A method which modifies intensities in pixels, to evenly stretch out the entire intensity range, reducing any non-linearity within pixel intensities [5].

6.4.2. Transformation Steps

- **Contour Finding** - A curve joining all of the continuous points (along the borders) that have the same intensity and/or color. The contours are useful for shape analysis and object detection [6].
- **Ridge Operators** - Algorithm that relies on the eigenvalues of the Hessian matrix a matrix of second-order partial derivatives of the intensities of the

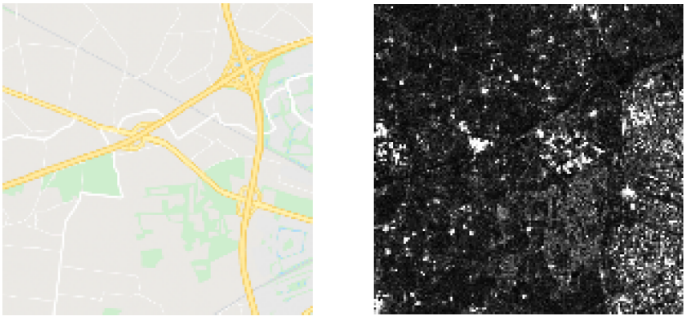

Figure 6.8: Comparison of Google map and Sentinel 1 map

pixels in the image, calculated in order to detect ridge structures where the intensity changes horizontally, but not along the structure [7].

- **Straight Line Hough Transform** - A common algorithm that assigns pixels to the existence of a line that meets width, length and direction properties [8].

- **Blob Detection** - Find a group of pixels that share some common property, for example colour or intensity [9]. In this experiment intensity is used. Since this method is about areas instead of lines in the image, it will not be compared to a Google map, but to the ESA Sentinel 1 database, which contains satellite reflectivity data. This database has more information about areas, but less about lines in the map, as can be seen in the comparison in figure 6.8.

- **Entropy Detection** - The entropy filter is capable of detecting slight variations in the local grey level distribution. It is used to determine regions in the image where many of these small changes are present [10].

- **Watershed** - A marker-controlled Watershed is an image transformation algorithm that interacts with a greyscale image and considers the image as a topographic surface, calculating the gradient of a high energy regions to low energy regions [11].

- **CGAN-CRF** - Unsupervised learning algorithm based on hierarchical Conditional Generative Adversarial Nets (CGAN) and Conditional Random Fields (CRF) Geo Land sensing - categorizing each pixel in satellite images into a category such that we can track the land cover of each area [12].

- **CAE-TVL** - A pre-trained Convolutional Autoencoder with Total Variation Loss (CAE-TVL) for satellite image segmentation as well as generic images [13].

With these different algorithms available, 15 methods are selected for testing in the experiment. These are found in Table 6.1.

Table 6.1: **Image Processing Algorithm Selections**

Method	Transformation 1	Transformation 2
1	Gamma Correction	None
2	Gamma Correction	Blob Detection
3	Gamma Correction	Thresholding
4	Thresholding	Contour Finding
5	Thresholding	Entropy Detection
6	Thresholding	Hough Line Transform
7	Thresholding	Blob Detection
8	Histogram Equalization	Ridge Operators
9	Histogram Equalization	Entropy Detection
10	Histogram Equalization	Watershed Marker
11	Histogram Equalization	Contour Finding
12	None	CGAN-CRF
13	None	CAE-TVL
14	Histogram Equalization	CGAN-CRF
15	Histogram Equalization	CAE-TVL

6.5. Experiment Setup

In order to compare a radar map and a Google map to one another, the Structural Similarity Index Measure (SSIM) is used to quantify the likeliness of the two images. The SSIM is chosen because it takes into account differences in geometry of detected points, even with a strong presence of noise. The SSIM takes into account the luminance, contrast and structure of regions within the image.

The goal of using the radar data is to improve possibilities of navigation, and therefore the radar map will not only be compared to the local Google map based on the aircraft GPS, but also to 300 false alternatives, which are generated by altering the GPS data. An alternative GPS location lays at a distance of 0-150m from the true GPS location, and a heading disturbance of maximum 15degrees is used. This is illustrated in figure 6.9 and figure 6.10.

In figure 6.10 the red circle from figure 6.9 is visible and drawn to scale. It can be seen that even with a maximum of 150m range difference, the two images will still be similar, given the total range of 5km. The task for the computer will be to distinguish the differences between 300 similar images, and to find the correct Google map which corresponds to the radar map. For algorithms 2 and 7, the comparison will not be made to a Google map but to the Sentinel 1 database, as discussed in IV.B. This only changes the image for comparison, all other steps are identical.

6.5.1. Dependent Variables

Three dependent parameters are selected to evaluate the performance of the algorithm. For all 300 images, the SSIM is computed. The Google map with the highest SSIM is selected to be the best match for the given radar map. The GPS coordinates

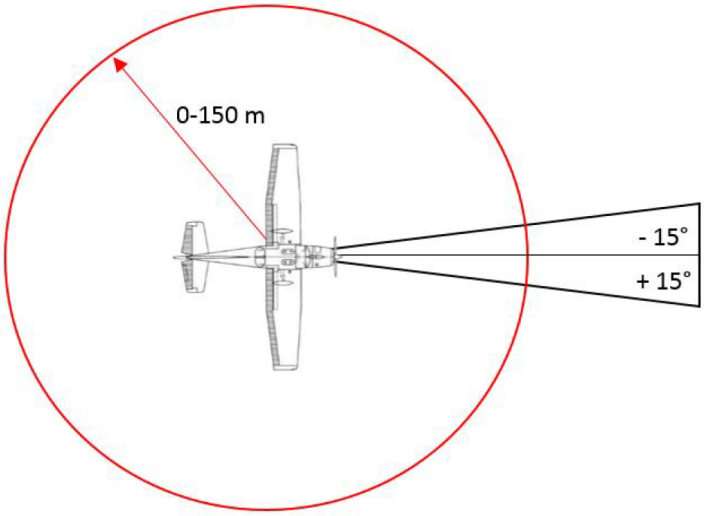

Figure 6.9: Generated GPS faults for alternative locations. The maximum location error is 150 meters, and the maximum heading error is 15 degrees.

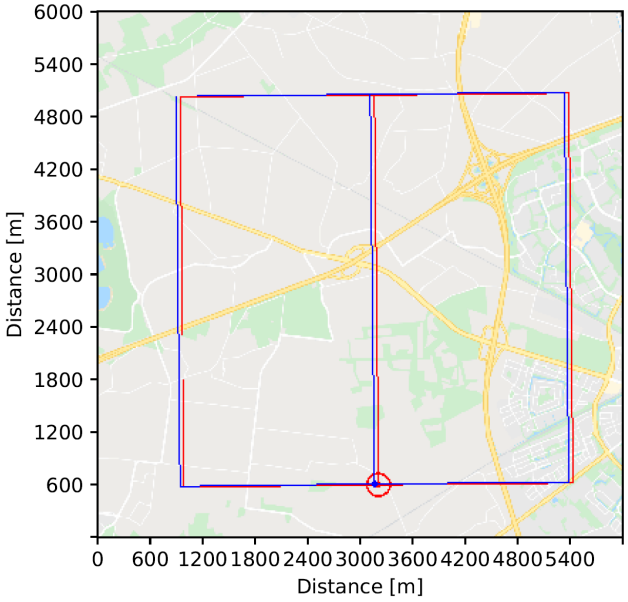

Figure 6.10: The original Google map and an alternative map with GPS errors

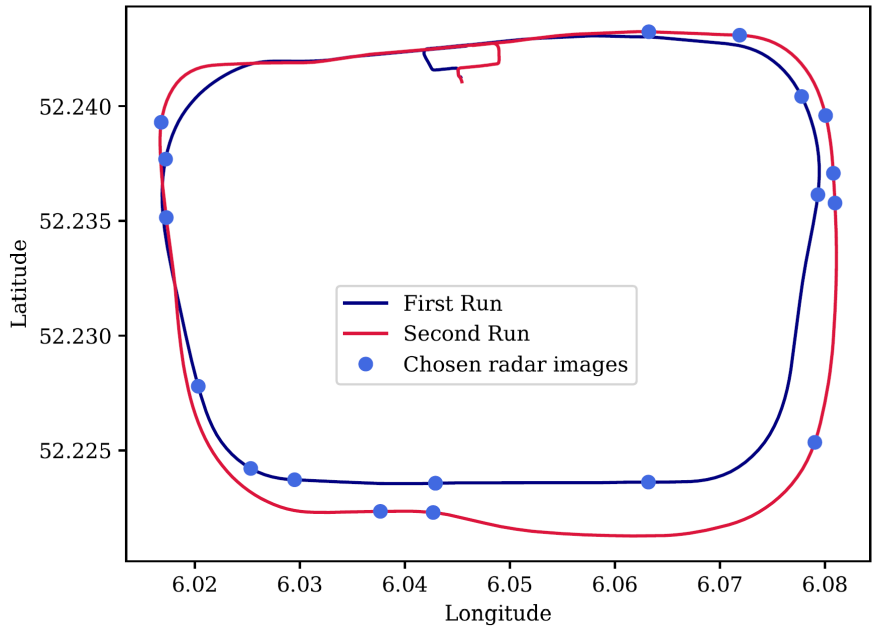

Figure 6.11: The randomly selected points for the detailed experiment

of this generated Google map are then compared to the true GPS coordinates of the measurement. The heading and position errors are noted down, and used as the first and second independent variables.

The third and final dependent parameter is the number of false positives. Out of the 300 false alternatives, it is noted how many score a better SSIM than the original Google map. This number is expressed as a percentage, and should be as low as possible.

6.5.2. Test points

The experiment is conducted in two steps. First, four test points are selected by hand. They were chosen on different parts of the flight for which clear reflections were to be seen in the radar output. The point from figure 6.7 is one of them, the other three are similar. The radar results from these four points are compared to all 15 algorithms from Table 6.1. The three algorithms that perform best under these 'easy' conditions will then be subjected to a further test.

In the second test the best algorithms are subjected to 20 radar data points. These points are selected randomly, on condition that the aircraft is not performing a take-off or landing. In figure 6.11 the locations of the selected points are shown.

Table 6.2: Experiment A Results for 15 Methods

Method	Average Results over 4 Data Points		
	Heading deviation [deg]	Position Error [m]	False Positives [-]
1 Gamma	7	108	53%
2 Gamma Blob	6	68	52%
3 Gamma Thresh.	3	75	50%
4 Thresh. Countour	11	46	39%
5 **Thresh. Entropy**	5	24	23%
6 Thresh. Hough Line	4	53	67%
7 Thresh. Blob	8	35	28%
8 **Histogram Ridge**	0	0	0%
9 **Histogram Entropy**	0	0	0%
10 Histogram Watersh.	6	119	38%
11 Histogram Contour	2	37	89%
12 CGAN	14	126	55%
13 CAE	12	124	53%
14 Histogram CGAN	12	52	45%
15 Histogram CAE	6	112	35%

Table 6.3: Experiment B results for the best 3 Methods

Method	Heading deviation [deg]	position error [m]	False Positives [-]
5 Thresh. Entropy	5	45	42%
8 Histogram Ridge	1	1	14%
9 Histogram Entropy	2	5	9%

6.6. Results

The numerical results of the first test are shown in Table 6.2. In this table, the results for the four data points are grouped together, and the average is taken.

It is seen that methods 8 and 9 yield superior results. For all four experiments, these algorithms were successful in picking the correct GPS image on the hand of the radar map out of a pool of 300 alternative GPS maps. Out of the other algorithms, number 5 was chosen to complement the set of three, predominantly based on its low number of false positives.

After experiment A, the second experiment was run, with only the three best methods and 20 selected points. The distance results of this experiment are shown in figure 6.12, and all results are numerically summarized in Table 6.3.

It is seen that also for the second experiment, methods 8 an 9 are performing well over all. For the majority of the data points, the algorithms manage to find the exact GPS location out of the 300 false alternatives. For method 8, 3 points were not related to the correct GPS position, but a position dozens of meters away. For method 9, 4 points differed from the true GPS. In the next section, these results

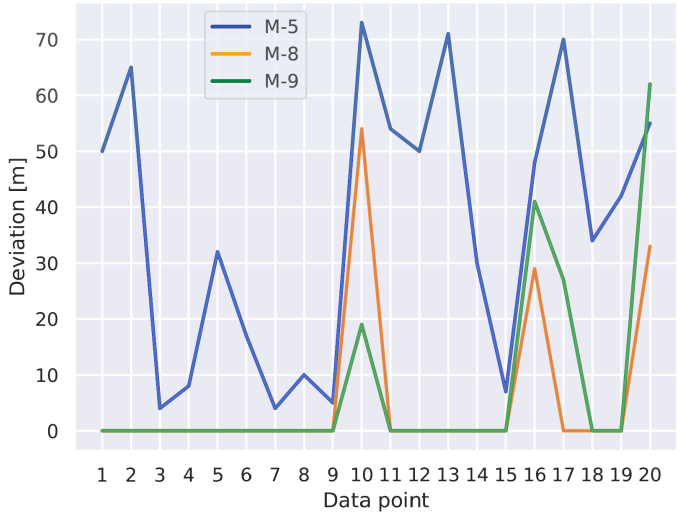

Figure 6.12: position error for the 3 best methods for all 20 data points

are discussed in detail.

6.7. Discussion

In this section, the results from the two experiments are discussed in order. First are the results of experiment A, second are those of experiment B. The third and final part of this section contains a comparison of this radar sensing technique to SAR imagery.

6.7.1. Experiment A

The results for all methods are discussed briefly.

Only Basic Operation

For method 1 only a scaling step was applied on the images. The number of false positives for this method was 53%. This is close to what would be expected if maps were evaluated by a randomizer. In that case the number of false positives would lay around 50%. This highlights the case that special operations are necessary in order to compare the images to each other. Also, a simple operation such as thresholding is not sufficient for the second step, as seen with method 3.

Blob detection

Methods 2 and 7 use Blob detection. This method is based on the assumption that buildings leave dense spots of illumination in the image. For Blob detection, the comparison is made to the Sentinel 1 database (figure 6.8), as the reflectivity information in that database is shaped much like blobs, and therefore suitable for the algorithm. Blob detection reduces a spot of illumination to a circle on the

image; apparently the presence of noise disturbed the circles too much for a decent comparison to be made.

Contour Finding

Methods 4 and 11 use Contour finding. It appeared that the noise present in the images distorted the resulting contours by such an extent that it was impossible to compare them to the contours based on Google maps.

Hough Line Transform

In method 6 it was attempted to connect different visible speckles on the radar map, to form roads. The presence of the noise speckles caused that many different lines could be drawn through the images, which could all be roads in reality. It is possible to tune the Hough Line Transform algorithm with multiple settings, but these attempts were not successful.

Watershed Marker

The Watershed Marker was used in method 10. This algorithm segments the image in multiple regions, based on greyscale results. The method works poorly, since noise is not at all filtered.

Computer learning algorithms

Methods 12, 13, 14 and 15 are based on pre-trained neural network algorithms, with or without scaling before that. All the false positive percentages lay around 50%. 50% is the expected result for a randomizer, so it is concluded that none of the attempts for implementing AI were successful.

The Successful Algorithms

Two algorithms are found to be successful in comparing the radar data to Google maps data. These are Ridge Operators for method 8 and Entropy Detection for methods 5 and 9.

The method of Ridge Operators is used to find edges in the image. In order to do this, the local Hessian Matrix of the image is computed for each pixel, as well as the corresponding eigenvalues. If the eigenvalues are strong in one particular direction, then there must be a line running in that direction. This method is not hindered by noise is used in the medical industry to detect blood vessels in noisy images.

Entropy Detection borrows from the physical term 'entropy', in the sense that it is a method that quantifies how much entropy is present locally in an image. Regions with much contrast between pixels have higher entropy. More homogeneous regions have low entropy. It appears that this method has the same regions highlighted in the Google and radar images.

A comparison of Ridge Operator results and Entropy Detection (only for method 9) is shown in figure 6.13. It is seen that the algorithm is applied both on the radar image and on the Google map. The two results 'M8' are compared to each other using the SSIM, and the two results 'M9' are compared to each other using the SSIM as well.

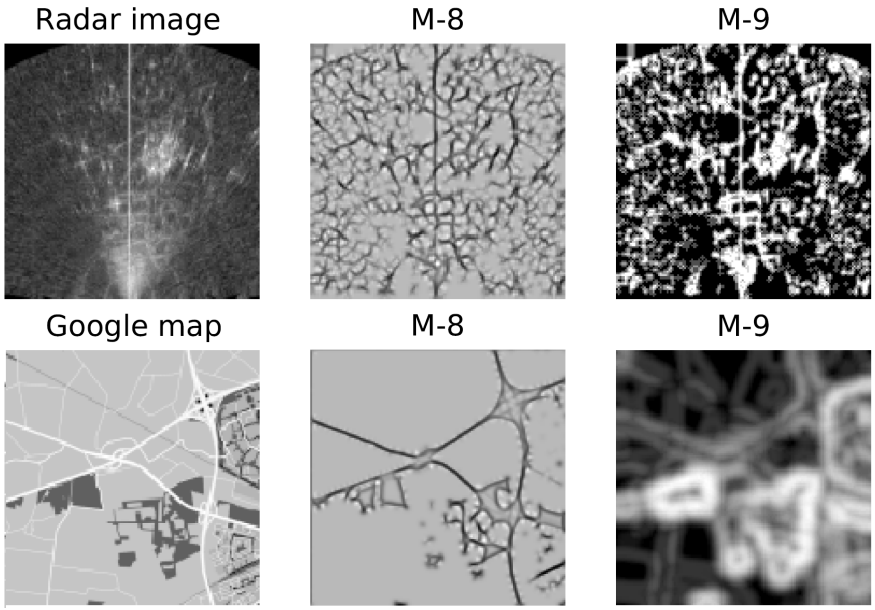

Figure 6.13: Ridge Operators (M8) and Entropy Detection (M9) results

6.7.2. Experiment B

It is found that from the three algorithms selected for the test, method 8 has the best results of all. In the second experiment, where the algorithms are supplied with 20 random in-flight situations, the algorithm could find the aircraft position for 17 situations. The algorithm for method 9 is also a good candidate for being put in practice: it found the correct location 16 times.

In figure 6.12 it was observed that three data points, numbered 10, 16 and 20, yield bad results for all methods. It was investigated if there was a reason behind the collective failure. It was found that these data points are taken when the aircraft was making a right turn. Because of this the left wing went up, and the radar was pointed to the sky. Ground reflections are still received because of the high aperture of the radar, but reflections are difficult to distinguish. This caused trouble for the algorithms. This may be compensated by putting a second radar on the right wing, which would point downward. But because only right turns are made in this flight, this cannot be verified in this experiment.

When the algorithms were off, the error was always in the order of magnitude of tens of meters. If the navigation algorithm is performed at reasonable frequency, an outlier filter can help to differentiate the inconsistent results from the correct ones.

The differences in the two algorithms are too small to yield a definitive answer to the question which one is better. A next step for testing can be to asses the algorithms in a more open setting, where the task is not to find the best answer out of a discrete set, but to find the best matching location on a map. Such an

optimization problem for finding the best match can be solved with extra code, such as a Newtonian solution or a Genetic Algorithm.

6.7.3. Comparison to SAR

It can be said that the method of sensing used in this chapter is comparable to Synthethic Aperture Radar sensing (SAR). In SAR technology, the radar can also be mounted on board of an aircraft, aimed towards the side. A SAR radar differs from the radar that is used here in that the SAR aperture is very narrow, but a wide image can be constructed by connecting observations through time, while the aircraft is moving.

The first difference that should be noted is that the radar in this research can generate ground images instantaneously, but that SAR images need time to be constructed, in which the aircraft is not disturbing the measurements by manoeuvering more than what the SAR algorithms can handle.

Apart from that, it can be said that the image processing algorithms can be applied on SAR imagery as well. It must be noted that the radar images from this research are based on the reflected signal strength. SAR radars measure signal strength as well, but not always is this included in the output image, so this can be of concern for the specific SAR application.

The final aspect that should be noted is the three dimensional nature of the landscape. The radar in this research mapped the observed reflections on a modeled flat plane, assuming that the earth has no height differences. This makes for easy comparisons to two dimensional maps that do not contain altitude, but it will affect the quality of the results when the assumption is invalid. A SAR image can improve on the quality of the results in that situation, since SAR images often contain three-dimensional data.

6.8. Conclusion

In this chapter, the results are presented of an experiment in which the conflict detection radar was mounted laterally on a flying aircraft. It has been noted that visually, structures on the ground could be identified in the radar reflections. It was tested whether computer vision could also distinguish these reflections, and whether these results could be used to determine the aircraft's position as a way to verify the operation of the GPS.

Fifteen different methods were tested. First, they were subjected to a simple experiment, and the best three algorithms were put to the test for an extensive comparison. It was found that a method based on Ridge Operators and one based on Entropy Detection performed exceptionally well. The Ridge Operator algorithm was slightly better, but no definitive verdict can be given based on this study alone.

Both of the algorithms were able to validate the location of GPS, even when provided with 300 similar alternatives that were close around the GPS location. Errors were found when the aircraft was making a turn, thereby aiming the radar away from the ground.

It is concluded that observations of ground reflections from airborne radars can

be used to validate the functioning of a GPS, as long as the radar can observe features on the ground that can be correlated to that on a map of the environment. The use of processing algorithms to extract features from the radar data is crucial for this application.

References

[1] A. G. Stove, *Linear FMCW radar techniques,* in *IEE Proceedings F Radar and Signal Processing*, Vol. 139-5 (1992) pp. 343–350.

[2] A. Paulraj and T. Kailath, *Direction of arrival estimation by eigenstructure methods with unknown sensor gain and phase,* Acoustics, Speech, and Signal Processing, IEEE International Conference on ICASSP '85. **10**, 640 (1985).

[3] D. Nitti, F. Bovenga, M. Chiaradia, M. Greco, and G. Pinelli, *Feasibility of Using Synthetic Aperture Radar to Aid UAV Navigation,* Sensors **15**, 18334 (2015).

[4] E. Reinhard, G. Ward, S. Pattanik, and P. Debevec, *High Dynamic Range Imaging* (Elsevier B.V., 2010).

[5] D. J. Ketcham, R. W. Lowe, and J. W. Weber, *Image Enhancement Techniques for Cockpit Displays* (Defense Technical Information Center, 1976) p. 88.

[6] W. Lorensen and E. Cline, *Marching cubes: a high resolution 3d surface construction algorithm,* in *SIGGRAPH 87* (1987) pp. 163–170.

[7] C. Ng, M. Yap, N. Costen, and B. Li, *Automatic Wrinkle Detection Using Hybrid Hessian Filter,* in *Asian Conference on Computer Vision* (2014) pp. 609–622.

[8] C. Galamhos, J. Matas, and J. Kittler, *Progressive probabilistic Hough transform for line detection,* in *IEEE Computer Society Conference on Computer Vision and Pattern Recognition* (1999).

[9] L. Nretzner and T. Lindeberg, *Feature Tracking with automatic selection of spatial scales,* in *Computer Vision and Image Understanding* (1998).

[10] S. Van der Walt, J. L. Schonberger, J. Nunez-Iglesias, F. Boulogne, J. D. Warner, N. Yager, E. Gouillart, and T. Yu, *scikit-image: image processing in Python,* PeerJ **2** (2014).

[11] L. Shafarenko, M. Petrou, and J. Kittler, *Automatic Watershed Segmentation of Randomly Textured Color Images,* IEEE Transactions on Image Processing **6** (1997).

[12] L. Matikainen, *Object-based analysis of multispectral airborne laser scanner data for land cover classification and map updating,* ISPRS Journal of Photogrammetry and Remote Sensing **128** (2017).

[13] C. Wang, B. Yang, and Y. Liao, *Unsupervised image segmentation using convolutional autoencoder with total variation regularization as preprocessing,* in *IEEE International Conference on Acoustics, Speech and Signal Processing* (2017) pp. 1877–1881.

7

Feasibility of Obstacle Detection using a Passive Radar

J Maas, R Van Gent, J Hoekstra

In this chapter a different approach towards the detection of objects is investigated. Instead of transmitting a waveform at the location of the radar sensor, it is researched whether it is possible to detect reflections of pulses that are transmitted by another source. If this is possible, the hardware required does not need to include a transmitter antenna, only a receiver. This can greatly reduce the required power consumption, weight and cost of the hardware.

It is tested whether the emitted pulses from an Air Traffic Control ground radar can be received by a Software Defined Radio, which is compact enough to be used as a mobile receiver station. It is found that the receiver can consistently detect the presence of buildings up to a distance of 20 kilometers away. However, it was difficult to detect reflections from an aircraft with the hardware and software in the experiment. Further developments may increase the performance of the sensor accuracy and reliability.

This chapter was submitted as *Feasibility of Obstacle Detection using a Passive Radar*, IEEE Transactions on Aerospace and Electronic Systems, 2021

7.1. Introduction

An accurate situation awareness is crucial for safe flight. The detection of obstacles around the aircraft is one aspect of that, which can help a pilot prevent hazardous situations. With reliable obstacle detection, a pilot can maintain a safe distance from buildings and towers on the ground.

When flying under Visual Flight Rules (VFR), a pilot can use eyesight to determine the locations of ground based obstacles. Beacons on top of tall buildings can empower visual detection at night as well. But obstacles may not be detected by human observers in poor visibility conditions. Also, due to sun glare, human error, or obstruction by the own aircraft fuselage, pilots may not detect obstacles even in good weather. Another option to determine the locations of ground based obstacles is to use a map. Many pilots choose to use digital maps, such as navigation apps on mobile devices. These maps may not contain temporary obstacles and must be updated regularly.

An alternative strategy for obstacle detection is to use radio waves, but radar transmitters are often too expensive to be taken on board of a General Aviation aircraft. Therefore an option is to use the bistatic radar principle, where the transmitting and receiving antennas are located at different places [1]. This technique has been known for years but has been implemented only sparsely. This is because the hardware was unmovable and offered little benefit over traditional monostatic radars. But recent developments have brought the Software Defined Radio (SDR) to the market. This hardware is affordable, compact, lightweight and has a low power consumption, and it may empower the application of the bistatic radar principle on a mobile platform.

In this chapter a feasibility study is presented that investigates the possibilities of the principle mentioned above: building a mobile station for detection of obstacles for aircraft. The method of the bistatic radar and the hardware and software are presented in chapters 7.2 and 7.3. An experiment is described in chapter 7.4, of which the results are presented in chapter 7.5. A discussion and conclusions follow in chapters 7.6 and 7.7.

7.2. Hardware

In this section the bistatic radar principle is introduced, as well as the required hardware for it. The chapter contains three subsections: one on the principle, one on the transmitter and one on the receiver.

7.2.1. Bistatic Principle

As opposed to a monostatic radar, the transmitting and receiving antennas of a bistatic radar are located on two different locations[2–4]. These locations can be kilometers apart from each other. This affects the geometry that the radio signal travels, as can be seen in figure 7.1.

The bistatic radar concept has several functional differences with respect to a traditional monostatic one [5]. The strength of the received signal in figure 7.1b is dependent on two dimensions, whereas only the distance to the radar is important

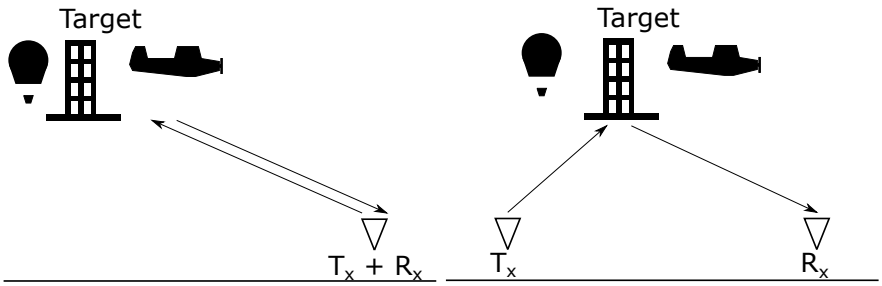

(a) Monostatic (b) Bistatic

Figure 7.1: Geometry for concepts of detection of targets by radar in a monostatic radar concept the radar receiver is at the same location as the transmitter. In a bistatic radar concept these antennas are separated.

in figure 7.1a [1]. Also the reflection angle of the transmission path is important for the strength of the received signal. The type of objects that are visible does not change in a bistatic radar concept: this is still dependent on the signal pattern of the transmitter antenna, as it is in a monostatic setup. Radar Cross Sections are found to vary for monostatic and bistatic concepts, but objects as small as birds and drones may be observed by bistatic radars [4, 6].

Another important difference is that a monostatic pulse radar concept needs to shut down the receiver antenna when the transmitting antenna is turned on. This must be done in order to prevent the wiring from overloading, since the antennas are located close to each other. In the bistatic concept, the distance between the antennas is large enough such that this is not a problem, and the receiving antenna does not need to be turned off periodically. This means that transmission patterns are possible in a bistatic concept which cannot be used in a monostatic setup [7].

It is also important that knowledge of both the transmitter and receiver antennas is required in order to localize any target [3]. One the one hand this knowledge is about the signal frequency and the transmitted waveform (explained in section 7.3.2). On the other hand spatial information is required for localization of obstacles (discussed below).

Localization is done on the horizontal plane on which the radars and target form a triangle (as in Figure 7.1b). The cosine rule can be used to determine the place of the target. Before this can be established, the following information is required:

1. The location of the transmitter antenna
2. The location of the receiver antenna
3. The travel distance from transmitter to target to receiver
4. Direction information to the target

Since the ground radar is directional (it broadcasts its signal in one direction), information point (4) can be found if it is known in what direction the radar is pointing.

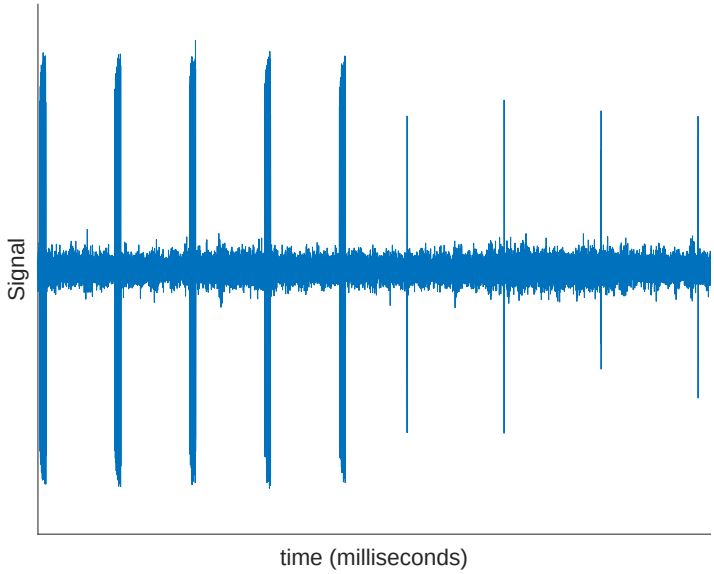

Figure 7.2: Recorded signal pattern from the ground radar

In the application of this chapter, the localization is done real time at the place of the receiving antenna. A stable datalink between the ground and mobile stations can provide this information to the processor.

7.2.2. Signal Transmitter

In this research, a primary ground radar is used as transmitting antenna. This is an existing radar station, located in the center of the Netherlands. The radar system is owned and operated by Dutch Air Traffic control, and it is developed for use as a monostatic radar for air surveillance purposes. This means that the radar is not optimized for bistatic applications, but it is a functioning transmitter nonetheless[8]. A network of these radars exists and it is designed such that the radars cover the complete airspace.

The broadcast signal is recorded with the signal receiver, and results of that recording can be seen in Figure 7.2. Units are not listed on the axes in order to protect the frequency information, which is proprietary data. But it is given that the width of the x-axis is in the order of magnitude of milliseconds. In the Figure it can be seen that periodically a high amplitude is measured. The rest of the time the signal seems to have a constant level, which is the background noise.

This high amplitude corresponds to the operation of the transmitter, which emits frequent pulses. The intervals between the pulses are regular, and two types of pulses can be observed in Figure 7.2: short and long pulses. These are used to

Table 7.1: SDR Specifications

Parameter	Value
Length	11cm
Width	7.5cm
Height	2.5cm
Weight	400grams
Signal inputs	2
Signal outputs	2
Power supply	via USB

detect aircraft in short and long range, respectively.

Long pulses make it easier to detect reflections against the background noise, but they cannot be used in short range because the receiver antenna has to be turned off during transmission, as discussed in section 7.2.1 above. In a bistatic concept it is not necessary to turn off the receiver, so in this application we focus only on the long pulses. How this works is explained in Section 7.3.

7.2.3. Signal Receiver

For the hardware of the bistatic receiver a Software Defined Radio (SDR) is used, in combination with a laptop. The SDR is powered by the laptop via the USB connection, so the setup is mobile. The collection of the data is done by the SDR and the processing is done by the software on the laptop.

The SDR is small hardware which is constructed on a single circuit board, as seen in Figure 7.3. The specifications of the SDR are given in Table 7.1, thus the SDR is small and lightweight, and it is possible to use it in a mobile setup.

As can be seen in Table 7.1, this SDR has four antenna connections. These can be seen on the right hand side in Figure 7.3. Of these antennas, two can be used for transmission of radio signals and two for reception. Only one of these antenna connections will be used in this study.

The antenna used for the receiver is custom built for reception at the ground station carrier frequency. The antenna is omnidirectional, meaning that it can receive signals equally well from all directions in the horizontal plane. The antenna is connected to the SDR with a cable, which is kept short (25cm) in order to reduce signal loss of the analog signal in this cable.

7.3. Software

In this section the software of the laptop will be described, which is used to determine the locations of reflections measured by the bistatic hardware. The software toolkit used is introduced in section 7.3.1 and the principle of Matched Filtering is described in section 7.3.2. In section 7.3.4 the bistatic radar equation is used to find the location of reflections. Window Functions may be a solution to improve the results, these are introduced in section 7.3.3.

Figure 7.3: The Software Defined Radio used [image from nuand.com]

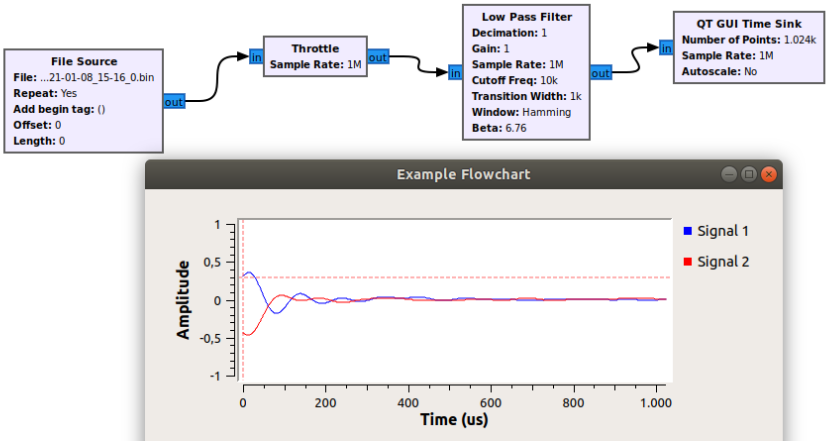

Figure 7.4: Example Flowchart and Execution window of GNU Radio: loading data, applying a low pass filter and plotting the results

7.3.1. Software Toolkit

The software application that is used is called GNU Radio[1], which is an open-source software development toolkit focused on signal processing. The software comes with a graphical interface which can be used to make block chains of functions which can process a data stream in real time. A simple example of such a flowchart is given in Figure 7.4.

Extensions for GNU Radio exist with which an SDR can be controlled and operated. The received data can be saved as a file for research and development purposes or it can be fed directly into the flowchart such that the data can be viewed in real time.

GNU Radio can be extended by the user who can add custom code to the software. With this feature, connections to external data sources can be implemented in the software. Such connections can be to a gps reader or to a display system that plots the results.

7.3.2. Matched Filtering

As described in section 7.2.2, the primary radar transmits long pulses to the air. These pulses blend in with the background noise, since their strength reduces over distance. In order to differentiate the signal from the noise, a Matched Filter can be used [9, 10].

A Matched Filter is matched to the signal that needs to be discerned from the background. The Filter uses a template and gives a strong output when that signal is received [11]. The output for a Matched Filter on a sampled system is a convolution, which can be mathematically represented by:

[1]GNU Radio can be found at https://www.gnuradio.org/

$$y(t) = (s * h)(t) = \int s(t-\tau) \cdot h(\tau) d\tau \tag{7.1}$$

In equation 7.1, the Matched Filter output of the signal $s(t)$ at time t is given by $y(t)$. The symbol h denotes the Matched Filter. The Matched Filter remains constant during the measurement, whereas the signal $s(t)$ is changing. If the signal contains data that is similar to the matched filter, $s(t)$ and h will be similar and $y(t)$ will be high. Therefore a Matched Filter can be used to detect a long but weak signal against background noise.

The Matched Filter h has a finite size of N elements and will be applied on the digital signal. Equation 7.1 can be discretized as follows:

$$y[n] = (s * h)[n] = \sum_{m=-\frac{1}{2}N}^{\frac{1}{2}N} s[n-m] \cdot h[m] \tag{7.2}$$

In the discretization in equations 7.1 and 7.2, the ratio between the sample number n and the time t is the sample rate of the experiment.

The operation of a Matched Filter is demonstrated on a real recorded signal with background noise, but first a simulated signal under perfect conditions is used. The signal pulse that is simulated is $0.1ms$ long, and let its frequency be linearly increasing in that time:

$$f(t) = f_0 + \frac{df}{dt} \cdot t \tag{7.3}$$

$$f(t) = 5.0MHz - 7.0GHz/sec \cdot t \tag{7.4}$$

This means that the phase p of the simulated signal a can be computed and that the complex representation of a is:

$$p(t) = \int 2\pi f(t) dt \tag{7.5}$$

$$p(t) = 2\pi(5.0 * 10^6 t - \frac{1}{2} 7.0 * 10^9 t^2) \tag{7.6}$$

$$a(t) = e^{i \cdot p(t)} \tag{7.7}$$

And let the signal $s(t)$ consist of just this frequency with power 1 and nothing else, therefore a noiseless signal is simulated:

$$s(t) = \begin{cases} a(t) & 1e^{-4} > t > 2e^{-4} \\ 0 & otherwise \end{cases} \tag{7.8}$$

The Matched Filter $h[n]$ is the exact complex conjugate of the waveform:

$$h[n] = e^{i \cdot -p[n]} \tag{7.9}$$

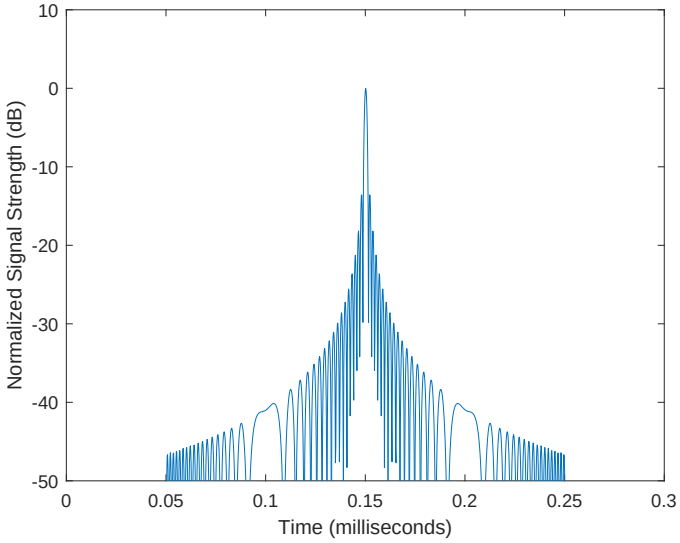

Figure 7.5: Result of applying the Matched Filter on the simulated noiseless pulse

The result of applying this Matched Filter $h[n]$ on this noiseless simulated signal $s[n]$ can be seen in Figure 7.5. It is seen that the blue line in Figure 7.5 has one peak value: this occurs at the moment when the signal is received. After this moment, the strength of the output fades away. The peak value occurs at $t = 0.15ms$, exactly at the middle of the pulse, which lasts from $t = 0.1ms$ to $t = 0.2ms$. So the Matched Filter can help to find exact timing of longer pulses as accurately as possible.

Now it is known that using a Matched Filter can help indicating the locations of pulses in the time domain. But in order to apply a Matched Filter on the signal from the ground radar it is required to know what waveform is transmitted. This information is proprietary so these details cannot be shared in publications. This has consequences for the applicability of bistatic radar: the transmitter waveform must be determined before the method can be applied.

Two strategies are suggested to obtain the waveform information, for the purposes to reproduce the results in this study. The first option is to collect this data from the organization that operates the ground radar and performs maintenance on it. For this study, the ground radar properties have been provided by Dutch Air Traffic Control.

The second option is to record the waveform with the receiver in a field experiment. The second option has as a disadvantage that multiple attempts of recording will be necessary in order to find the correct signal frequency. But when a successful recording is made, the recorded data can be used as a template for the Matched Filter, which will be more accurate than when a Matched Filter is based on the theoretical properties of waveform.

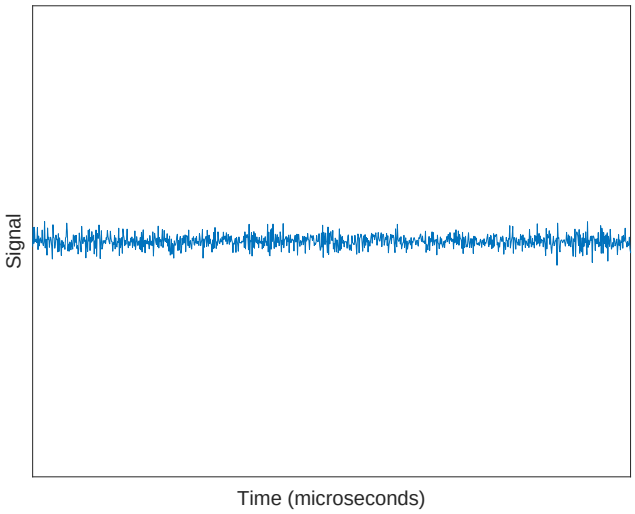

Figure 7.6: Raw signal as measured from the radar by the SDR, including background noise

Even though the waveform information cannot be shared, we illustrate the operation of the Matched Filter based on real recorded data, but the values from the axes are removed. The data is pictured in Figures 7.6 and 7.7. The original recorded signal is seen in Figure 7.6. No pulses are clearly apparent in the data, because the signal to noise ratio is not high enough. When this signal is convoluted with the proper Matched Filter, the locations of the pulse that are hidden in the signal will become clear, as seen in Figure 7.7.

7.3.3. Window Functions

After applying a Matched Filter, as described in section 7.3.2, the locations of reflections become apparent in the time domain representation of the signal as peaks rising above the noise floor. These peaks have the shape of the blue line in Figure 7.5, which is generated with a theoretical signal in perfect circumstances.

As can be seen in Figure 7.5, the sides of the peak are not vertical lines, but the Filter output reduces over time. If there were a second signal in Figure 7.5, a bit earlier or later but weaker in strength, it may not be visible because it is under the sidelobe of the big pulse.

This problem will always exist: if two signals arrive at the same time one may suppress the other. But the problem can be reduced by applying a Window Function on the Matched Filter [10, 12]. A Window Function is a mathematic formula that values a part of the Matched Filter over the rest. Many different window Functions exist [9], and their effects have been researched thoroughly. A well known Window Function is the Hann Filter, this Window Function is also used in this chapter.

The Hann Window Function is a function that reduces the values of the edges

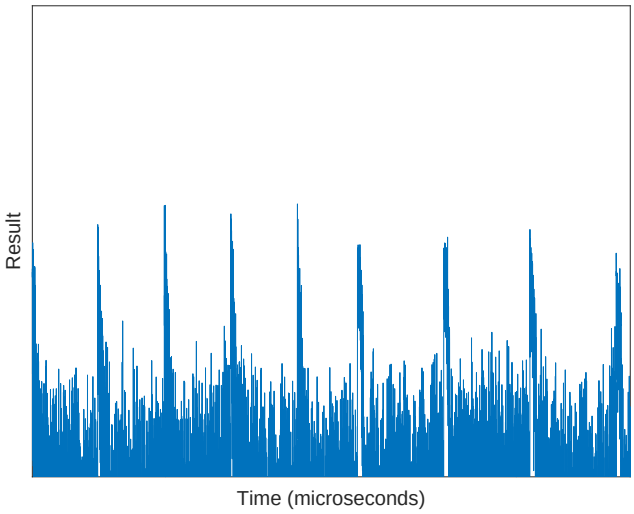

Figure 7.7: Applying the Matched Filter on raw signal reveals pulse locations

of the filter until they reach zero, while keeping the central values of the template close to their original values. The formula for a Hann window is as follows:

$$w[m] = \sin^2\left(\frac{\pi \cdot m}{N}\right) \tag{7.10}$$

We can multiply the Hann Window with the Matched Filter, which changes the filter values, as seen in Figure 7.8. The signal output from equation 7.1 then becomes:

$$y[n] = \sum_{m=\frac{1}{2}N}^{\frac{1}{2}N} s[n-m] \cdot h[m] \cdot w[m] \tag{7.11}$$

As stated in the start of this section, the goal of using this Window Function is to reduce the strength of the sidelobes of the Matched Filter output from figure 7.5. To test this, a weak second pulse is added to the signal stream of Figure 7.5, with a small delay of 0.02ms. The simulated signal is described as:

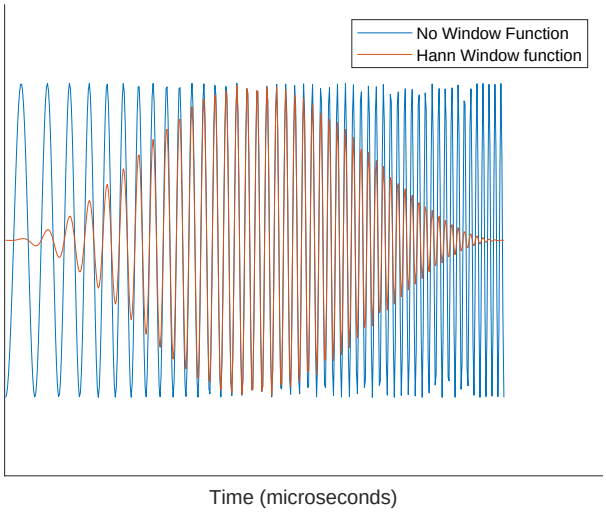

Figure 7.8: The same Matched Filter with and without Hann Window

$$s_1(t) = \begin{cases} a(t) & 1e^{-4} > t > 2e^{-4} \\ 0 & otherwise \end{cases} \tag{7.12}$$

$$s_2(t) = \begin{cases} a(t - 0.2e^{-4}) & 1.2e^{-4} > t > 2.2e^{-4} \\ 0 & otherwise \end{cases} \tag{7.13}$$

$$s(t) = s_1(t) + 0.01 \cdot s_2(t) \tag{7.14}$$

The results of Matched Filters with and without Hann window can be seen in Figure 7.9. It can be seen that the second pulse can only be distinguished from the first pulse if the Hann window is applied, since that window makes the response peak more narrow.

7.3.4. Localizing Reflections

After pulses have been detected in the radar signal (as explained in the previous section) they should be localized, so it becomes clear where they are originating from. In order to perform this computation, four parameters are required:

- The location of the radar receiver
- The location of the radar transmitter
- The direction of the transmitted signal

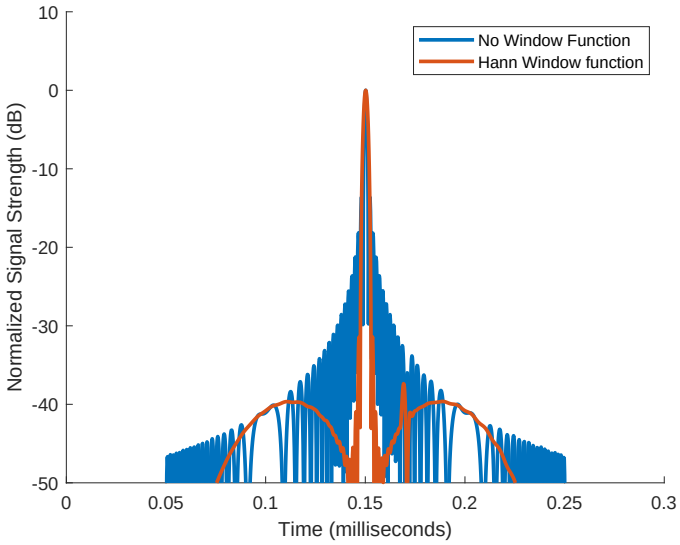

Figure 7.9: Only the Matched Filter with the Hann Window can observe the second peak

- The travel time of the signal

These parameters will help to solve the bistatic radar geometry equation and plot the location of the reflection on a 2d map. The location of the receiver can be known by taking a GPS receiver along with the test hardware. The radar transmitter is static, so its location never changes. The direction of the transmitted signal and the travel time may be communicated over a data link between the transmitter and receiver, such that the receiver always has up to date information.

Once these parameters are known, the location of a reflection can be determined in two dimensions by using the bistatic geometry equation, which is numbered equation 7.15, as found in [13]. The equation is based on the geometry as seen in Figure 7.10.

$$R_2 = \frac{(R_1 + R_2)^2 - L^2}{2(R_1 + R_2 + Lsin(a))} \tag{7.15}$$

Equation 7.15 looks complicated at first, but it is relatively easy to solve: L and a are known parameters, and $R_1 + R_2$ is the total distance travelled by the signal. This distance can be computed when the timing of the pulses is measured accurately, since radar signals always travel with the speed of light c, as indicated in equation 7.16.

$$R_1 + R_2 = L + dt \cdot c \tag{7.16}$$

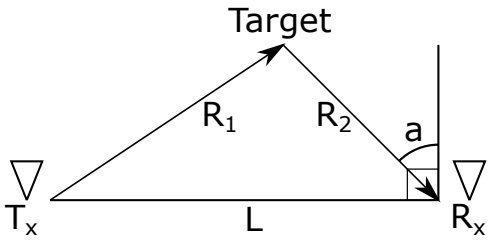

Figure 7.10: Bistatic Radar Geometry

7.4. Experiment

An experiment is developed in order to assess the performance of the hardware and software of the passive radar system, as described in the previous sections. The goal of this experiment is to quantify the performance of the bistatic radar setup and to compare its detection capacities to that of traditional transponder technology.

The experiment will focus on the detection of two kinds of obstacles. The first category is static obstacles, such as buildings and towers. The second category is dynamic obstacles, such as aircraft. These two categories will be treated as separate sections within Section 7.5.

For this experiment a ground radar of Dutch Air Traffic Control was used as bistatic transmitter. The specifications of this radar are provided to the researchers by Air Traffic Control, but it is not allowed to share these publicly.

The receiving end of the bistatic radar setup is placed on top of a viewpoint in a forest, located at a distance of about 12 kilometers from the ground radar. The receiver location was chosen because a line of sight is available between the two ends of the setup, and the location in the forest was expected to be relatively free of intervening signals. An image of the viewpoint can be seen in Figure 7.11.

As noted before, the experiment results will focus on static obstacles and dynamic obstacles. The position of static obstacles can be verified with a map, but dynamic obstacles need to be logged.

During the experiment, a test aircraft was also flying over the test zone. The aircraft carried a transponder and a GPS tracker on board, with which its trajectory was logged. The performance of the bistatic radar can be verified in that way. A picture of the aircraft can be seen in Figure 7.12.

During the experiment, the radio signals were recorded for a period of 40 seconds, in which 9 full observations can be made. The recordings are stored and used for processing after the experiment.

7.5. Results

In this section the results of the experiment are presented, focusing both on the performance of the bistatic radar and the transponder technology. The radar output is discussed in general in the first part of this section, subsection 7.5.1, and the results for static and dynamic obstacles are discussed in subsections 7.5.2 and 7.5.3.

Figure 7.11: The viewpoint for the receiver location. The tower is higher than the treetops.

Figure 7.12: The target aircraft used in the experiment

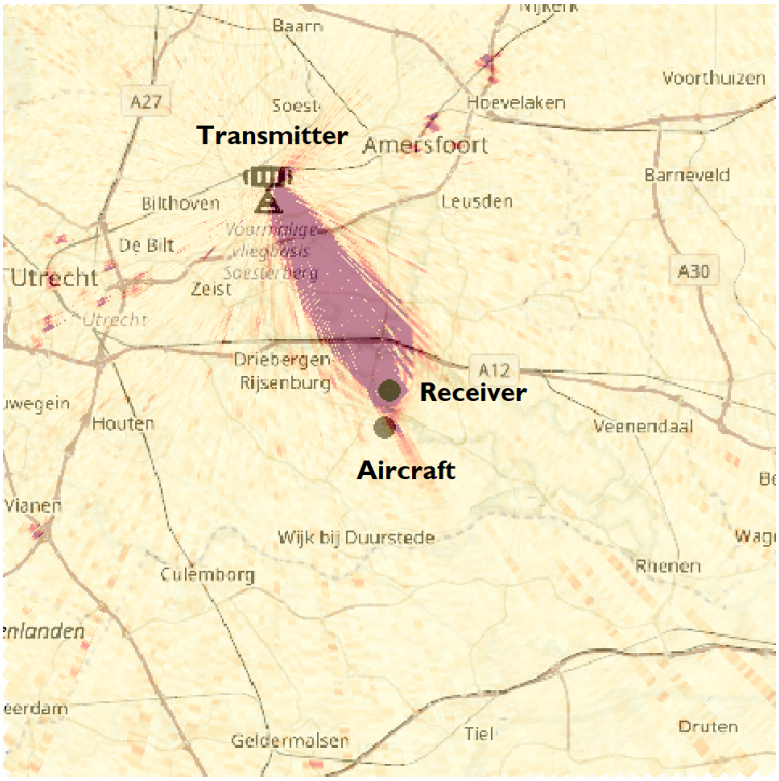

Figure 7.13: Results for the bistatic radar setup plotted on a map. Maroon regions are locations with high signal strength, yellow indicates low signal.

7.5.1. General Bistatic Radar Output

Multiple measurements were performed during the experiment, which are used to evaluate the performance of the bistatic radar. A typical example of one measurement is seen in Figure 7.13. Several elements in this figure shall be highlighted below.

It is seen that Figure 7.13 consists of a background map, on which cities and roads are indicated. Three elements are located explicitly on the map: the locations of the ground radar, the mobile receiver station and the aircraft. The location of the ground radar is given, the receiver location is known. The aircraft location is recorded with the transponder technology, and indicated on the map.

A colored overlay is present, on which the signal reception for each location is indicated by color: yellow indicates a weak signal reception and maroon indicates strong signals.

At first glance it is seen that a very strong reception is present in the area in between the transmitter and receiver. This strong region is always present in the results, and will be discussed explicitly in section 7.6. The rest of the map is mostly yellow, except several dark spots on the overlay, which change during the recording.

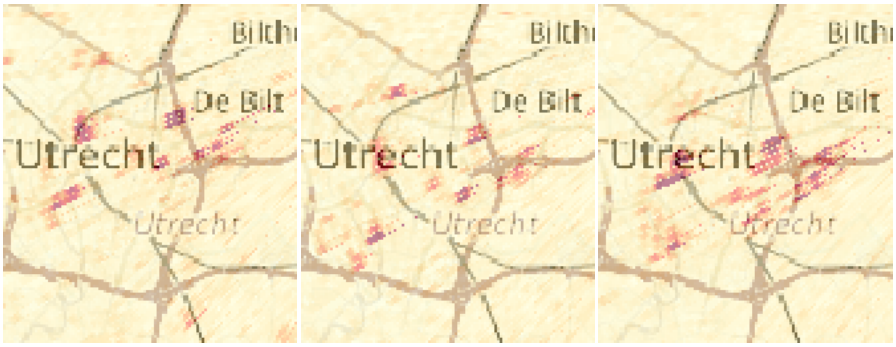

Figure 7.14: Visual result of three measurements of static reflections of Utrecht

These are considered reflections of obstacles.

7.5.2. Static Obstacles

The majority of the map is bright yellow, indicating that no strong signals are coming from there. The test was conducted on the free standing tower, and the local surroundings were all forests. This indicates that no reflection from the trees is observed, not even the trees at close distance. This may be because the wood is not a good radar reflector, or that the radar is aimed above the forests, so not many signals are reflected there.

Contrary to the forests, there are groups of strong signals above urban areas. Three images of reflections of urban areas can be seen in Figure 7.14. When comparing the locations of these reflections to satellite images, high rise buildings can typically be found at the locations of the strong reflections. These high buildings can be churches, apartment complexes and office buildings. Whilst aircraft carry transponders, the buildings cannot be detected by transponder technology. It must be noted that the locations of the reflections shift a little in Figure 7.14, where all reflections appear to be moving to the north or south together.

For the experiment, it is chosen to focus on 5 (clusters) of reflections that can be observed in Figure 7.13. These are all coming from urban areas in the surroundings of the environment. For each of the 9 observations, it is counted how often the clusters are observed in the results map. Also, the approximate values for R_1 and R_2 are given. These results are shown in Table 7.2.

7.5.3. Dynamic Obstacles

In Figure 7.13 it can be seen that a strong signal is received from the area where the aircraft is flying. The radar reflections and the transponder technology both indicate that an aircraft is present, although the exact location differs.

During the experiment, it has been counted how often the reflections from the aircraft are observed. Since the aircraft is logged during the flight, its R_1 and R_2 values can be computed at the times of observations. These results can be found in Table 7.3. In the Table, it is seen that the aircraft is 'possibly' observed three

Table 7.2: Observation Count of Static Obstacles

Reflection	Times Observed	Times Missed	Hit Percentage	R_1 (km)	R_2 (km)
Geldermalsen	7	2	78%	30.6	20.7
Vianen	9	0	100%	22.0	19.6
Utrecht	9	0	100%	9.4	14.7
Amersfoort	9	0	100%	8.8	14.3
Hoevelaken	9	0	100%	12.3	16.8

Table 7.3: Observation Count of Aircraft

Reflection	Observed?	R_1 (km)	R_2 (km)
1	Possible	11.8	1.1
2	Possible	12.0	1.3
3	Possible	12.2	1.5
4	No	12.4	1.7
5	No	12.6	1.9
6	No	12.8	2.1
7	No	13.0	2.3
8	No	13.2	2.4
9	No	13.3	2.6

times. These times, the reflections on the map looked very similar to the one from Figure 7.13. Signals like this can very well originate from reflections of the aircraft, but it cannot be said with absolute certainty.

7.6. Discussion

The results of the bistatic radar experiment are discussed in this chapter. It consists of three sections: in the first section, the focus will be on the grand maroon area in the center of Figure 7.13. The second and third sections will go into detail about the detection of static and dynamic obstacles in the experiment. In these sections the obstacle detection capacities of the radar setup will also be compared to those of transponder technology. The final section contains a discussion about the application of well known radar processing operations, such as Moving Target Indication, on this bistatic radar setup.

7.6.1. Central Area

As announced in section 7.5, special attention should be paid to the area of strong reception in between the receiver and transmitter. This area is always present, meaning that there is no difference whether objects are in it or not, so obstacles are not visible in this area. This is logical: when the receiver is listening in that direction it will primarily record the direct path from the ground radar, which is very

strong.

Any reflections from within this central area will arrive at the receiver station at around the same time, meaning that they fall in the shadow of the primary pulse. This is a inherent property of a bistatic radar setup. The area of this region may be reduced if the receiver is shielded from the direct signal such that it is weaker, or by using a directional antenna for the receiver.

7.6.2. Static Obstacles

During the experiment, reflections of high buildings in urban environments were seen. These reflections were consistently observed every time the ground radar illuminated them and they appeared on the same places. Minor changes in the location places were observed, which is believed to be a rotational shift around the transmitter radar. If the datalink between the transmitter and receiver stations is more stable, this variation can be reduced.

All reflections of these buildings were observed repeatedly. Only 1 out of the 5 observed clusters has not been consistent, but this also has been the one the furthest away from the test location: the R_2 distance was 20 kilometers. It is logical that the performance of radar is reduced over distance, and a distance of 20 kilometers is more than enough time to take action for any General Aviation pilot, who usually needs several minutes to cover this distance.

The high rise buildings that the bistatic radar observed are usually not equipped with transponder technology of any kind, so they cannot be observed by other technological measures currently. Equipping all buildings with transponders is expensive and therefore an unlikely solution. Another solution can be to store locations of objects in a database, but that introduces a dependency on the accuracy and completeness of this database.

7.6.3. Dynamic Obstacles

The bistatic radar setup was also used to observe an aircraft flying over the receiver location. Other than the static obstacles, this aircraft was relatively close to the receiving antenna: during the tests the distance to the aircraft varied between 1 and 3 kilometers.

Despite this close range, the aircraft was not consistently observed. Three times out of nine, a reflection on the map was seen that could indicate a reflection of the aircraft, but these reflections have also been uncertain: it is possible that they were reflections from the aircraft, but they could also have been other spurious signals. These three reflections were also the cases when the aircraft was closest to the receiver antenna.

A possible explanation is that the aircraft was flying underneath the radar beam, but it is remarkable that the buildings on the ground were still visible. Another cause can be that the aircraft which was used was small and had a poor radar reflection. The distance between aircraft and antenna was also small and that would have made the signal stronger. A third explanation is that the Doppler effect caused by the aircraft velocity has distorted the signal to such an extent that it became unrecognisable by the Matched Filter. These explanations need to be investigated

in future research.

Comparing this to transponder based obstacle detection, it can be stated that the bistatic radar setup is not as reliable as transponder detection. However, transponder technology may not be available since it is not mandatory in General Aviation. That is not a problem for the bistatic radar, which can detect uncooperative targets - the signal from the ground radar is designed to detect those aircraft. And the ground radar network of Air Traffic Control is designed to provide coverage over the entire airspace so availability of bistatic radar signals is high.

At the moment, the improvement in availability of the detection is nullified by the reliability issue of the bistatic radar for dynamic targets. But bistatic radar sensing is independent and does not interfere with any other signals. Therefore it can still serve as an extra safety method on top of regular means of safety.

7.6.4. Other Radar Processing Operations

Many different algorithms and methods are developed for use in traditional monostatic radar sensing. This section contains discussion about three of these, and about the question whether they can be applied in this bistatic radar setup.

Moving Target Indication

Moving Target Indication (MTI) can be performed when the transmitter broadcasts several consecutive pulses [2, 14, 15]. The recorded signals from these pulses can be subtracted from each other. The principle of destructive interference will ensure that the signals that are identical in all recordings (from unchanging therefore static obstacles) are nullified and that only moving reflections remain.

Since the Air Traffic Control radar is developed for MTI purposes, the emitted signal is suitable for MTI processing. In order to do MTI accurately, the pulse repetition frequency (PRF) of the ground radar needs to be known. This is not a problem, since it was already required to know the waveform specifications of the ground radar.

But if the receiver is used on board of an aircraft, this will distort the signals too since the aircraft itself is moving. The effect of MTI will be reduced severely in this case. It may be possible to compute the expected results from static obstacles based on the conflict geometry and aircraft velocity, which future research can investigate.

Constant False Alarm Rate

Constant False Alarm Rate (CFAR) algorithms are adaptive algorithms that are widely used in radar processing in order to find peak value locations in a stream of numbers [2, 16]. This is important in order for the computer to discern strong signals from the background noise and to find the origin of possible hazards for the pilot.

These algorithms adapt to the processed data stream. It can therefore be expected that CFAR based detection of targets will work also in a bistatic radar setup, even when the receiver is located far from the transmitter. Future projects will aim to implement CFAR in the receiver.

Moving Target Detection

In Moving Target Detection (MTD), the radar reflections can be compared to a known reflection map around the monostatic radar [14, 17]. This map can be recorded at any time when it is known that no targets of interest are present in the radar field of view. This map will then only contain objects that are not of interest for the user. During operation, the recorded radar map can be subtracted from the current results, filtering out all uninteresting reflections.

However, it is known that the reflection strength of an obstacle is influenced by the angle with which the radar beam is reflected. Since the bistatic radar setup is developed with the idea of having a mobile receiver, this means that the background map will be different for all positions in which the receiver may be located. If the receiver is indeed going to be used on a moving platform, constructing a background map will be impossible.

7.7. Conclusion

The radar sensing technology in the previous chapters focused on hardware that transmits its own signal, of which the reflections are received on the same location. As opposed to this principle, this chapter focuses on using a bistatic radar constellation, in which the transmitter and receiver antennas are separated by a distance of several kilometers.

The transmitting part of the setup is the ground radar from Air Traffic Control. The receiving station is implemented on a Single Board Computer, using a BladeRF as the Software Defined Radio (SDR). The setup is lightweight and runs on battery power, such that it can be made as a mobile station.

Real time knowledge about the transmitter station is required in order to work. Various signal processing techniques are applied in order to recognize incoming signals with respect to background noise, and to localize their origins.

The hardware is tested in an experiment where the SDR is taken to a viewpoint above a forest, which is located at a distance of about 12 kilometers away from the ground radar. It is found that the system can consistently detect radar reflections from buildings in several cities around the test location, which are found to be up to 20 kilometers away from the test setup.

An aircraft was also included in the experiment, to assess the performance of the bistatic radar on dynamic targets. It was found that the SDR had difficulty detecting this object. The detection of the aircraft was inconclusive and not reliable. Possible explanations include the relatively small size of the aircraft, and signal deformation due to the Doppler effect. Future research will try to answer these questions.

The reflections from the buildings imply that the bistatic principle is working correctly and that it can be used to observe objects, even uncooperative ones, which is the main strength of sensing by bistatic radar. This technology can also observe static obstacles such as buildings and towers. The hardware is also compact and lightweight, so mobile applications are possible. This means that the principle of bistatic radar may be used by a pilot to detect obstacles in situations of poor visibility.

Comparing that to transponder technology, such as ADS-B and Flarm, it is found

that bistatic radar sensing is always available when a ground station is present. Transponder technology is not always available to sense obstacles: aircraft do not always carry transponders, and static obstacles are hardly ever equipped with such hardware. However, the big benefit in availability is nullified by the poor reliability in detecting aircraft.

So with the current state of hardware, the sensing of aircraft is not reliable enough to be used in practice. This will be improved when more accurate antennas become available or the system parameters of SDRs are improved. Alternatively, new software methods for signal processing can improve the quality of the detections. When this happens, bistatic radar sensing will provide a user significant benefits when compared to object detection based on transponders.

References

[1] P. Bezoušek and V. Schejbal, *Bistatic and multistatic radar systems,* Radioengineering **17**, 53 (2008).

[2] M. I. Skolnik, *Radar Handbook*, Vol. 58 (McGraw-Hill Education, 2008) pp. 53–79.

[3] M. I. Skolnik, *An Analysis of Bistatic Radar,* IRE Transactions on Aerospace and Navigational Electronics **ANE-8**, 19 (1961).

[4] J. I. Glaser, *Some Results in the Bistatic Radar Cross Section (RCS) of Complex Objects,* Proceedings of the IEEE **77**, 639 (1989).

[5] R. J. Burkholder, I. J. Gupta, and J. T. Johnson, *Comparison of Monostatic and Bistatic Radar Images,* IEEE Antennas and Propagation Magazine **45**, 41 (2003).

[6] M. Ritchie, F. Fioranelli, H. Griffiths, and B. Torvik, *Monostatic and bistatic radar measurements of birds and micro-drone,* in *IEEE Radar Conference* (2016) pp. 6–10.

[7] M. Weiß, *Synchronisation of bistatic radar systems,* in *International Geoscience and Remote Sensing Symposium (IGARSS)*, Vol. 1 (2004) pp. 1750–1753.

[8] J. Brown, K. Woodbridge, H. Griffiths, A. Stove, and S. Watts, *Passive bistatic radar experiments from an airborne platform,* IEEE Aerospace and Electronic Systems Magazine **27**, 50 (2012).

[9] C. Kumar, *Development of Efficient Radar Pulse Compression Technique for Frequency Modulated Pulses*, Ph.D. thesis, National Institute of Technology Rourkela (2014).

[10] S. J. Orfanidis, *IEEE Transactions on Communications*, Vol. 20-5 (Pearson Education Inc, 2004) pp. 1046–1047.

[11] P. V. Villeneuve, H. A. Fry, J. P. Theiler, W. B. Clodius, B. W. Smith, and A. D. Stocker, *Improved Matched-Filter Detection Techniques,* in *Proceedings SPIE*, Vol. 3753 (1999) pp. 278–285.

[12] D. Koks, *How to Create and Manipulate Radar Range-Doppler Plots*, Tech. Rep. (Defence Science and Technology Organisation, Edinburgh, 2014).

[13] H. D. Griffiths, *From a different perspective: Principles, practice and potential of bistatic radar,* in *Proceedings of the International Conference on Radar*, Vol. 1 (2003) pp. 1–7.

[14] C. C. Hang, W. C. Ming, L. Weixian, and J. S. Fu, *Radar MTI/MTD Implementation and Performance,* in *2nd International Conference on Microwave and Millimeter Wave Technology Proceedings* (2000) pp. 674–678.

[15] K. A. Gallagher, R. M. Narayanan, G. J. Mazzaro, K. I. Ranney, A. F. Martone, and K. D. Sherbondy, *Moving target indication with non-linear radar,* in *IEEE National Radar Conference - Proceedings*, June (IEEE, 2015) pp. 1428–1433.

[16] R. Nitzberg, *Clutter Map CFAR Analysis,* IEEE Transactions on Aerospace and Electronic Systems **AES-22**, 419 (1986).

[17] T. S. Perry, *In search of the future of Air Traffic Control,* IEEE Spectrum **34**, 18 (1997).

8

Conclusion

This chapter concludes the dissertation. The goal of using radar sensing in General Aviation is repeated in the first section, as well as the requirements that the radar sensor must comply to. In the middle sections, the conclusions from the previous chapters are summarized. The final sections of this chapter go in detail on the promise of independent sensing in aviation and how the technologies from this dissertation can be applied in industry.

8.1. Radar Sensing Requirements

Many flights in General Aviation are performed under Visual Flight Rules, in which the pilot is responsible for preventing collisions. Using eyesight is the pilot's only independent method to survey the area around the aircraft, but there are limitations to human vision which can be dangerous in aviation if no other safety measures are taken. Another opportunity for the detection of hazards can be to use microwave sensing techniques, this method of observation is independent of the other target as well.

This dissertation revolves around radar sensing techniques that can be applied in General Aviation, which must comply to several specific requirements. The techniques should provide unambiguous warnings for the pilot in case of hazardous situations, such that the pilot can take action to resolve the danger. The acquired results must be accurate and reliable. The radar should not provide a false sense of safety, so it must not overlook obstacles within a specified range. Also, the results must be obtained on board of a GA aircraft, which poses restrictions on price, weight and power consumption. The computations by the sensing techniques must be able to be performed real time.

8.2. Modelling a Microwave Sensor

Many experiments are required in the process of developing radar solutions, but flight tests are costly in both financial and logistical aspects. Therefore, first a model

was developed to simulate microwave output on a computer, such that experiments can be performed on a computer instead of in flight tests. The Python code of this model was provided in this dissertation.

The developed simulator has proven to be suitable for simulating the response of an active radar. This radar model broadcast its own radar waves, and listened to their reflections as well. The waveform simulated was frequency modulated on continuous waves - a prototype radar with these specifications was available for experiments.

The model output has been compared to the output of the actual radar prototype and it was seen that the patterns observed in the radar output were also visible in the real collected data. But some unwanted data, such as the presence of spurs and background noise, were clearly visible in the actual radar output too, but they were absent in the simulator.

This means that this simulation of a microwave system can be used for development of various sensing techniques and methods without flying, but also that verification of the methods by using flight tests remains necessary. Future research to the presence of spurs in antenna systems may help to further increase the model, reducing the dependency on flight tests further.

8.3. Detection of Objects

In chapter 3, research was presented towards the possibility of actually building a portable primary radar for General Aviation, of which the goal was to bring it on board of an aircraft for purposes of 'detect and avoid'. Such a system has to be affordable, small and have a low power consumption, and the hardware tested in this chapter matches those requirements.

A test was performed with an aircraft flying over the radar, which proved to be detectable in the radar image for a range up to $3km$. The aircraft was tracked with an on-board GPS for a flyover at closer distance and the radar was able to detect the aircraft autonomously and to determine its location with an accuracy of on average $46m$.

The direction of the incoming signals could be determined within 2 degrees horizontally, and 3 degrees vertically. If the aircraft was tracked, low-pass filters could be applied to filter out the high-frequency noise and increase the accuracy of the three dimensional position estimates. Expanding the number of antennas beyond the four used in this research could also improve the radar results further.

It was found that the deployment of portable primary radars can increase situational awareness around the radar system. Future research is required to develop both the hardware and software for aviation purposes, such as in-air use and separation of ground reflections.

8.4. Tracking of Objects

In chapter 4, a novel method for tracking objects in images was presented. The method was optimized for use in FMCW radar images, which are fundamentally different from traditional visual images. The method makes use of the radar specific

properties, such as the Doppler effect, with which accurate target predictions can be made. A simulation experiment is set up to assess the performance of the algorithm in dense General Aviation circumstances, and the results are investigated.

It is found that the proposed method outperforms a traditional object tracking algorithm. Often, a traditional method is not able to connect segments of observations to each other when the observations are aliased to the other side of the radar image or at close distance. The new algorithm is almost always able to make these connections, but one case was found where the new algorithm misconcluded that a series of observations consisted of two tracks instead of one.

Additionally, the accuracy of the proposed algorithm was tested. It was found that the new algorithm is better in predicting the progression of a track than standard optical imagery, and that systems using the new algorithm may have a higher tracking capacity than traditional algorithms applied to FMCW radar images.

In conclusion, the proposed tracking algorithm improved the internal Kalman model of the observed tracks to include aliasing and the relation between distance and radial velocity. It is found that this is an important improvement for the object tracking in FMCW radar images. This new model may be combined with existing and upcoming research on the quality and the assignment of observations.

8.5. Estimation of Flight State

In chapter 5 the radar prototype was phyisically brought on board of an aircraft for the first time. Results from the simulation algorithms from chapter 2 indicated that ground reflections would be clearly visible in lower segments of the airspace. These segments are typically where General Aviation flights take place, so the reflections will always be present in on-board radar images.

It was investigated whether these ground reflections could be used to determine the altitude and velocity of the aircraft, using a new algorithm for this radar type, which was presented in this chapter. The system was tested in a local flight. It is concluded that the velocity estimates of the radar can approach the quality of those of GPS navigation, if proper filtering techniques are applied.

It was found that the radar could provide altitude information without the need for calibration, but the GPS needed to be calibrated to the runway height. Also, the radar measured the height above the terrain, including tree heights and landscape shapes. This information may be absent or unreliable in a database that is used for GPS navigation. However, the GPS height results are still more accurate than those of the radar. This difference will be reduced by the application of better filtering techniques and more accurate hardware.

The simulation tests indicated that the algorithm performs best above flat terrain. The landscape data of the flight test location are compared to the data of the entire European landscape, and it can be expected that the flight test results will improve if the experiment was performed at another location anywhere in 33.4% of Europe. For the other 66.6% of the landscape, it is unknown where the state estimation method can work and where it will malfunction. Further flight tests above varying landscapes can help indicate the performance envelope of the method.

If the radar sensor is developed further, and the quality of hardware and soft-

ware is improved with respect to the prototype, this strategy to find flight state information can become a solution for independent state determination with respect to the local environment around the aircraft.

8.6. Verification of Position Information

In chapter 6 the radar was tested again in flight, but this time the radar was not oriented to the front but to the side of the aircraft. It was found that the radar reflections showed patterns that visually resembled those of the landscape below the aircraft, when displayed as an image. It was researched whether these radar images could be used to verify the navigation information given by GPS.

Fifteen different methods were tested to process the images and to compare them to local maps. Two experiments were performed in order to evaluate these methods. In the first experiment, all 15 methods were evaluated on a few flight points. In the second experiment, the three methods that gave the best results were evaluated further in a more extensive test.

It was found that a method based on Ridge Operators and one based on Entropy Detection performed exceptionally well. The Ridge Operator algorithm was slightly better, but no definitive verdict can be given based on this study alone.

Both of these algorithms were able to validate the location of GPS, even when provided with 300 similar alternatives that were close around the GPS location. Errors were found when the aircraft was making a turn, thereby aiming the radar away from the ground.

It is concluded that observations of ground reflections from airborne radars can be used to validate the functioning of a GPS, as long as the radar can observe features on the ground that can be correlated to that on a map of the environment. The use of processing algorithms to extract features from the radar data is crucial for this application.

8.7. Detection of Objects using a Passive Radar

As an alternative to the radar sensing principle from the previous chapters, chapter 7 focuses on using a bistatic radar constellation, in which the transmitter and receiver antennas are separated by a distance of several kilometers.

The transmitting part of the setup is the ground radar from Air Traffic Control. The receiving station is implemented on a Single Board Computer, using a BladeRF Software Defined Radio (SDR). The setup is lightweight and runs on battery power, such that it can be made into a mobile station.

Real time knowledge about the transmitter station is required in order to work. Various signal processing techniques are applied in order to recognize incoming signals with respect to background noise, and to localize their origins.

The hardware is tested in an experiment where the SDR is taken to a viewpoint above a forest, which is located at a distance of about 12 kilometers away from the ground radar. It is found that the system can consistently detect radar reflections from buildings in several cities around the test location, which are found up to 20 kilometers away from the test setup.

An aircraft was also included in the experiment, to assess the performance of the bistatic radar on dynamic targets. It was found that the SDR had difficulty detecting this object. The detection of the aircraft was inconclusive and not reliable. Possible explanations include the relatively small size of the aircraft, and signal deformation due to the Doppler effect. Future research will try to answer these questions.

The reflections from the buildings imply that the bistatic principle is working correctly and that it can be used to observe objects, even uncooperative ones, which is the main strength of sensing by bistatic radar. This technology can also observe static obstacles such as buildings and towers. The hardware is also compact and lightweight, so mobile applications are possible. This means that the principle of a bistatic radar may be used by a pilot to detect obstacles in situations of poor visibility.

The comparison with transponder technology, such as ADS-B and Flarm, is made. It is found that bistatic radar sensing is always available as long as a ground station is present, but transponder technology is not always available to sense obstacles: aircraft do not always carry transponders, and static obstacles are hardly ever equipped with such hardware. However, the poor reliability in detecting aircraft still provides challenges for the bistatic radar system, in which the transponders perform better.

So with the current state of hardware, the sensing of aircraft is not yet sufficiently reliable to be used in practice. Developments in hardware and software may help to increase the performance of bistatic radar sensing. If that happens, the accuracy and reliability of this method of sensing may be improved and SDR sensing can outperform transponder technology for the purpose of obstacle detection.

8.8. Radar Sensing as Independent Solution

This dissertation focuses on the application of microwave sensing technology to assist pilots in General Aviation in their 'detect and avoid' tasks. The technology should never provide a pilot with a false sense of safety, so they must detect any obstacles that are relevant for the pilot. This detection must be independent of technology that may not be present on all obstacles, so transponder technology is not a final solution for the problem (but it can still be a good additional safety net for a pilot).

The independent nature of radar sensing has been demonstrated extensively in this dissertation. Reflections have been observed of aircraft, buildings and trees: these are all obstacles that can be relevant for a pilot but that may not carry transponders. It is demonstrated that tracking of these objects is possible, so radar technology can be used to closely monitor the movements of objects in the vicinity of the radar through time.

The reflections of the ground allow it to be used to infer the pilot's position with respect to the ground. The altitude, heading and latitude/longitude coordinates have been determined by radar sensing in this dissertation. This can also be achieved by GPS navigation, but this introduces a dependency on the accuracy of the GPS landscape model. This can be coped with by calibration on the ground, but this is only a local solution.

It can be concluded that microwave sensing technology has serious potential as a support system for pilots in General Aviation, because it is an independent method of observation which can be automated, and it is not influenced by poor visibility conditions.

Similar considerations have of course been made in the selection of microwave sensors for self driving cars as they are being developed in the present day. But several important differences exist between aviation and road traffic (with respect to the sensors): the distances over which targets must be observed in aviation are larger than those in road traffic. Also, most hazards in road traffic will approach the vehicle over a more or less flat plane, but hazards in general aviation can come from three dimensions.

Despite the work done in this thesis, there is still much more work to be done before technology from self driving cars can be applied on aircraft. This is also supported by the conclusions from all of the chapters in this dissertation, which frequently state that more work should be done in order to further optimize the detection algorithms. Even though much of this research can be done in simulated experiments, as concluded in chapter 2, flight tests will remain necessary because radar spurs can be present in the actual hardware output.

8.9. Differences Active and Passive Radar

Two different kinds of microwave sensing technologies are inspected in this dissertation. In one of the two, the radar consists of both a transmitter and a receiver at the same location. For the second technology, only a receiver antenna is required, since it makes use of signals from other transmitters, being the Air Traffic Control ground radar. These two technologies are respectively referred to as active and passive radar sensing, since the latter does not actively transmit any signal.

8.9.1. Applying the Sensor in Industry

When these technologies are brought to the market in the future, it is foreseen that active sensing might give more difficulties than passive sensing in terms of licensing. Since licenses are required for transmission on specific frequencies, each transmitter should have a license to operate in the designed spectrum. Since these licenses are determined by national governments and many General Aviation aircraft perform international flights, this can be an extra difficulty. A solution could be to use openly available frequencies, but these can freely be used by anybody, so this comes with a risk that the signal gets hindered by somebody else.

The results obtained by the active and passive sensors in this dissertation differ in dimensionality: the active radar sensing resulted in three-dimensional localization estimates, but the passive radar could only determine a signal location in two dimensions. However, if the passive sensor would be equipped with multiple antennas, the same direction of arrival estimate algorithm could be used that was also used for the active radar.

Adding more antennas will go at the cost of miniaturization. In order to be used in General Aviation, the final hardware should be as compact and lightweight as

possible, and its power consumption should be low too. Adding more antennas makes a system more complicated and heavier, which makes it less suitable for use in General Aviation. Comparing the active and passive radar systems, the passive system will always be more suitable for miniaturization, since it does not require to transmit its own signal, saving on extra antenna hardware and power. The effects on the price of the hardware are similar.

8.9.2. Detection of Objects

For the detection of objects, the active radar has shown better results than the passive radar. The active radar has clearly observed aircraft in its vicinity with an accuracy of several meters (as demonstrated in chapter 3). The passive radar had difficulty in recognizing an aircraft in the experiment performed with it.

Comparing the detection information, it is seen that the active system can detect range and Doppler information, whereas the passive system can only detect range information. However, the passive system could detect buildings located 20 kilometers away from the sensor, this is much further than what is possible with the active radar system, that limits its range axis to 5 kilometers.

Another question is where the systems can detect obstacles. The active system can detect obstacles within its field of view. The radar was designed to have a wide aperture, but that still leaves a large area that is not surveyed by the radar. The passive radar was able to observe in 360 degrees, using only a simple antenna. There was a blind region in between the receiver and the ATC radar, where targets could not be observed. Both of the radar technologies have blind regions in which objects can remain undetected.

There are potential solutions possible, which are different for the two techniques. For the active system, a user could use multiple sensors to survey the zone around the aircraft. For the passive system, the solution could be to make use of different transmitters which are located on different locations. Depending on the application, a user can have a preference for either active or passive radar sensing. It can also be possible to accept a blind region, as long as the end user's requirements are not violated.

8.9.3. Worldwide Implementation

In this final section, the possibilities of worldwide implementation are discussed for the active and passive radar system. No problems are foreseen for the active radar system, since all technology is enclosed together at the aircraft. The active radar principle can work anywhere.

Another issue for worldwide implementation is the presence of transmitter stations for the passive radar. Indeed, the radar can observe targets independently of the target, but it is obviously dependent on the vicinity of transmitter stations such as those used by Air Traffic Control. Also, the passive radar system needs to have a database with the frequency and location information of all possible transmitters, otherwise it is not possible to perform object detection. Not all transmitters will be suitable for using as bistatic radar, and the operators may not be prepared to share the specific information. As there are also areas without primary radar coverage

(shielded behind mountains or in remote areas), worldwide implementation of a passive radar system seems unlikely.

Acknowledgements

It's been about seven years since I decided to start on this PhD trajectory. This was a long time which consisted of many memorable moments with many different people, filled with love and support. As proud as I am of the result of this PhD programme, so am I thankful to all the people who contributed to it, in one way or another.

First of all, I want to mention my family. I have had the incredible luck of growing up in an environment of unconditional love and support. You've shown me as much of the world that anyone could wish for, and given me the freedom to make my own choices in it. I can't express in words what an enormous wealth this is. Completing a PhD is the biggest scientific success of my life so far, and this truly is also your accomplishment. I am sure that with the immense power of your support, I could be successful anywhere.

During this PhD, I've had the pleasure of being supervised by an excellent professional duo, with whom I also worked together in most of my publications. Thank you for helping me in commenting on the draft versions of my papers over and over, and thank you for your tips and tricks in the process of publicizing them, as well as helping me find my motivation again after setbacks. Thank you for inviting me to do this PhD programme and for the continued supervision during the process.

This dissertation came into existence with the efforts of many professionals who went out of their way to accommodate my research. There are the people who built the radar prototype which was used in the first three journal publications that I made, and several test pilots were prepared to take my weird equipment on board of their flights. And of course the section secretary who forms the beating hart of all that is practical. I've learned from all your help that we can achieve more than what we think is possible, if we are prepared to go the extra mile to help each other.

Many of these professionals also work in the section of the university where I completed my PhD. There is a constant flow of colleagues arriving, and at the same time there are always people leaving. The colleagues made me feel welcome and appreciated from the first day, and that greatly helped to relieve the natural insecurity that newcomers can feel. I treasure the memories on various conversations in the coffee corner, as well as those of several field days, on land and on the water. I also felt a great honour in supervising the flight practical of the university, of which I am proud to have been a part. Thanks to everyone who helped making me a part of the team.

Within the university, I have been in close contact with many contemporary PhD students. Some of them started after me, some of them graduated before me, and some of them did both. I remember the events that we had together, some scheduled and some improvised. There were group lunches, tea breaks, barbecues, pub quizzes, game nights and frantic table tennis matches. I specifically remember (in order of success) a royal cheese fondue, an imaginary spicy chicken sandwich and a glamorous Italian coffee. The PhD community at the section is the living proof that working on a PhD is more than 'working on a PhD'.

A special word of thanks is due to the people with whom I have shared office space during the time of my PhD. I have had the luck of encountering the most friendly roommates that I could have expected, and I greatly enjoyed my time with all of you. The conversations about all kinds of things, whether professional, casual or emotional, were both good for relaxing and insightful and I have learned much from your company.

I've experienced the most beautiful moments during this PhD, and I've also felt insecure at times, for various reasons. But when I felt down, there was always someone around who showed that they cared, and that helped me a lot. Some people gave advice, some people expressed empathy, and others just listened. Whatever you did: you helped to shape me into the person who I am and you enriched my life. Even though I cannot possibly name every such situation in this section, please know that I am deeply grateful for all the support that I received from everyone.

This dissertation is a product of interactions. It would not be possible without your advice, kindness, love, enthusiasm, insight, friendship, appetite, openness, altruism, guidance, empathy, and support.

Thank you.

Jerom

Curriculum Vitæ

Jerom Bastiaan MAAS

22-11-1990 Born in 's-Hertogenbosch, the Netherlands

Education

2002–2008 Het Stedelijk Gymnasium van 's-Hertogenbosch
's-Hertogenbosch, the Netherlands
Profile: Nature and Technology

2008–2011 BSc in Aerospace Engineering
Delft University of Technology, the Netherlands
Minor: Communication in Technology and Business

2012–2015 MSc in Aerospace Engineering,
Delft University of Technology, the Netherlands
Control and Operations (Traffic Management and Airports)
Honours Track titled: 'Youth influence in innovation policy'
Thesis on large-scale simulations of uncontrolled airspace

2015–2021 PhD: Aerospace Engineering, Control and Operations
Delft University of Technology, the Netherlands
Thesis: Radar Sensing in General Aviation
Promotor: Prof. dr. ir. J. M. Hoekstra

Professional Experience

2011-2012	Open Jongerenvereniging De Koornbeurs Delft, the Netherlands Secretary of the daily board of a society of 350 members
2012-2013	Adviesraad voor Wetenschaps- en Techniekbeleid Den Haag, the Netherlands Study towards youth influence in innovation policy
2014	Nationaal Lucht- en Ruimtevaartlaboratorium Amsterdam, the Netherlands Researching the use of commercial navigation apps by pilots
2020-Present	Radar Based Avionics Delft, the Netherlands Developing Radar Technology for Hazard Detection in Aviation

List of Publications

Journal Articles

5. **J. Maas**, R. Van Gent and J. Hoekstra, *Feasibility of Obstacle Detection using a Passive Radar*, Submitted to IEEE Transactions on Aerospace and Electronic Systems, 2021

4. **J. Maas**, R. Van Gent and J. Hoekstra, *Modelling an Airborne Detect & Avoid Radar for General Aviation*, Submitted to Journal of Aerospace Information Systems, 2021

3. **J. Maas**, R. Van Gent and J. Hoekstra, *Estimation of Flight State with a Collision Alert Radar*, Journal of Aerospace Information Systems: Vol. 18, No 6, Pg. 347-354, 2021

2. **J. Maas**, R. Van Gent and J. Hoekstra, *A Portable Primary Radar for General Aviation*, PLoS ONE 15(10), 2020

1. E. Sunil, J. Ellerbroek, J. Hoekstra and **J. Maas**, *Three Dimensional Conflict Count Models for Unstructured and Layered Airspace Designs*, Elsevier Transportation Research Part C: Emerging Technologies, Vol. 95, Pg. 295-319, 2018

Conference Proceedings

8. **J. Maas**, R. Van Gent and J. Hoekstra, *Estimation of Flight State with a Collision Alert Radar*, ICRAT International Conference for Research in Air Transportation, 2020

7. **J. Maas**, V. Stefanovici, R. Van Gent and J. Hoekstra, *Validation of GPS by Ground Scanning Radar*, ICRAT International Conference for Research in Air Transportation, 2020

6. **J. Maas**, R. Van Gent and J. Hoekstra, *Object Tracking in Images of an Airborne Wide Angle FMCW Radar*, ICRAT International Conference for Research in Air Transportation, 2018

5. J. Hoekstra, J. Ellerbroek, E. Sunil and **J. Maas**, *Geovectoring: Reducing Traffic Complexity to Increase the Capacity of UAV airspace*, ICRAT International Conference for Research in Air Transportation, 2018

4. E. Sunil, J. Ellerbroek, J. Hoekstra and **J. Maas**, *Modeling Airspace Stability and Capacity for Decentralized Separation*, USA Europe Air Traffic Management Research and Development Seminar, 2017

3. **J. Maas**, E. Sunil, J. Ellerbroek and J. Hoekstra, *The Effect of Swarming on a Voltage Potential-Based Conflict Resolution Algorithm*, ICRAT International Conference for Research in Air Transportation, 2016

2. J. Hoekstra, **J. Maas**, M. Tra and E. Sunil, *How Do Layered Airspace Design Parameters Affect Airspace Capacity and Safety?*, ICRAT International Conference for Research in Air Transportation, 2016

1. E. Sunil, **J. Maas**, J. Ellerbroek and J. Hoekstra,*The Relationship Between Traffic Stability and Capacity for Decentralized Airspace*, ICRAT International Conference for Research in Air Transportation, 2016